Observations and modeling of the active galactic nucleus B2 1215+30 together with performance studies of the ground-based gamma-ray observatories VERITAS and CTA

D i s s e r t a t i o n

zur Erlangung des akademischen Grades

d o c t o r r e r u m n a t u r a l i u m

(Dr. rer. nat.)

im Fach Physik

eingereicht an der
Mathematisch-Naturwissenschaftlichen Fakultät I
der Humboldt-Universität zu Berlin

von
Dipl. Phys. Heike Prokoph

Präsidentin/Präsident der Humboldt-Universität zu Berlin:
Prof. Dr. Jan-Hendrik Olbertz

Dekanin/Dekan der Mathematisch-Naturwissenschaftlichen Fakultät I:
Prof. Stefan Hecht PhD

Gutachter/innen: 1. Dr. Gernot Maier
2. Prof. Dr. Thomas Lohse
3. Prof. Dr. Reshmi Mukherjee

Tag der mündlichen Prüfung: 16. August 2013

"Alles Wissen und alles Vermehren unseres Wissens
endet nicht mit einem Schlußpunkt,
sondern mit einem Fragezeichen."

Hermann Hesse

Abstract

Ground-based gamma-ray astronomy, which provides access to photons in the TeV energy range, has been a rapidly developing discipline over the past decades. In this thesis, the performance of the current- and next-generation imaging atmospheric Cherenkov telescopes VERITAS and CTA is evaluated using Monte Carlo simulations. Special emphasis is given to the possible extension of the duty cycle of CTA. It is shown that an increase of about 30% in observation time can be achieved through operation under partial moonlight without significant losses in performance. The increased observation time is especially important when studying astronomical objects which are variable at very high energies (VHE; $E > 50$ GeV), such as active galactic nuclei (AGN), as this allows the extension of monitoring or multi-wavelength campaigns on these occasionally flaring sources.

AGN represent to date about one third of the population of known VHE gamma-ray sources. Most of them are blazars, whose emission is dominated by non-thermal radiation of relativistic jets closely aligned to the line of sight of the observer. The blazar B2 1215+30 has been observed by VERITAS for nearly 100 hours between 2008 and 2012. The data analysis presented in this thesis yields a detection significance of 9.0σ and shows long-term variability with a relatively bright flux state in 2011. Multi-wavelength data are used to construct the spectral energy distribution of B2 1215+30 which is well described by a one-zone leptonic model. The model is presented in detail and possible constraints are investigated. The results of the modeling are discussed and put in context with other VHE-detected blazars.

Kurzfassung

Das Gebiet der bodengebundenen Gamma-Astronomie bietet Zugang zu Photonen im TeV-Energiebereich und hat sich in den letzten Jahrzehnten vor allem durch den Erfolg der abbildenden atmosphärischen Cherenkov-Technik profiliert. In dieser Arbeit werden zwei dieser Cherenkov-Teleskop-Systeme, VERITAS und das zukünftige CTA, mit Hilfe von Monte-Carlo-Simulationen in Hinblick auf deren Sensitivität auf hochenergetische Gammastrahlung ($E > 50$ GeV) untersucht. Besonderes Augenmerk wird hierbei auf die Beobachtungsmöglichkeit mit CTA unter Mondlicht gelegt. Es wird gezeigt, dass dadurch eine Beobachtungszeitverlängerung um etwa 30% ohne signifikante Sensitivitätsverluste erreicht werden kann. Die erhöhte Beobachtungszeit ist besonders für zeitlich variable Quellen wichtig, da dies die Ausweitung von Überwachungs- oder Multi-Wellenlängen-Kampagnen ermöglicht.

Eine dieser stark variablen Quellklassen sind aktive Galaxienkerne, welche zur Zeit etwa ein Drittel der bekannten hochenergetischen Gammastrahlungsquellen repräsentieren. Die meisten davon sind Blazare, deren Emission durch nicht-thermische Strahlung aus gebündelten Strömen von Materie und Energie (sogenannten Jets) dominiert wird. Diese Jets breiten sich mit annähernd Lichtgeschwindigkeit aus und sind in Sichtlinie des Betrachters ausgerichtet. Der Blazar B2 1215+30 wurde zwischen 2008 und 2012 mit VERITAS fast 100 Stunden beobachtet. Die Datenanalyse, welche in dieser Arbeit präsentiert wird, weist die Quelle mit einer Signifikanz von 9.0σ nach und offenbart Langzeitvariabilität mit einem hellen Flusszustand im Jahr 2011. Multi-Wellenlängen-Daten werden verwendet um die spektrale Energieverteilung von B2 1215+30 zu konstruieren, welche gut mit einem leptonischen Ein-Zonen-Modell beschrieben werden kann. Das verwendete Modell wird im Detail vorgestellt und mögliche Einschränkungen an den Modellparameterraum untersucht. Die Ergebnisse der Modellierung von B2 1215+30 werden diskutiert und in Zusammenhang mit anderen bekannten hochenergetischen Gammastrahlen-Blazaren gesetzt.

Contents

1. Introduction

Gamma-ray astronomy studies astronomical objects using the most energetic form of electromagnetic radiation. Gamma-ray photons are at least one hundred thousand times more energetic than an optical photon. These high-energy gamma rays cannot penetrate the Earth's atmosphere which makes it impossible to observe the radiation emitted from the astronomical object directly from ground. To detect those photons directly, one has to place the detector above the atmosphere. This method has been successfully applied to measure photons from X-ray up to MeV/GeV energies. However, with increasing photon energy, space-borne instruments become more and more ineffective due to the steeply decreasing fluxes of the astronomical objects and hence the limited number of photons which can be collected with the about 1 m^2 detector area.

To detect very-high-energy (VHE; E>50 GeV) gamma rays much larger detector areas are needed, so far only achievable from ground. Although these gamma rays cannot be detected directly from ground, they interact with the atmosphere and initiate so-called air showers. These air showers consist of highly relativistic particles which emit Cherenkov radiation and two main methods exist to detect their interacting products. One is based on the detection of the shower particles itself, while the other detects the Cherenkov light emitted within the air shower. The particle detector arrays have the advantage of a large duty cycle ($\sim$ 100%) and a large field of view ($\sim$ 1 sr) but their performance is restricted by an inefficient rejection of the (much more abundant) cosmic-ray background, as well as by the reconstruction of the energy and direction of the incoming gamma ray. Therefore, even though current (or past) particle detector arrays like MILAGRO[1], Tibet ASγ[2], and ARGO-YBJ[3] have done some interesting gamma-ray observations, this technique will probably not be competitive with the Cherenkov experiments until the arrival of the next generation of instruments like HAWC[4] or LHAASO[5] (Panaque, 2012). The Cherenkov experiments on the other hand can further been divided into non-imaging (e.g.,

[1] http://www.lanl.gov/milagro
[2] http://www.icrr.u-tokyo.ac.jp/em/index.html
[3] http://argo.na.infn.it/
[4] http://www.hawc-observatory.org/
[5] http://english.ihep.cas.cn/ic/ip/LHAASO/

STACEE[6] or HiSCORE[7]) and imaging (e.g., H.E.S.S.[8], MAGIC[9], VERITAS[10], or FACT[11]). The latter experiments use arrays of imaging telescopes consisting of a reflecting surface which focusses the Cherenkov light onto a fast recording, pixelized camera. They have a typical field of view of 3-5° and a duty cycle of about 10% ($\sim$ 1000 hours/year), as the faint bluish Cherenkov light from air showers cannot be detected during daylight. This technique has proven to be the most powerful approach to detect gamma rays in the energy range from several tens of GeV to a few tens of TeV as it combines a good angular and energy resolution with a high background rejection efficiency. For a review of the detection techniques see, e.g., Hinton & Hofmann (2009) or Panaque (2012).

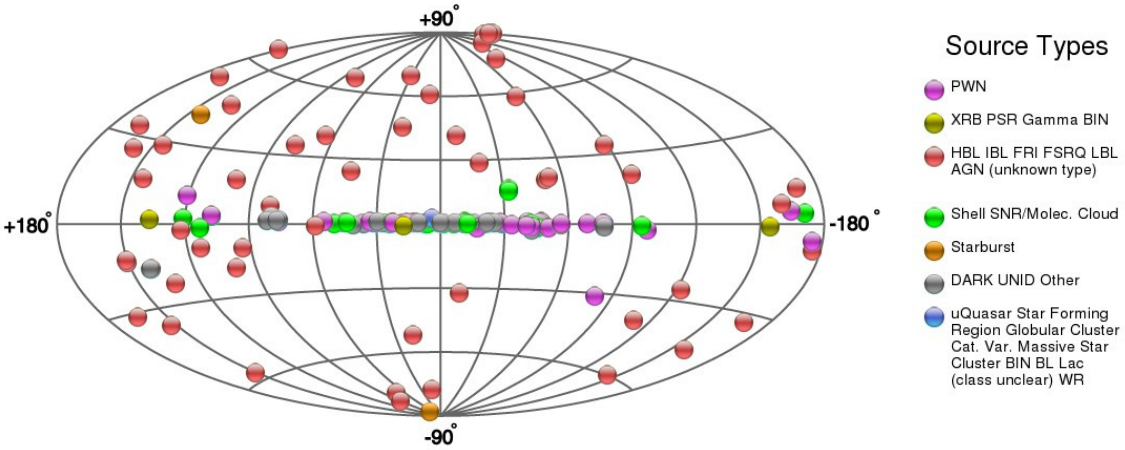

Figure 1.1.: Sky map in galactic coordinates of the TeV sources detected by IACTs. Each point represents a gamma-ray source and the colors represent different source classes as explained in the legend. Image credit: Wakely & Horan (2013).

The number of known VHE gamma-ray emitters detected by Imaging Atmospheric Cherenkov Telescopes (IACTs) currently exceeds 150 sources (Wakely & Horan, 2013) and includes morphological, spectroscopic and temporal studies. The objects are of galactic and extragalactic origin, as shown in Figure 1.1. Among the galactic objects, source types include supernova remnants (SNRs), pulsars and pulsar wind nebulae (PWNe), binary systems, interacting stellar winds as well as unidentified sources without any obvious counterparts in other wavelength regimes. Out-

[6] http://www.astro.ucla.edu/~stacee/
[7] http://www.iexp.uni-hamburg.de/groups/astroparticle/score/en/
[8] http://www.mpi-hd.mpg.de/hfm/HESS/
[9] http://magic.mppmu.mpg.de/
[10] http://veritas.sao.arizona.edu/
[11] http://www.isdc.unige.ch/fact/

side our Galaxy, starburst galaxies and various types of active galactic nuclei (AGN) have been detected to emit VHE gamma rays. Several additional source classes are thought to be possible VHE emitters, but have not yet been detected. These include, for example, gamma-ray bursts (GRBs), galaxy clusters and microquasars as well as possible signatures from dark matter. The reader is referred to Aharonian et al. (2008) or Rieger et al. (2013) for a general overview of the status of VHE gamma-ray astronomy.

Many of the observations over the last decade have shown the large discovery potential in the VHE regime and have raised new questions, especially about the origin of these high-energy photons. For this reason, scientists around the world have come together to build a new instrument – the Cherenkov Telescope Array (CTA[12]). The aim of CTA is to make significant progress over the existing experiments. CTA will be able to detect probably more than 1000 sources over the whole sky, including many AGN, and thus might answer many of the persisting questions about the underlying processes in those sources. CTA has as well a large discovery potential for "new physics" as the domain of VHE gamma rays is sensitive to energy scales important for particle physics (the 100 GeV scale expected for cold dark matter, the TeV scale where super-symmetry may emerge, and even perhaps the unification scale for the strong and electroweak forces). For more details about the scientific motivation of future IACT arrays, the reader is referred to Buckley et al. (2008) and Actis et al. (2011).

In this thesis, VHE observations of the blazar-type AGN B2 1215+30 with VERITAS are used to derive a deeper understanding of the physical processes in this source by modeling its broadband emission. The reconstruction of the properties of astronomical objects at very high energies requires a precise knowledge of the detector and its performance. Therefore, the performance for the current- and next-generation ground-based gamma-ray observatories VERITAS and CTA is evaluated.

The thesis is structured as follows. Chapter 2 details the detection principle of VHE gamma rays by imaging atmospheric Cherenkov telescopes. It is followed by a description of the VERITAS experiment and the analysis chain used throughout this thesis in Chapter 3. In the same chapter, a first performance estimate for the VERITAS upgrade with new cameras in 2012 is presented. A further step towards an increased sensitivity to VHE gamma-ray sources is expected from the future CTA observatory, described in Chapter 4. Monte Carlo (MC) simulations are used to determine the performance characteristics of CTA and to explore the feasibility of operations under partial moonlight to increase the duty cycle of the instrument. Chapter 5 gives on overview of the observations of blazars and presents in detail the long-term observations of B2 1215+30 with VERITAS and additional multi-wavelength instruments. To understand the

[12] `https://www.cta-observatory.org/`

underlying processes in AGN, the observed spectral energy distribution (SED) is modeled. The model and possible constraints on its input parameters are demonstrated in Chapter 6 before it is applied to the SED of B2 1215+30. The obtained results are discussed and compared to other VERITAS-detected blazars. Chapter 7 summarizes the results of this thesis.

2. Imaging Atmospheric Cherenkov Technique

In this chapter, the detection principle of VHE gamma rays by Imaging Atmospheric Cherenkov Telescopes (IACTs) is presented. It starts with an introduction of the basic properties of air showers and their emission of Cherenkov light (Section 2.1). Then, the detection principle itself is outlined (Section 2.2) and current IACT facilities are briefly presented.

2.1. Air showers

An air shower is a cascade of particles generated by the interaction of a high-energy cosmic-ray particle with the molecules of the atmosphere (Gaisser, 1990). The number of particles in the cascade at first multiplies while the energy of the primary particle is distributed among the secondary particles. The cascade then reaches a maximum and attenuates as more and more particles fall below the energy threshold for further particle production and the shower dies out. Depending on the type of the primary particle, the development of the shower differs. In case of a primary photon or electron/positron, most of the interactions are of electromagnetic type and the initiated shower is called *electromagnetic shower*. In case of a primary hadron, the shower develops in a complex way as a combination of electromagnetic sub-showers and hadronic multi-particle production while interactions via the strong and the weak force occur. This kind of shower is called *hadronic shower*. As hadrons are much more numerous than gamma rays, they contribute most to the background measured by IACTs.

2.1.1. Electromagnetic air showers

An electromagnetic air shower initiated by a high-energy photon starts with the production of an electron-positron pair within the Coulomb field of an atmospheric nucleus[1]. The energy E_0 of the primary photon is, on average, shared in equal parts by the electron and the positron. The high-energy electrons and positrons undergo bremsstrahlung in the presence of an electromagnetic field of an atomic nucleus and radiate gamma rays. This process, together with the pair production, repeats itself and the particle cascade starts to develop. As a result, the number of

[1] Muon−anti-muon production is negligible as the cross section in air is only $\sim 12\mu$b, compared to $\simeq 500$ mb for electron-pair production.

particles in the shower increases exponentially with atmospheric depth. As the shower evolves, the energy of each individual particle reaches the critical energy E_c, where energy losses through ionization become the dominant process for electrons ($E_c \approx 83$ MeV in air). At this point, the maximum number of particles is reached and the particles are gradually absorbed by ionization. Further on, the mean photon energy reduces and the cross section for pair production decreases until it becomes of the same order of Compton scattering and photoelectric absorption (few MeV). Eventually, the particle cascade dies out.

The variation of the number of particles with atmospheric depth (or in dependence of the radiation length[2]) is often called *longitudinal shower development*. It is shown in Figure 2.1 and demonstrates some of the basic properties of the electromagnetic air shower development (e.g., Heitler, 1954; Rossi & Greisen, 1941): (i) the number of particles increases exponentially in the initial phase of the cascade development, (ii) the maximum number of particles is proportional to the energy of the primary particle ($N_{\max} \propto E_0$), and (iii) the depth of the shower maximum grows logarithmically with the primary energy ($X_{max} \propto \ln E_0$). For low energetic primaries, the electromagnetic cascade develops early in the atmosphere (i.e. at high altitudes) and the cascade dies out relatively soon. Additionally, much fewer particles are created within the cascade compared to showers initiated by high-energy gamma rays.

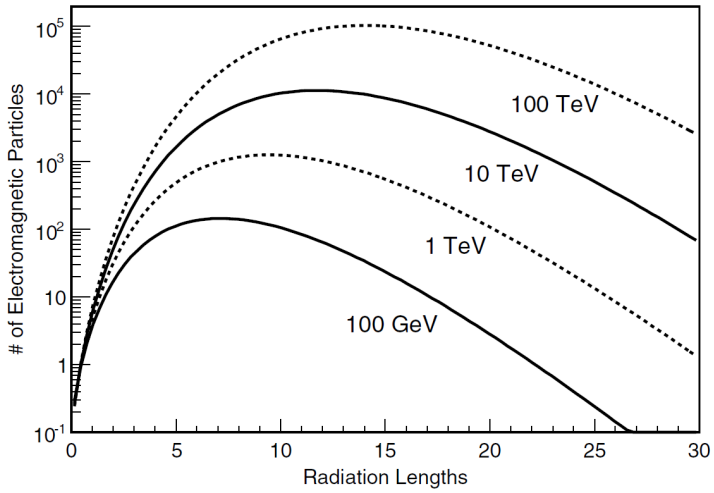

Figure 2.1.: Longitudinal shower development of electromagnetic air showers for different primary energies. Sea level corresponds to about 27 radiation lengths. Figure taken from Aharonian et al. (2008).

[2] The radiation length for photons and electrons in air is $X_0 \simeq 37\text{g/cm}^2$. The atmosphere therefore corresponds to a depth of 27 radiation lengths.

The lateral spread of an electromagnetic shower is due to the deflection of charged particles within the Earth's magnetic field and multiple Coulomb scatterings of low-energy electrons within the air shower. The Coulomb scattering scales with the Molière radius R_{mol} which depends on the radiation length X_0 and the critical energy in a given material: $R_{mol} = 21.2\,\mathrm{MeV} \cdot X_0/E_c$. In the atmosphere the distance corresponding to X_0 varies with the density. It is $R_{mol} = \frac{9.6\,\mathrm{g\,cm^{-2}}}{\rho}$, which is approximately 80 m at sea level (Heck et al., 1998). On average, 90% of the shower energy is deposited inside a cylinder around the shower axis with radius R_{mol}.

2.1.2. Hadronic air showers

When a high-energy cosmic-ray particle like a proton (or a heavier nucleus) enters the Earth's atmosphere it interacts with the nuclei of air molecules and initiates a hadronic air shower. This air shower consists of three components: a hadronic core, a mounic component and electromagnetic sub-showers. This is illustrated schematically in Figure 2.2.

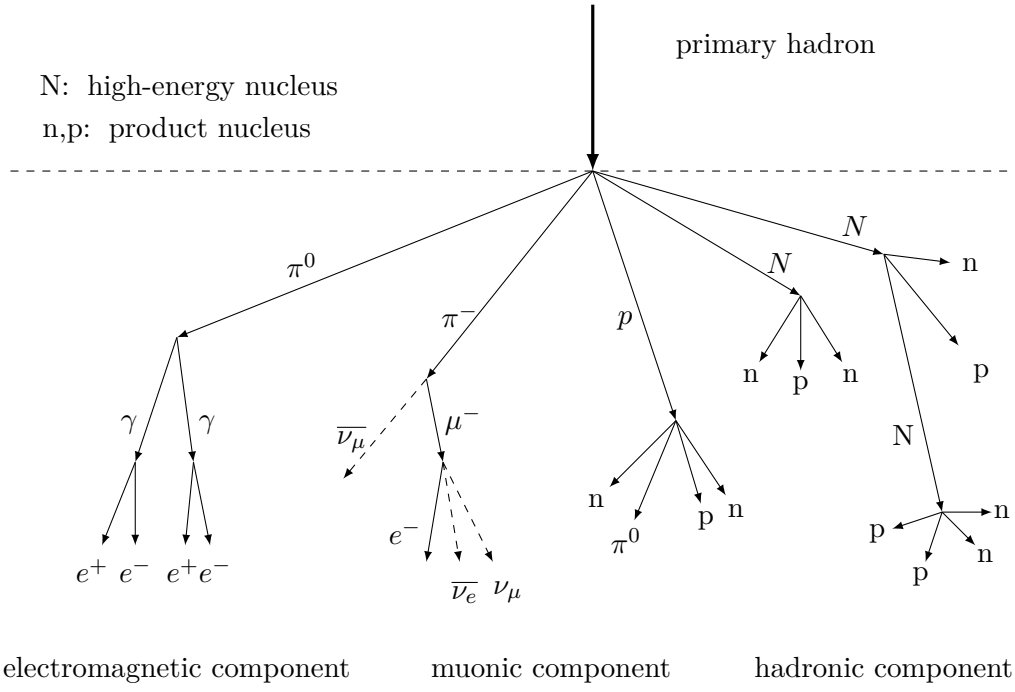

Figure 2.2.: Schematic model of an hadronic air shower generated by a cosmic ray. Note that the length of the arrows does not correspond to the distance traveled in the particle's lifetime.

Within the shower mesons like pions, kaons as well as light baryons are produced. Most neutral pions decay almost immediately into two gamma rays ($\pi^0 \to \gamma\gamma$, mean lifetime $\tau = 0.84{\times}10^{-16}$s).

These photons initiate electromagnetic sub-showers through electron-positron pair production. This makes the energy transfer from the hadronic to the electromagnetic component of an air shower very efficient. In fact, about one third of the hadronic energy is transferred to the electromagnetic component at every hadronic interaction length (Gaisser, 1990).

The charged pions and kaons produce a new generation of mesons through interactions with the atmosphere. The multiplication will continue until the energy drops below the critical energy, where the decay of $\pi^{\pm}$ and $K^{\pm}$ into muons becomes more likely then their interaction. Thus, pions and kaons of lower energy decay and feed the muonic component of the shower. Nucleons and other high-energy hadrons contribute further to the hadronic component. Since most hadrons re-interact, most of the primary energy is transfered to the electromagnetic component.

Compared to electromagnetic air showers there are some significant differences in the development of hadronic cascades, illustrated on the example of a 100 GeV gamma-ray (left) and a 100 GeV proton shower (right) in Figure 2.3. The general differences can be summarized as follows:

- The secondary particles of hadronic showers receive a high transverse momentum, e.g. by inelastic scattering and decay processes. This leads to a much larger lateral extension compared to electromagnetic showers where the lateral spread is determined by elastic multiple Coulomb scattering for which the mean scattering angle for high-energy photons is very small.

- Hadronic air showers are less regular and have larger fluctuations due to the complex multiparticle processes in their development, compared to the rather compact developments of electromagnetic air showers.

- The nuclear interaction length λ_N of hadrons in air is $\lambda_{\text{proton}} \approx 83\,\text{g/cm}^2$ and $\lambda_{\text{pion}} \approx 107\,\text{g/cm}^2$. This is larger than the radiation length for Bremsstrahlung $\lambda_{Brems} \approx 35\,\text{g/cm}^2$ or the mean free path for pair production $\lambda_{pair} \approx 35\,\text{g/cm}^2$. Therefore, hadrons penetrate deeper into the atmosphere than gamma rays or cosmic-ray electrons/positrons.

These differences in the air shower development are used later to discriminate between gamma-ray and hadronic (background) showers.

2.1.3. Cherenkov emission of air showers

Most of the charged particles in an air shower emit Cherenkov radiation (Čerenkov, 1937) when they travel through the atmosphere. This light is emitted in a narrow cone around the direction of the particle (see left side of Figure 2.4). The angle θ between the particle track and the

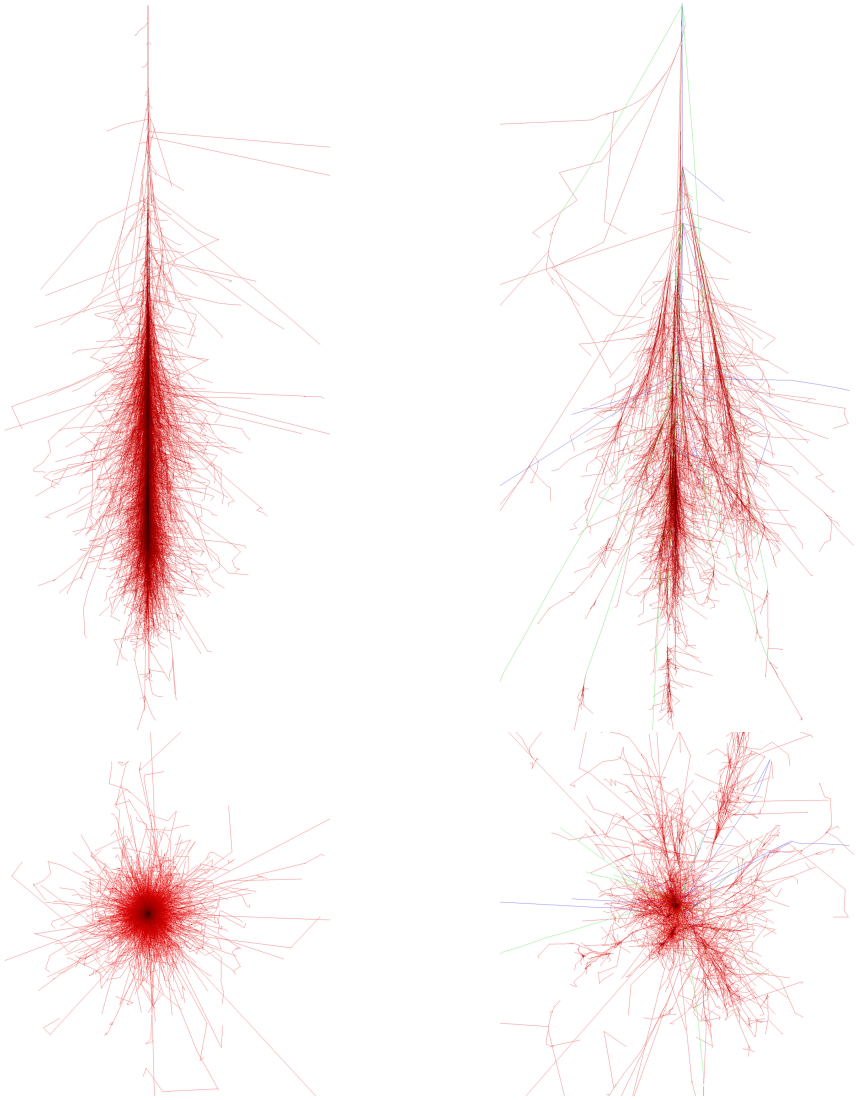

Figure 2.3.: Air shower simulations initiated by a 100 GeV photon (left) and proton (right). The upper plot shows the longitudinal development (dimension in y-direction 30 km) and the lower part shows the lateral extension (±5 km). Shown are the particle tracks, where *red* are electrons, positrons and gamma rays, *green* are muons and *blue* are hadrons. The first interaction height is fixed to 30 km height. Images taken from Schmidt (2005).

emission direction depends on the velocity $v = \beta c$ of the particle and the velocity of light $c' = c/n$ in the medium (with the refractive index n and the speed of light in vacuum c):

$$\cos\theta = \frac{c'}{v} = \frac{1}{\beta n}. \tag{2.1}$$

It implies that light emission can only take place if $\beta \geq 1/n$. This leads to a minimum energy of the particle needed to emit Cherenkov light:

$$E_{min} = \frac{mc^2}{\sqrt{1-\beta^2}} = \frac{mc^2}{\sqrt{1-n^{-2}}}. \tag{2.2}$$

The mass dependence of E_{min} indicates that light particles like electrons dominate the Cherenkov light emission in air showers. Above the energy threshold, the number of Cherenkov photons emitted within a certain wavelength interval $[\lambda_1, \lambda_2]$ can be described by the Frank-Tamm formula (Tamm & Frank, 1937):

$$\frac{dN}{dx} = 2\pi\alpha Z^2 \int_{\lambda_1}^{\lambda_2} \left(1 - \frac{1}{n(\lambda)^2\beta^2}\right) \lambda^{-2}\, d\lambda \tag{2.3}$$

where β and Z are the velocity and the charge of the charged particle, λ the wavelength and $\alpha \simeq 1/137$ the fine structure constant. The amount of light emitted by particles thus depends on the index of refraction in air.

As the density of air, and hence the refractive index, is not constant within the atmosphere, the energy threshold and the Cherenkov angle depend on the atmospheric altitude h. Under the assumption of an isothermal atmosphere one can use the barometric formula (Beringer et al., 2012) and obtains

$$n = n(h) = 1 + \eta_0 \cdot e^{-h/h_0} \tag{2.4}$$

with $\eta_0 = 2.9 \cdot 10^{-4}$ and $h_0 = 7.1\,\mathrm{km}$. Inserting this in Eq. 2.1, gives the dependence of the Cherenkov angle on the height of emission. At high altitudes (where the refractive index is close to unity) the emission angle is small and then grows with increasing density to about $\theta \approx 1.4°$ at sea level. As a result, the light emitted from particles at the different altitudes superimposes at observation level, as illustrated schematically in Figure 2.4 (right).

Most of the Cherenkov light within an air shower is emitted around the shower maximum. Since the number of particles at the shower maximum is proportional to the primary energy of the particle, the energy of the primary gamma ray can be derived by measuring the number of Cherenkov photons on ground. This is illustrated in Figure 2.5 for vertical gamma-ray showers, showing an example of the arrival directions of the Cherenkov photons (left) and the average

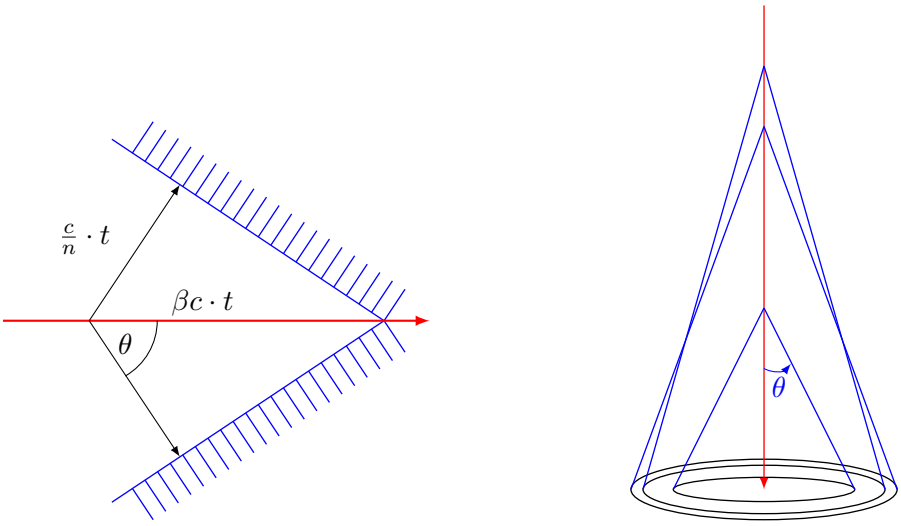

Figure 2.4.: (Left) Emission of Cherenkov radiation (blue) along the particle track of a charged, fast moving particle (red). (Right) The light emitted from each point of the particle track arrives as a ring on the ground. Due to the height-dependence of the Cherenkov angle, the superposition of the light emitted from the different particles at different altitudes leads to the characteristic Cherenkov light profile on ground.

lateral Cherenkov light distribution on ground (right). Up to distances of about 120 m from the shower track the Cherenkov photon density is fairly flat and is usually denoted as the "Cherenkov light pool" of the shower. Beyond the radius of the light pool, the number of photons decreases exponentially. It should be noted that the number density of Cherenkov photons is relatively small, i.e. for an energy of 100 GeV less than 10 photons/m^2 reach the ground (at $\sim$ 1270 m altitude). To detect these low-energetic showers, the detector size and thus the mirror area of the telescope has to be large in order to detect the few emitted photons.

The differences in the shower development between a hadron-induced and a gamma-ray-induced air shower are reflected in the shape and the time structure of the Cherenkov light distribution at ground. Air showers develop nearly with the speed of light, resulting in very short Cherenkov flashes. Typically, the front of Cherenkov photons produced in an electromagnetic air shower arrives at ground within an interval of 2-5 ns, whereas hadronic showers have a wider time spread (10-15 ns), mainly due to the development of many electromagnetic sub-showers and the larger transverse momentum of hadronic interactions. For the same reason, the lateral distribution of hadronic air showers is much more heterogeneous and asymmetric than from photon-induced cascades. Both the differences (in shape and time structure) can be used in IACTs to discriminate between hadronic cosmic-ray background and gamma-ray events.

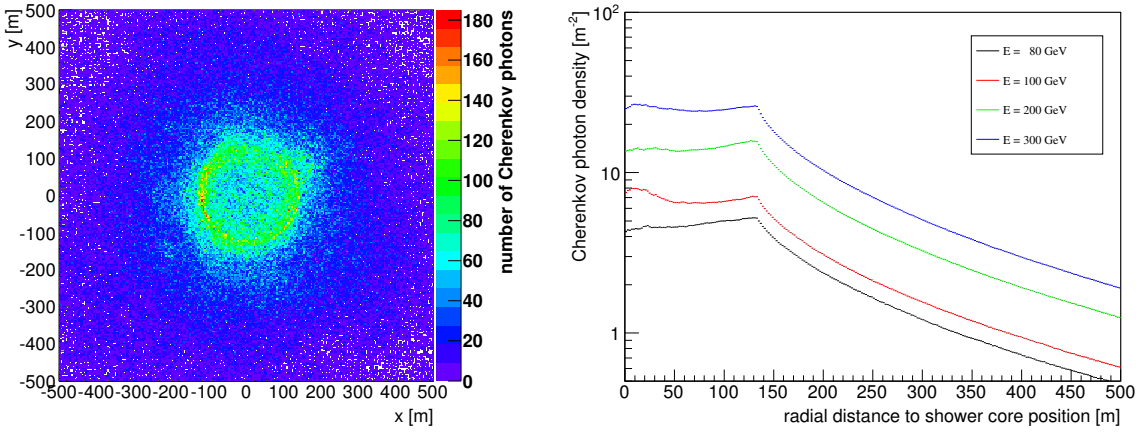

Figure 2.5.: Simulations of the Cherenkov photon density of vertical gamma-ray air showers at an altitude of 1270 m using VERITAS site specific parameters (i.e., magnetic field strength and the winter atmospheric profile). (Left) An example of the number of Cherenkov photons on ground level for a 80 GeV gamma-ray. (Right) Average lateral Cherenkov light distribution in the wavelength range from 200 to 750 nm for vertical gamma-ray showers of different energy (averaged over 100 showers).

2.1.4. Simulation of air showers

The propagation of particles through the atmosphere can be described by analytical and numerical models. While the analytical models predict, in general, the correct average values of the observables, the numerical treatment via Monte Carlo (MC) simulations is essential to correctly account for fluctuations between showers (Hansen et al., 2011).

Throughout this thesis, the air shower simulations are done with CORSIKA (COsmic Ray SImulations for KAscade; Heck et al., 1998). The CORSIKA program allows to simulate interactions and decays of nuclei, hadrons, muons, electrons, and photons up to primary particle energies of some 10^{20} eV. The development of air showers is simulated by tracing the single particles through the atmosphere. Environmental properties, such as the atmospheric density (mainly its vertical profile), its chemical composition as well as the geo-magnetic field, are taken into account. The main challenges in simulating the development of air showers initiated by cosmic rays are hadronic interactions, which play a central role. These interactions are still not well understood at very high energies and several reaction models are available within CORSIKA. In this thesis, hadronic interactions are described with UrQMD (at low energies) and QGSJET-II (at high energies). In addition, the shower development is strongly influenced by atmospheric conditions. As the atmosphere serves as target medium for the high-energy cosmic-

ray particles and as transport medium for the Cherenkov photons, a good knowledge about the local atmosphere is essential for the simulations.

Due to absorption and scattering processes in the atmosphere (Bernlöhr, 2000), not all the Cherenkov light emitted within an air shower reaches the ground. The most important processes are absorption bands of molecules, molecular (Rayleigh) scattering, and scatter on aerosols (Mie scattering). All of these processes are wavelength-dependent. While the Cherenkov photon spectrum shows, in general, a λ^{-2}-dependency of the number of photons (following Eq. 2.3), the observed photon spectrum on ground is different from the one emitted at a given altitude (see Figure 2.6). The most pronounced feature in the photon spectrum at ground is the peak at UV/blue wavelengths[3]. Therefore, photo-detectors which are most sensitive in this part of the spectrum are used in IACTs to efficiently detect the emitted photons. One should also note that these absorption effects depend on the local atmosphere and are usually subject to temporal variations which have to be taken into account in the simulation of air showers.

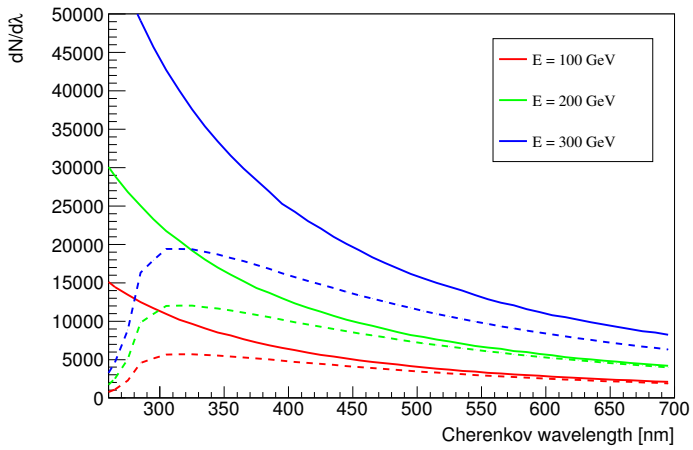

Figure 2.6.: Cherenkov photon spectrum emitted by a vertical gamma-ray shower of different primary energies. Solid lines correspond to all emitted Cherenkov photons within the air shower while dashed lines are after taking absorption processes in the atmosphere into account. Simulations are at 1270 m altitude, taking VERITAS site specific parameters into account.

[3] At wavelengths below $\sim$ 300 nm the Cherenkov photons are strongly absorbed due to atmospheric ozone.

2.2. Imaging Atmospheric Cherenkov Detectors

Imaging atmospheric Cherenkov detectors use the Earth's atmosphere as a calorimeter to sample the Cherenkov light from air showers (Galbraith & Jelley, 1953). As the Cherenkov radiation is very faint, detecting the showers, especially in the low energy regime (less than a few TeV), requires large reflectors to gather as much light as possible. It also requires fast responsive cameras as the light flashes are only a few nanoseconds in duration. A major challenge of this indirect detection method is to separate the high-energy gamma rays from the much more numerous cosmic rays, initiating as well particle cascades in the atmosphere. In the following, the detection principle is explained before a brief overview of IACT facilities is given.

2.2.1. Principle

The basic principle of imaging Cherenkov telescopes is illustrated in Figure 2.7. The light emitted in the air shower is reflected onto a camera located in the focal plane of the telescope. The camera itself consists of several hundreds of light-sensitive detectors, usually photomultiplier tubes (PMTs). Due to the typical dimensions of a gamma-ray air shower (longitudinal extension $\sim 10\,\mathrm{km}$, transversal extension ~ 50 m for an energy $E_\gamma \approx 1$ TeV) the obtained image in the camera has elliptical shape and is used to infer information about the primary particle. The light content of the image is the main estimator of the energy as the number of Cherenkov photons on ground is proportional to the energy of the primary gamma ray. The orientation of the image in the camera is used to determine the direction of the incoming particle.

In the stereoscopic approach, the air shower is detected by two or more telescopes simultaneously (Kohnle et al., 1996). The telescopes are separated by a distance comparable with the radius of the Cherenkov light pool. This allows different viewing angles on the shower. The combination of the images results in a better reconstruction of the shower properties. A system of two or more imaging Cherenkov telescopes has the additional advantage of an increased effective detection area and therefore an enhanced sensitivity (Fegan, 1997).

2.2.2. The background

The major challenge for IACTs is to distinguish between gamma-ray induced air showers and those initiated by other particles (background). Particles, which can mimic gamma-ray showers in the camera are cosmic hadrons (basically protons and helium nuclei), cosmic electrons and muons (Fegan, 1997; Maier & Knapp, 2007).

Hadrons are the most prominent background contribution as they are about one thousand times more numerous then gamma rays. In general, those air showers are longer, wider

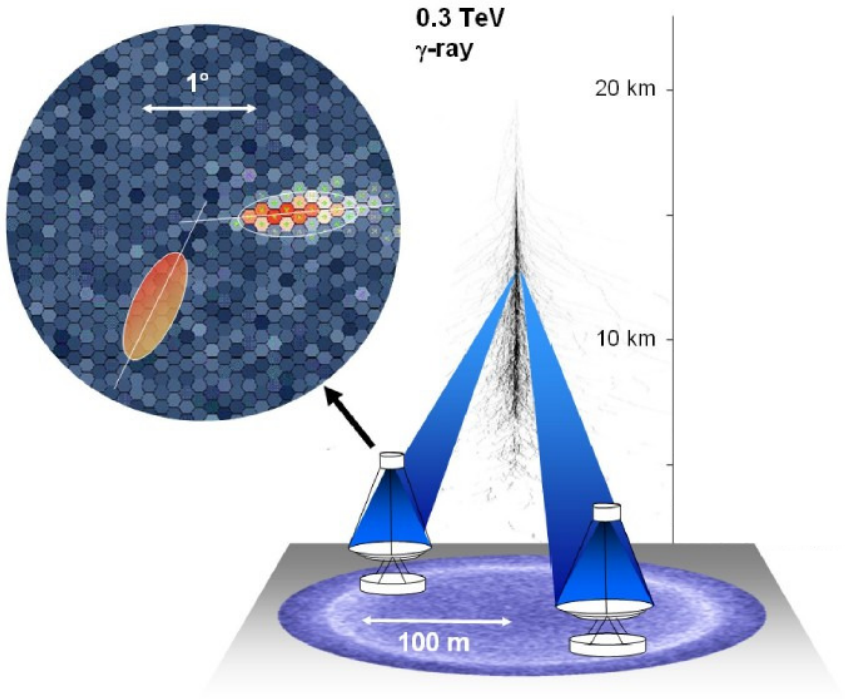

Figure 2.7.: Detection principle of an air shower using IACTs. By locating an IACT inside the Cherenkov light pool, the light from the shower is mapped onto the pixelated camera in the focal plane of the telescope. The detected light forms an image in the camera (figure inset upper left) which can be parameterized by an ellipse (see Section 3.2.2). When more than one telescope is used, the shower can be viewed stereoscopically and the images from the cameras can be overlaid in the camera coordinate system to reconstruct the shower direction (see Section 3.2.3). Picture adapted from Hinton & Hofmann (2009).

and more irregular then gamma-ray showers (as shown in Section 2.1). Therefore, they can be rejected based on the shape of the Cherenkov image (see Section 3.2.4). However, for low-energetic hadrons statistical fluctuations in the air shower development do effect much more the recorded image and the suppression power based on the shape of the image is reduced. An additional rejection of hadrons is based on their arrival direction. As hadrons are charged particles, they are deflected within the interstellar magnetic fields and thus arrive isotropically on Earth. They can therefore be discriminated easily from a gamma-ray point source (see Section 3.2.5).

Electrons are almost indistinguishable from gamma-ray primaries, as they also initiate an electromagnetic air showers. Their rejection is based on their arrival direction.

Muons which are considered as background for IACTs are high-energetic secondary particles produced within the air shower. Due to the small light pool of an energetic muon, multiple telescope images occur only if telescopes are very close to each other and they can be efficiently rejected based on the stereoscopic approach.

Another source of background is the light from the night sky. A number of different components contribute to this night sky background (NSB) light, e.g. air-glow (light emitted by atoms and molecules in the upper atmosphere - its intensity increases with increasing zenith angle), zodiacal light (sunlight which scattered by interplenary dust near the ecliptic - it is most prominent shortly after sunset or before sunrise), starlight, and man-made light (depending on the location of the Cherenkov telescope system). Additionally, the scattered light from the Moon or the moonlight itself can also contribute significantly to the NSB. As the typical yield of Cherenkov photons is roughly $100\,\text{photons}\,\text{m}^{-2}\,\text{TeV}^{-1}$, the light of the NSB, with intensities of the order of $10^{12}\,\text{photons}\,\text{m}^{-2}\,\text{sr}^{-1}$, represents a significant limitation for the performance of IACTs. It defines the minimum Cherenkov light yield which can be reliably detected with the telescope, and hence its energy threshold (Preuss et al., 2002). As the Cherenkov light from air showers is only a few nanoseconds long and the background light due to night sky is random in time and space the installation of fast electronics allows to suppress a huge amount of background light to be recorded by the camera.

2.2.3. IACT facilities

While the success of early detectors has been limited by the overwhelming background of cosmic rays, the development of the imaging technique by Whipple (e.g., Weekes et al., 1989; Kildea et al., 2007) has addressed this problem by exploiting the differences in the air shower development seen in the Cherenkov light distribution. Further improvement has been achieved by HEGRA (Daum et al., 1997) with the introduction of stereoscopic observations. Additionally, the deployment of fast read-out electronics combined with finer pixels by CAT (Barrau et al., 1998) improved the resolution of the recorded image and marks another important step towards the current generation of imaging Cherenkov telescope arrays. Pictures of those three facilities are shown in Figure 2.8 and the interested reader is referred to Watson (2011) and Hillas (2013) for a historical review of the detection methods.

Further developments of the detectors and in the discrimination of background lead to the foundation of ground-based gamma-ray astronomy using IACTs. The three major IACT observatories of the current generation are: H.E.S.S. in Namibia (Aharonian et al., 2006), MAGIC on the Canary Islands (Aleksić et al., 2012a), and VERITAS in southern Arizona (see next chapter). They are shown in Figure 2.9 and their key characteristics are given in Table 2.1. They

Figure 2.8.: Pictures of the different telescopes which mark the most important steps towards the current generation of IACTs. (Left) Whipple 10 m telescope. Image credit: VERITAS collaboration (Upper right) CAT. Image credit: CAT collaboration (Lower right) One of the HEGRA telescopes. Image credit: HEGRA collaboration

Instrument	Lat (°)	Long (°)	Alt (m)	Telescopes	Mirror Area (m^2)	Pixels	FoV (°)
Whipple	32	-111	2300	1	75	379	3.2
HEGRA	29	18	2200	5	8.5	271	4.3
CAT	42	2	1650	1	17.8	600	4.8
H.E.S.S.	-23	16	1800	4	107	960	5
H.E.S.S. II	-23	16	1800	1	614	2048	3.2
MAGIC	29	18	2225	2	234	1039	3.5
VERITAS	32	-111	1275	4	106	499	3.5

Table 2.1.: Basic characteristics and properties of three historical and the major three currently operational IACTs. H.E.S.S. II denotes the fifth telescope in the middle of the H.E.S.S. array. Table adapted from Acharya et al. (2013).

all employ stereoscopic observations combined with large mirror areas. They consist of $2-5$ Cherenkov telescopes, separated by distances of the same order as the Cherenkov light pool. This provides a large effective area of about $10^5\,\mathrm{m}^2$ and the recording of simultaneous images of the air shower can be used to pinpoint the location of the source with high accuracy. All three experiments also use fast electronics and their cameras consist of several hundred PMTs. The size of the PMTs is matched to the size of the air shower in the atmosphere to allow for efficient background suppression due to the image shape. The improvements in background rejection compared to the predecessor instruments, boosted the sensitivity to very high-energy gamma-ray sources over a wide range of energies. The current instruments reach sensitivities of about 1% of the Crab Nebula flux[4] for observing times of about 25 hours (Acharya et al., 2013).

Figure 2.9.: Pictures of the different IACTs of the current generation. (Left) One of the four VERITAS telescopes, for a picture of the full array see Figure 3.1. (Upper right) H.E.S.S. array consisting of five Cherenkov telescopes. Image credit: H.E.S.S. collaboration (Lower right) The two MAGIC telescopes. Image credit: MAGIC collaboration

[4] The Crab Nebula is the brightest steady source in VHE gamma rays which is usually used as a reference flux in VHE astronomy. Its flux at 1 TeV is $\approx 2 \times 10^{-11}\mathrm{cm}^{-2}\mathrm{s}^{-1}$ (Hillas et al., 1998).

3. The Very Energetic Radiation Imaging Telescope Array System (VERITAS)

The Very Energetic Radiation Imaging Telescope Array System (VERITAS) is a ground-based gamma-ray observatory consisting of four imaging Cherenkov telescopes; probing the high-energy Universe with photon energies of $\sim$ 85 GeV to about 30 TeV. Details about the VERITAS array characteristics and its observations of the gamma-ray sky are given in Section 3.1. The reconstruction of the data is described in Section 3.2 in which also the Monte Carlo (MC) simulation chain is introduced. These MC simulations are not only used for the analysis, but also to estimate the performance of the instrument. One of these performance estimates has been carried out by the author and is presented in Section 3.3. It is dedicated to the study of improvements at lowest energies, expected from the VERITAS upgrade in summer 2012.

3.1. The VERITAS array

VERITAS is operating at the Fred Lawrence Whipple Observatory in southern Arizona, USA (+31° 40' 30.21", -110° 57' 7.77"), at an altitude of about 1270 m above sea level (Holder et al., 2011). VERITAS started as a single telescope in early 2005 and was completed as an array of four IACTs in 2007. The sensitivity of VERITAS has steadily increased since the array was commissioned in summer 2007 through improvements in the analysis as well as implementations of new hardware. The first major improvement happened in summer 2009 with the relocation of one of the four telescopes. This made the overall array layout more symmetric, as shown in Figure 3.1, and resulted in an increase of sensitivity of about 30%. This reduced the observation time needed to detect a 1% Crab Nebula-like source with 5 standard deviations (5σ) from 48 hours to less than 30 hours (Perkins et al., 2009). The second major upgrade happened in summer 2012 when the PMTs in all four cameras were replaced by high-quantum-efficiency devices. As all data presented in this thesis was taken before summer 2012, the description of the VERITAS instrument in the following concentrates on the 4-telescope array before the camera upgrade and covers hardware, calibrations, and observations.

Figure 3.1.: Pictures of the VERITAS array before (top) and after summer 2009 (bottom). The relocation of one of the telescopes in summer 2009 lead to relatively uniform distances (of roughly 100 m) between the four telescopes. Image credit: VERITAS collaboration.

3.1.1. The telescopes

The primary components of each of the four VERITAS telescopes are a reflector of 12 m diameter, a camera, a trigger system, and a data acquisition system. They are described in the following.

Telescope mechanics and tracking

The basic mechanical structure of each VERITAS telescope consists of an altitude-over-azimuth positioner and a tubular steel optical support structure (OSS). The camera is mounted on a quadrupod and a mechanical bypass of the upper quadrupod arm transfers the camera load directly to counter-weight supports located at the rear of the OSS (Holder et al., 2006).

The maximum slew speed of the telescopes during normal operations is one degree per second. The positioner encoder measurements are logged to a database at a rate of 4 Hz. These values are used to monitor any pointing discrepancies of the telescopes. The mechanical pointing accuracy of a VERITAS telescope is typically better than $\pm 0.01^\circ$ (Holder et al., 2006).

Telescope optics

The optics of each VERITAS telescope follows the Davies-Cotton design (Davies & Cotton, 1957) and has a 12 m diameter reflector and a 12 m focal length. The total reflector area is about 110 m^2 and consists of 350 identical hexagonal spherical mirror facets. The mirror reflectivity is 85% over the Cherenkov light wavelength regime (between 280 nm and 450 nm) with reflectivities typically $\geq$ 90% at 320 nm (see Figure 3.2). In order to maintain the high mirror reflectivity, mirrors are continuously re-coated (Roache et al., 2007).

The individual mirror facets are manually aligned so that the entire reflector will act as a single dish with a relatively small point spread function (PSF). The PSF describes the response of an imaging system to a point source of light at infinity and the 80% containment radius of the optical PSF of VERITAS is less than $\sim 0.05^\circ$ at operational elevations (McCann et al., 2010).

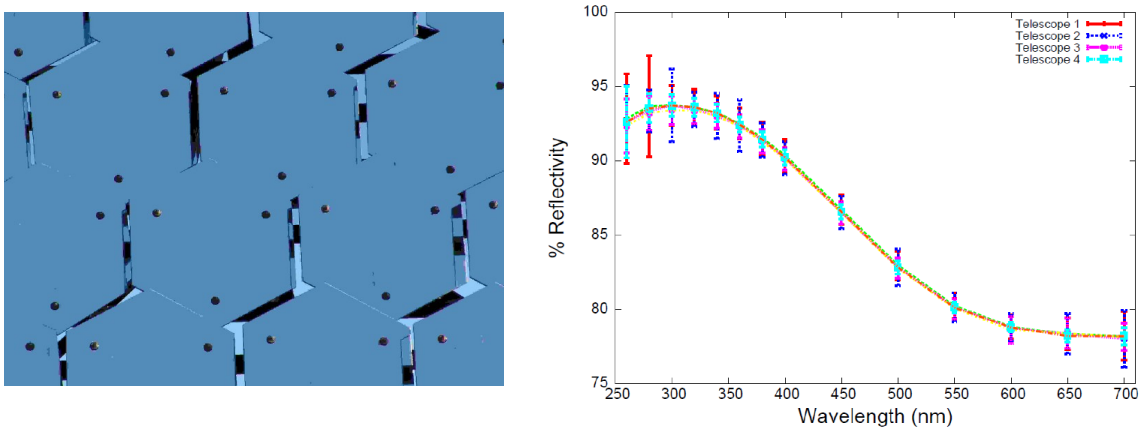

Figure 3.2.: (Left) A close-up view of the hexagonal VERITAS mirror facets. The three adjustment points which are used in aligning each facet can be easily seen. Image taken from Holder et al. (2006). (Right) Reflectivity measurements of the VERITAS telescope mirrors as a function of wavelength. The design specified reflectivities of 90% at 320 nm and >85% between 280 nm and 450 nm. Taken from Roache et al. (2007).

Camera and electronics

Each camera is located in the focus of the reflector and consists of 499 PMTs as shown in Figure 3.3. The PMTs (Photonis model XP2970/02) are UV-sensitive with a fast rise-time (1.9 ns) and a quantum efficiency of ∼20% at 320 nm. In front of each PMT is a light concentrator which reduces dead space between the PMTs and focusses the light on the center of the PMT photo-cathode. The angular pixel spacing is 0.15° and results in a total field-of-view (FoV) of 3.5°.

Figure 3.3.: (Left) Picture of the VERITAS camera located in the focal plane of the telescope. The camera consists of 499 PMTs with light concentrators located in front of them (right). Image credits: VERITAS collaboration.

The PMT high voltage is provided by a multi-channel power supply which allows each PMT to be controlled individually. The PMTs are typically operated at a voltage of $700 - 800$ V which yields a nominal gain of $\sim 2 \times 10^5$. A high-bandwidth pre-amplifier is integrated into the base of the PMTs to provide an extra gain of 6.6 to the PMT signals. The pre-amplifier also provides a direct DC output for anode-current monitoring purposes (Nagai et al., 2007). It enables the detection of long-term changes in tube performance and is especially important during moonlight observations, when too high currents could result in a damage of the camera.

Signals from the pre-amplifier are transmitted to the trigger electronics and data acquisition system as it is schematically illustrated in Figure 3.4.

Trigger system

The VERITAS trigger system is designed to distinguish light coming from potentially gamma-ray initiated air showers from NSB as well as local muons. The trigger consists of three hierarchical conditions and is explained in detail in Weinstein et al. (2007).

The first trigger works on the single-pixel level (L1) and is a programmable constant fraction discriminator (CFD). It produces a 10 ns logic output pulse if the sum of the voltages from the PMT pulse and a time-delayed copy crosses a set threshold. Additionally, the VERITAS CFD design has a rate feedback (RFB) circuit that reduces timing jitter and stabilizes the CFD trigger rate in the presence of changing NSB levels (Hall et al., 2003).

After the CFD triggered, the logic pulse is sent as input to the camera-level trigger (L2). The L2 triggers an output pulse when several (typically three) adjacent pixels surpass the L1

discriminator threshold within a coincidence time window of about 6 ns. This camera-pattern trigger successfully rejects fluctuations due to NSB and PMT afterpulsing, and preferentially selects compact images from air showers.

A positive L2 trigger decision is sent to the array-level trigger (L3). The main purpose of the L3 is to reject local muons by requiring a trigger on multiple telescopes in the array. It requires typically two or more telescopes within 50 ns and ensures a stereoscopic view of the event. Since muons dominate the low energy background, a reduction of triggers due to muons enables a further reduction of the CFD threshold. Thus, it lowers the energy threshold of the telescope array at trigger level. When an L3 trigger occurs, a logic signal is sent back to all four telescopes which initiates the readout of the buffer by the DAQ system (see Figure 3.4). During this time no new trigger can be accepted; introducing a dead time to the system which is about 10% for an L3 trigger rate of 250 Hz.

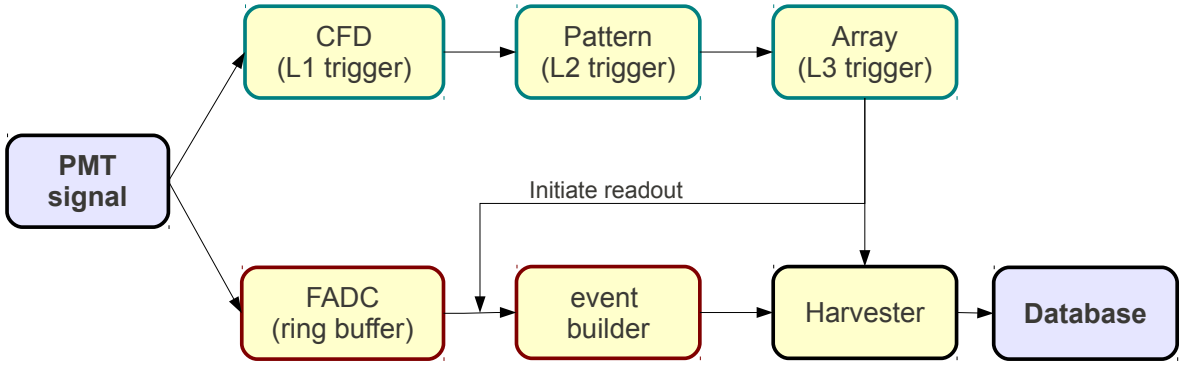

Figure 3.4.: Schematic view of the VERITAS trigger and DAQ system. Analog signals are sent from the camera PMTs to the three-level trigger system (upper part). A second copy of these analog signals is fed to the data acquisition system (lower part), where it is digitized and buffered until the readout is initiated by the L3 system and the events are assembled. The data is finally written to a database and archived. A description of each component is given in the text.

To estimate the settings for the best trigger conditions (i.e. low energy threshold, low NSB contribution, and stable rates), so-called "bias-curves" are taken (see Figure 3.5). Therefore, the trigger rates of each camera (L2) and the array trigger (L3) are recorded by the system in dependence of the L1 discriminator threshold. The optimal CFD trigger threshold is just above the inflection point; the point where the steeply falling NSB accidental rate and the relatively flat rate due to cosmic-ray background cross each other. For dark sky conditions the CFD thresholds for each pixel are set to $45 - 50$ mV, corresponding to approximately $4 - 5$ photoelectrons.

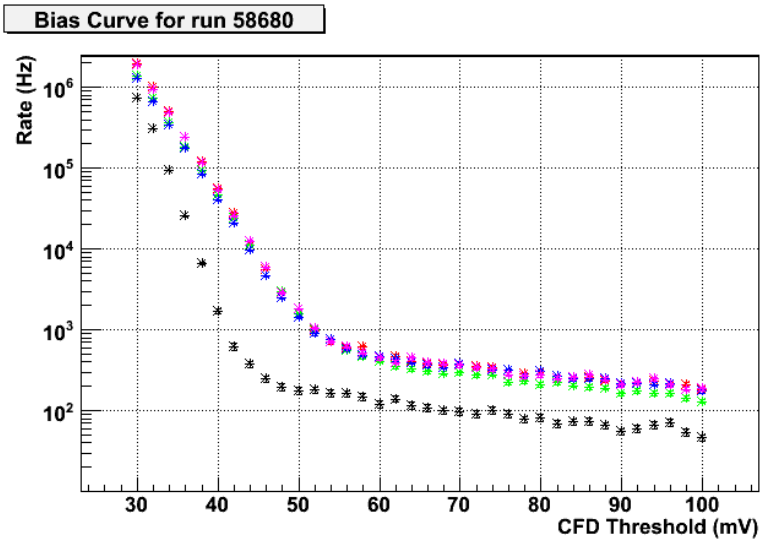

Figure 3.5.: Bias curve taken under dark sky conditions. Shown are the trigger rates in dependence of the CFD threshold. The black crosses are the L3 trigger rate and the colors represent the different L2 telescope rates (T1: red, T2: green, T3: blue, T4: magenta). One can clearly see the steeply falling NSB rate at very low thresholds and the nearly constant rate due to cosmic rays above 50 mV.

Data acquisition system

The core of the DAQ system (Hays et al., 2007, see Figure 3.4) is a 500 Mega-sample per second flash analog-to-digital converter (FADC[1]). These FADCs digitize continuously the analog PMT signal (Rebillot et al., 2003). A ring buffer holds the digitized information with a memory depth of 32 μs while awaiting an L3 trigger signal. When the L3 trigger signal is received, the DAQ system reads out a section of this buffer (typically 32 to 48 ns) for each PMT signal. By default, the signal traces follow the high-gain path to the FADC. If the signal saturates the 8-bit range of the FADC, an analog switch connects the FADC chip to a delayed low-gain path instead, thus extending the dynamic range from 256 to 1500 digital counts (dc).

The digitized signals from the FADC boards are then sent to a telescope-level event-building computer, where complete events are integrated, tested and passed to a data harvester machine. The harvester machine combines the telescope-level event information with array-level information from the L3 (e.g. event numbers and timing information) into a custom VERITAS data format and stores them on disk for later offline analysis.

[1] The benefit of FADCs over simple charge integrating ADCs is the possible application of digital signal processing techniques. They allow, for example, to dynamically place and minimize the charge integration window during the analysis, thus improving the signal-to-noise per PMT and lowering the effective energy threshold (Cogan et al., 2007).

As the events are being assembled, the observing conditions, such as the trigger settings and high-voltage values, are continuously recorded in a database. The database also records any changes in settings by observers and acquisition information for a given run including run types, source names or positions, selected trigger types and diagnostic information such as weather and PMT currents. The database is later queried for relevant details by the offline data analysis.

3.1.2. Calibrations

In order to understand the signal size and energy scale, calibrations (absolute and relative) are performed regularly. The absolute calibrations are used as input for the detector simulations to properly address the overall photon conversion factor while the relative calibrations measure the channel-to-channel variations which are applied later in the data analysis.

The overall photon conversion factor of a telescope is a combination of mirror reflectivity, collection and quantum efficiency of the PMT cathode, and the conversion factor of the electronic chain. The mirror reflectivity and the PMT photo cathode characteristics can be determined from laboratory measurements. The conversion factor of the electronic chain is measured in situ with an LED flasher system, providing a uniform and simultaneous illumination of the camera. It is used to determine the absolute gains in the camera by directly measuring the position of the single photo-electron peak in the pulse-size spectrum as described in Hanna et al. (2010).

To measure channel-to-channel variations, a short (5-minute) flasher run is taken each night to determine time differences and relative gains across the camera. The time differences between channels arise mainly from cable lengths and electronic delays. A typical distribution of the time offsets, relative to the arrival time of the flasher pulse in the whole camera, is shown in Figure 3.6 (left). This correction is applied to each channel during the data analysis. The relative gain calibration accounts for inhomogeneities in the amount of charge produced in each channel. It depends on the response of the light concentrator, the quantum efficiency of the photo cathode and the gain through the photomultiplier stages of each PMT. An example of the relative gain variations is shown in Figure 3.6 (right). These corrections are applied in the data analysis (see Section 3.2.2) in order to obtain a uniform camera response. In case that the RMS of the relative gain distributions is larger than $\sim 10\%$, the cameras are "flat-fielded". During this procedure, the high voltages of the PMTs are adjusted to equalize the PMT response to a uniform light source, resulting in a narrower spread in relative gain.

Auxiliary data

In addition to the camera calibrations the quality of the sky, i.e. the atmospheric conditions and the night-sky brightness, is continuously monitored and logged into the database. In this way,

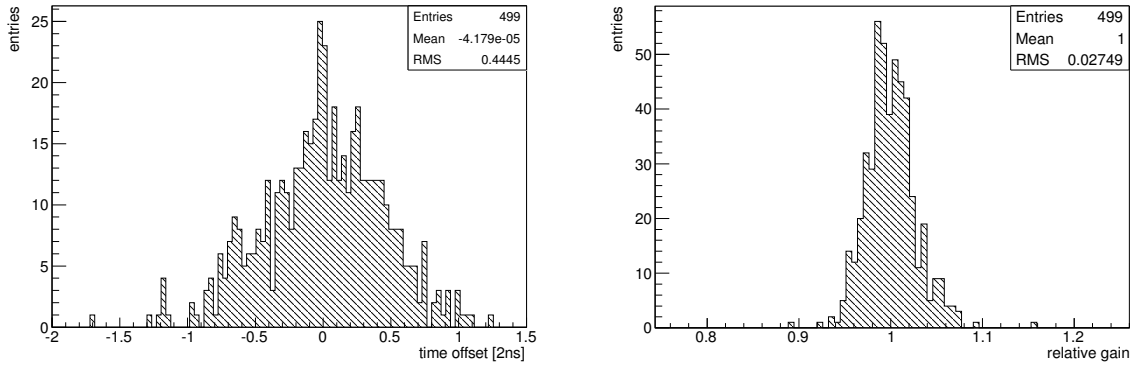

Figure 3.6.: Distributions of time offset (left) and relative gains (right) in the cameras as obtained for flasher run 56002 (Telescope 4). They are used in the analysis to correct for the inhomogeneities in the camera.

the operating conditions can later be retrieved to assist a correct interpretation of the data.

To quantify the quality of the atmosphere, the temperature of the sky is monitored using infrared pyrometers. As water vapor and droplets act as infrared emitters, a rise in sky temperature in the FoV of the pyrometers indicates the presence of clouds or haze. The pyrometers values are logged every 10 seconds to the VERITAS database and are used in the analysis to perform a run quality selection.

The brightness of the night sky is highly variable and depends on the observing conditions, such as the observed FoV or the presence of the Moon. To determine the pixel's response to the current NSB condition, the L3 system artificially triggers the readout at a rate of 1 Hz during normal data taking. These events, so-called pedestal events, are used in the analysis to provide a baseline measurement of the pixel behavior in the absence of Cherenkov light and to diagnose and remove problematic pixels.

3.1.3. Observations

VERITAS observations are usually carried out during clear, dark nights. This leads to a typical observation time per year of about 750 hours[2]. Most of the observations are taken in "wobble mode" where the source position is offset by 0.5° from the camera center to allow for simultaneous background measurements (Fomin et al., 1994). A typical run duration is about 20-30 minutes after which the wobble position is changed to another cardinal direction, or the telescopes are pointed to another source.

[2] It should be noted that VERITAS cannot observe in the summer months of July and August due to local monsoon. The instrument is shut down during this time to avoid damage to hardware and electronics.

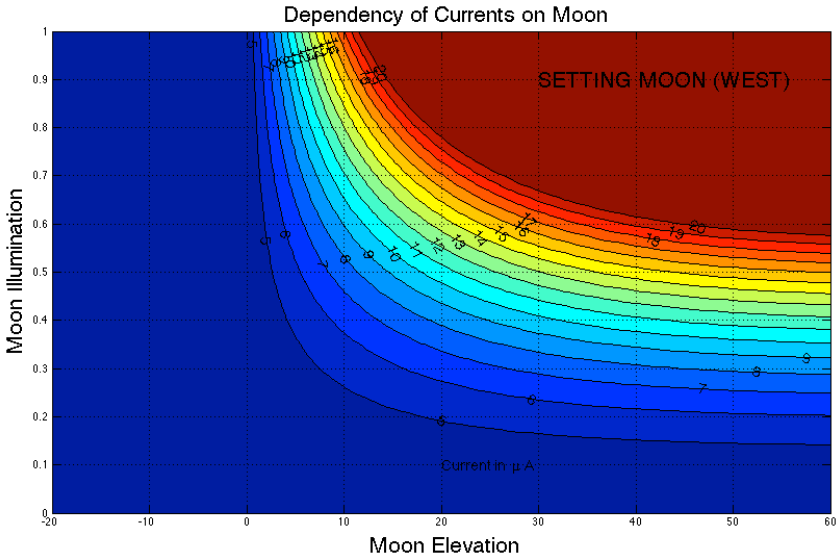

Figure 3.7.: Average currents (in μA) in the VERITAS cameras in dependence of the Moon phase (= Moon illumination) and the Moon elevation. Courtesy of Jeffrey Power.

To increase the duty cycle of VERITAS, observations are routinely carried out when the Moon is above the horizon. This increases the observation time by about 25% compared to dark nights only. The major restrictions for observations under moonlight are the influence of the increased NSB and a possible damage of the PMTs due to high currents. The NSB flux under moonlight conditions is highly variable and depends on the angle between the Moon and the telescope pointing direction as well as on the Moon phase and its elevation. This is illustrated in Figure 3.7 which shows the average currents in the cameras as a function of the Moon elevation and the Moon phase. For low Moon phases nearly no increase in the average currents is visible when the Moon is above the horizon. As the Moon gets more illuminated, the average currents rise and depend more and more on the elevation of the Moon itself. At some point, the currents are too high to safely operate the instrument and no observations are possible anymore. Depending on the average currents in the cameras different operation modes are defined within VERITAS, ranging from dark sky observations to a full moon break as described in Table 3.1.

Observation & scientific plans

The VERITAS Time Allocation Committee (TAC) is in charge of organizing the observation plan. This committee, consisting of representatives elected from the collaboration on a yearly basis, collects and ranks the submitted observing proposals. It also carries out the scheduling

Name	Description	Settings
Dark sky	Sun and Moon are below the horizon. The average currents in the camera depend on observations of extragalactic or brighter galactic sky patches and are around $4-7\mu$A, respectively.	50 mV CFD
Low moonlight	Typically up to a Moon phase of 35%; similar to dark-sky operations with average camera currents $\leq 10\mu$A.	50 mV CFD
Moderate Moon	Rising or setting bright Moon (phase $\geq 35\%$); operations with increased CFD trigger threshold to reduce NSB accidental rate; average currents in the camera are $10-15\mu$A.	60 mV CFD
Bright Moon	Moon phase approx. $35-65\%$; the high voltage (HV) is reduced resulting in reduced gains and lower camera currents.	85% HV
Very bright Moon	Moon phase is $\geq 65\%$; operations with reduced HV are not feasible anymore; special bandpass filter are employed which let only the UV light pass.	UV filter
Full Moon	No observations, typically 4 nights around full Moon.	NONE

Table 3.1.: VERITAS observation modes defined by the average currents in the cameras. The upper two are the standard observation modes and no differentiation in their hardware settings (i.e. their trigger settings) is made between them. The bright and very bright moonlight modes were introduced in 2012 and their performance evaluation is still ongoing.

of the overall observing program, taking into account the long-term Science Plan of VERITAS. This science plan is dedicated to the study of the physical processes responsible for gamma-ray emission in a large variety of sources and astrophysical environments. It is based on four major themes of scientific exploration (Galante et al., 2012):

1. *Particle Physics and Fundamental Physics Laws* including the following questions: What is the nature of dark matter? How is the distribution of dark matter in the Galactic halo? What are the constraints on physical laws at energies well beyond the reach of terrestrial accelerators (Lorentz invariance violation)? Search for primordial black holes and search for axion-like particles.

2. *Cosmology* with emphasize on constraining the epoch of re-ionization and the history of star and galaxy formation through gamma-ray opacity measurements as well as the study of cosmic rays in star-burst galaxies and ultra-luminous infrared galaxies.

3. *Black Holes* at the center of active galaxies are believed to power relativistic jets through

accretion of matter. How accretion and particle acceleration in active galactic nuclei (AGNs) works and if AGNs accelerate ultra-high-energy particles are among the still open questions around black holes.

4. *Galactic Tevatrons and Pevatrons* are studied to possibly identify the sources of cosmic rays in the Galaxy. They can be used to understand the mechanisms of particle acceleration (maybe up to PeV energies) and to obtain constraints on their magnetic fields.

In order to explore this wide range of science topics and open questions, many different objects are observed by VERITAS. Those include specifically (1) possible dark matter targets like spheroidal dwarf galaxies and the Galactic center; (2) gamma-ray bursts, galaxy clusters, and distant AGNs; (3) AGNs like blazars and radio galaxies; and (4) galactic sources like pulsars, pulsar wind nebulae, supernova remnants and binary systems. Most of these source classes have already been detected by VERITAS and show a large variety of photon fluxes and spectral behavior. A brief overview of VHE observations of AGNs, i.e. blazars, will be given in Section 5.1.2. The reader is referred to Holder et al. (2011) for a review of the scientific highlights of VERITAS.

3.2. VERITAS data analysis

The data analysis is based on Monte Carlo (MC) simulations which are essential in order to understand the measured signals and to reconstruct the properties of the primary particle from the detected Cherenkov light. The software package used within this thesis is `eventdisplay`. It was originally designed as display for the VERITAS prototype data by Gernot Maier (DESY) and Jamie Holder (University of Delaware), but evolved into a full analysis package.

In the following the VERITAS analysis chain is explained. It starts with a overview of the MC simulations used (Section 3.2.1) before the reconstruction is outlined. The reconstruction starts with the trace analysis and parameterization of the image in each camera (Section 3.2.2). The information from those camera images are combined to reconstruct the direction and energy of the event (Section 3.2.3). Afterwards, a gamma-hadron separation is performed (Section 3.2.4) and the signal is extracted (Section 3.2.5). Once the gamma-ray signal is obtained, the determination of the instrument response functions from MC simulations (Section 3.2.6) allows us to convert the count rate into a flux measurement of the astronomical object and to derive an energy spectrum and a light curve (Section 3.2.7).

3.2.1. Monte Carlo simulations

The MC simulations consist of two parts: the air shower development in the atmosphere including the emission of Cherenkov light and the detector response on these Cherenkov photons. The shower development is simulated with the CORSIKA program (version 6.960; Heck et al., 1998). For the Cherenkov light emission the IACT option is used (Bernlöhr, 2008b), in which the detectors are defined as fiducial spheres around a detector position. Any Cherenkov light intersecting these spheres is recorded. The VERITAS site specific parameters, like altitude, geomagnetic field and telescope positions, are used together with two different atmospheric profiles, corresponding to summer and winter atmospheres[3]. Corrections for atmospheric extinction are applied to the Cherenkov photons after the shower simulation. The systematic uncertainty due to the variations of the local atmosphere is estimated to $\sim 15\%$.

The number of recorded Cherenkov photons depends on the primary particle's energy, the angle of the incoming particle, the distance of the telescope to the impact point of the incident particle, as well as on the geomagnetic field. For this reason, the shower simulations used here cover several steps in zenith angle (from 0° to 65°), which can be observed with the VERITAS telescopes. The full range of azimuth angles ($0^\circ - 360^\circ$) is simulated due to the rather strong geomagnetic field at the VERITAS site which causes deflection of the particles within the air shower. Showers are simulated up to a radius of 750 m from the array center. Primary particles are gamma rays in the energy range from 30 GeV to 200 TeV, following an E^{-2} spectrum. During the analysis, the MC events are weighted to account for the difference between the simulated spectral shape and that of the potential source.

The detector simulation is done with the GrISU package[4] and is two-fold: the propagation of Cherenkov photons through the optical system and the response of the camera and electronics. The geometrical properties of the telescope are fully implemented, taking into account the mirror reflectivity, their surface roughness and random scatter in their alignment. Shadowing effects from the telescope structure are as well accounted for during the ray-tracing. In a second step, the electronics and readout are simulated. Cherenkov photons hitting a PMT produce a single photo-electron pulse which is digitized into 2 ns samples with a trace length reflecting the FADC properties. Noise arising from NSB photons is simulated seperately for different NSB conditions and is added to the trace during the analysis. The trigger simulation uses a simplified model of the CFD as the first stage and a full realization of the pattern trigger; requiring three adjacent pixels above threshold within 6 ns. The trigger threshold generally used is 50 mV; corresponding to about $4 - 5$ photo-electrons. It should be noted, that this simplified

[3] The two atmospheric profiles are models based on daily radiosonde measurements. See Appendix B.1 for a brief discussion on the transition between these two atmospheres.

[4] `http://www.physics.utah.edu/gammaray/GrISU/`

trigger model shows good agreement between data and simulations above the energy threshold. However, at lowest energies the trigger due to NSB photons have a significant contribution and need to be taken into account. This is realized with a new simulation package (CARE[5]) which is used for the performance studies of the PMT upgrade. The output of the telescope simulation, i.e. the FADC traces for all PMTs, are written to disk in the VERITAS specific raw data format. The input to the detector simulations are hardware specific parameters like the positions of the mirror facets and the PMTs as well as the absolute gain measurements, the pulse shape of a single photo-electron, and the quantum and collection efficiencies of the PMTs. A systematic uncertainty from the detector simulation is estimated to be $\sim 15\%$. The major uncertainties arise from the determination of the quantum efficiency and the mirror reflectivity; both time dependent and subject to differences between single devices.

Once the simulations are done, they are analyzed in the same way as the real data and are used to validate the different reconstruction steps as well as to obtain the instrument response functions needed for the flux determination. The overall systematic uncertainty on the flux is estimated to be $\sim 20\%$. This takes as well $\sim 5\%$ systematics into account which arise from the analysis (e.g., from the influence of dead pixels and differences between different analysis packages).

3.2.2. Image parameterization

In the first step of the analysis, the charge in each pixel is determined by a trace analysis, an image cleaning is performed to reduce the noise contribution and the remaining image is parameterized.

Trace analysis

Two typical FADC traces, as recorded by the VERITAS cameras, are shown in Figure 3.8. The left part of the figure corresponds to a signal from Cherenkov photons. It shows the typical pulse shape of a PMT and is characterized by a fast rise to a maximum value (recorded as negative values in digital counts) and a slightly slower decay back to a baseline value, so-called pedestal. The arrival time T_0 is defined as the time where the trace rises to half its maximum value. It is corrected for relative time differences in the camera (see Section 3.1.2). The right part of Figure 3.8 shows the absence of Cherenkov light in the PMT, fluctuating around the pedestal value. The pedestal is an artifical negative offset which is added to the analog PMT signal while the fluctuations arise mainly from NSB photons and electronic noise. To determine the pedestal

[5] CARE (CAmera and REadout) is a simulation package developed by Nepomuk Otte; `git clone http://www.gtlib.gatech.edu/pub/IACT/CARE.git`.

value, the externally triggered pedestal events (see Section 3.1.2) are analyzed by summing up the digital counts in each pixel. The mean of this charge distribution is the pedestal and is approximately 16 digital counts (dc). The charge in each pixel is finally determined by summing up the signal of each FADC trace within a given time window, subtracting its pedestal value and applying the relative gain corrections (Section 3.1.2).

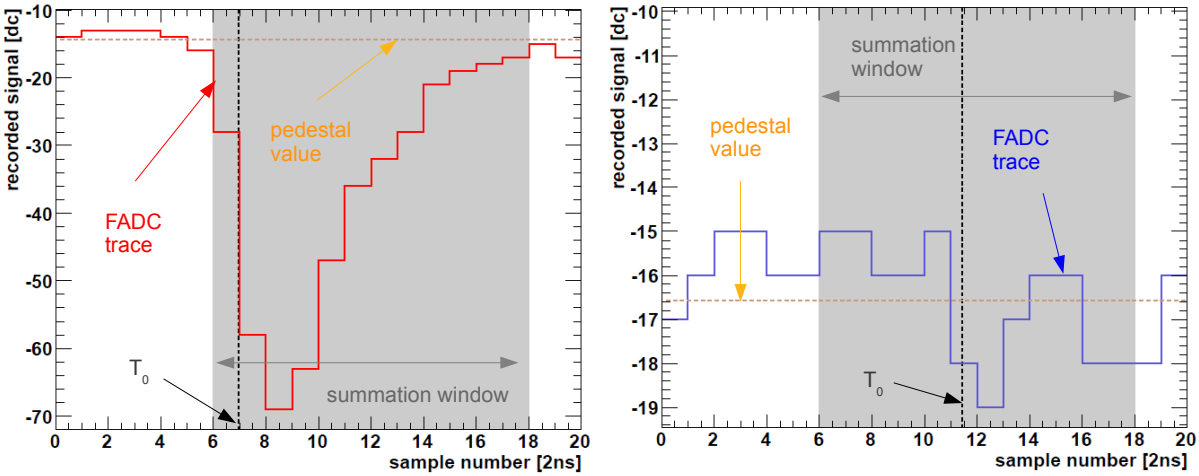

Figure 3.8.: Two typical FADC traces with a sampling rate of 500 Mega-samples per second (i.e. 2 ns). (Left) Temporal pulse profile in response to Cherenkov photons hitting the PMT. (Right) The FADC trace in the absence of Cherenkov photons shows only fluctuations around the pedestal value (note the different ranges on the y-axes). The horizontal lines represent the pedestal value while the vertical dashed lines indicate the arrival time T_0. The grey shadow indicates the summation window used in the analysis for the charge extraction.

To minimize the contribution from NSB photons[6] which are continueously recorded and digitized, a short summation window, covering the pulse from the Cherenkov light only, is used. This is typically done in two stages, so-called *double-pass method* (Holder et al., 2005). In the first stage, a wide integration window (typically 18 samples) is applied to each FADC trace and is used to calculate the charge and the arrival times. The resulting images are then cleaned and parameterized (as described in the next sections). In a second stage, a smaller integration window (typically 7 or 12 samples) is positioned upon every trace in the camera. To determine the optimal position of the short integration window, the temporal development of the air shower has to be taken into account. Therefore, the arrival times as a function of the PMT position

[6] For dark-sky observations of a Crab Nebula-like FoV, approximately 0.13 photo-electrons/ns from the NSB are recorded. This number can increase dramatically when the Moon is above the horizon.

along the major axis (determined from the first-stage image parameterization) are fitted by a straight line. The slope of this fit is the *time gradient* and its value is used to define the start position of the integration window in the second stage. This method allows to use short integration windows with optimal signal-to-noise ratios for small pulses and at the same time prevents signal losses due to significant time gradients in large, far distant showers.

Image cleaning

After the charge in each pixel is determined, an image cleaning is performed. It removes random background fluctuations from the compact shower image by applying tail cuts. These tail cuts can be either fixed or are based on the signal-to-noise ratio in each pixel[7]. The main motivation to use variable tail cuts is that the NSB conditions during a typical observation run can change, especially when operating under moonlight conditions. Therefore, every pedestal event within a given time slice (typically three minutes) is selected and the RMS of the pedestal distribution (its *pedvar*) is determined. This *pedvar* is proportional to the NSB (noise) level as the pedestal events characterize the pixel behavior in the absence of Cherenkov light signals.

To determine whether a given pixel belongs to the shower image is done in two stages. In the first stage, each pixel with a charge greater then 5 times its *pedvar* is selected and forms an *image pixel*. In a second stage, a lower cut value of 2.5 times the *pedvar* is used with the condition that at least one of the neighboring pixels is already identified as an image pixel. If this cut is passed, the pixel belongs to the shower image and forms a *border pixel*. In case, an image pixel does not have any neighbor pixel surviving the cleaning procedure, it is removed as well. The remaining image and border pixels then define the image of the Cherenkov shower.

Hillas parameterization

Once the shower images have been calibrated and cleaned, each image is parameterized. The parameterization is based on the so-called Hillas parameters (Hillas, 1985). They are derived by the zeroth order (amplitude or size), first order (center of gravity) and second order (length, width, orientation) moments of the elliptical image of the shower and are listed in Table 3.2. These parameters describe the shape and the orientation of the image in the camera and are calculated using the formulas given in Fegan (1997).

As images at the edge of the cameras are difficult to reconstruct with this method, they are usually excluded from the analysis by cuts on the distance between the camera center and the image centroid or the *loss* parameter (the fraction of image size contained in edge pixels).

[7] In VERITAS, the signal-to-noise ratio is used while for the CTA analysis (see Section 4.3.2) fixed cleaning thresholds are applied.

Parameter	Short description
size	Total intensity of the image = sum of the integrated charge of all pixels (relates to the energy of the primary particle).
width	The rms spread of charge deposit along the minor axis of the image (relates to the projected lateral development of the cascade).
length	The rms spread of charge deposit along the major axis of the image (relates to the projected longitudinal development of the cascade).
centroid	Coordinates of the center of gravity of the image in the camera (θ_x, θ_y).
distance	The distance from the centroid of the image to the center of the field of view of the camera.
fui	The fraction of image size under the image ellipse. (can be used to remove less compact images)
loss	The fraction of image size contained in edge pixels. (can be used to remove strongly truncated images at the camera edge)

Table 3.2.: Image parameters describing the shape and the orientation of the image in the camera.

These quality cuts result in improved energy and angular resolution at the expense of less reconstructed gamma-ray events at multi-TeV energies. To recover those truncated images at the edge of the camera, a simple log-likelihood fitting algorithm is applied (Maier, 2010). The underlying assumption of the fitting method is that the image of a gamma-ray shower can be described by a two-dimensional normal distribution. Asymmetry is ignored to limit the number of fit parameters which are image centroid position, image width, image length and image size. Noise is estimated by assuming Poisson fluctuations. The starting values for the fit parameters are obtained from the standard image analysis. The following expression is minimized using the MIGRAD method of MINUIT (James, 1998):

$$L = -\sum (n_i \ln S_i - S_i - n_i \ln n_i + n_i) \tag{3.1}$$

where n_i is the measured integrated charge for pixel i, and S_i is the estimated charge from the fit function. In general, this log-likelihood reconstruction method works well for loss values smaller than 50%. It results in an increase of effective area at high energies compared to the standard analysis.

3.2.3. Event reconstruction

Image quality cuts

Before the event is reconstructed, quality cuts are applied to the parameterized images. These include a minimum number of image/border pixels ($N > 4$), a minimum image size ($size >$ 400 dc) and a maximum loss value ($loss < 0.5$). Furthermore, a minimum number of three telescope images is required.

Geometrical reconstruction

The reconstruction of the direction of the event is based on the stereoscopic approach and follows in principal algorithm 1 in Hofmann et al. (1999). The direction of the shower is obtained by superimposing the camera images into a single camera plane coordinate system, as illustrated in the left part of Figure 3.9. As the major axis of the camera image represents the shower axis, the intersection point of the major axes corresponds to the shower direction in camera coordinates. It is determined from a weighted average of the intersection of all pairs of major axes. The weights include the sine of the angle between two axes, the size of the images, and the ratio of width-over-length from each image. In this way more weight is given to high quality (i.e. brighter and more elongated) image pairs.

Then the shower core, needed for the energy reconstruction and the gamma-hadron separation, is reconstructed. This parameter is defined in the plane perpendicular to the arrival direction of the shower (the shower plane) and corresponds to the position where the incoming gamma ray would have hit the ground. For each camera, the axis passing through the center of gravity of the image and the reconstructed source position is projected into the shower plane, as illustrated in Figure 3.9 (right). The intersection point between the different image axes is determined and the shower core position is then given by the weighted average of the intersection of all pairs. The distance from the shower core to a given telescope position within the shower plane coordinate system is the so-called *impact parameter*. As far distant showers tend to produce parallel images, the angular resolution[8] worsens as a function of impact parameter. To avoid this problem, a cut on the shower core position of 250 m from the array center is applied.

In addition to the direction and shower core, the *emission height* of the shower can be calculated (Aharonian et al., 1997). The emission height refers to the point in the development of the air shower which contains the maximum number of Cherenkov emitting particles. This parameter is pair-wise calculated and the final value is the mean of all telescope pairs weighted by the corresponding image size. Additionally, the χ^2-value is determined. Both parameters can

[8] The angular resolution is defined as the angular distance from a point-like source position within which 68% of the reconstructed gamma-ray events are contained.

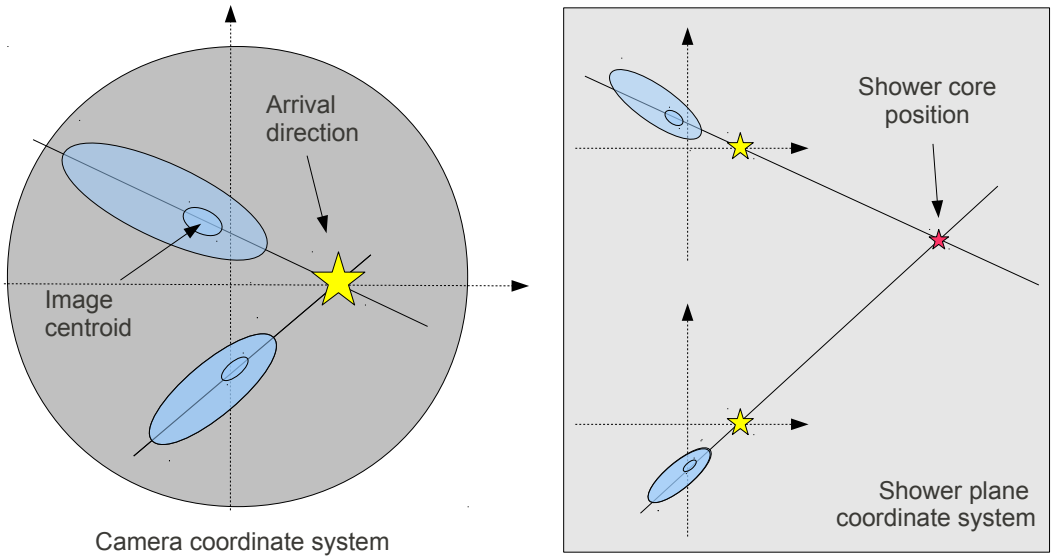

Figure 3.9.: Reconstruction of the direction and core position of an air shower using the stereoscopic approach. (Left) By superimposing the two camera images into a single camera coordinate system, the direction of the shower can be reconstructed by intersecting the major axes. (Right) The shower core position corresponds to the intersection point of the straight lines passing through the reconstructed arrival direction and center of gravity of the image and is defined in a plane perpendicular to the shower arrival direction.

be used as background discriminant since hadronic showers and single muons penetrate deeper into the atmosphere than gamma-ray initiated showers.

Energy reconstruction

The energy reconstruction exploits the fact that the energy of a gamma-ray initiated air shower is proportional to the number of Cherenkov photons within the air shower. The energy is therefore related to the total charge contained in the image (*size*) and depends on the observing conditions, i.e. the shower direction (zenith, azimuth, wobble offset), the impact parameter, and the NSB level. To cover this wide parameter space, the energy estimation is based on gamma-ray MC simulations using so-called lookup tables. These lookup tables are filled with the median and the 90%-width (σ) values of the logarithm of the image size as a function of the primary gamma-ray energy and the impact parameter. An example of both for a fixed shower direction and NSB level is shown in Figure 3.10.

For each telescope image, an energy estimate E_i is derived by inverting the lookup table of the

median, weighted by $1/\sigma_i^2$. As the simulations are done in finite steps of zenith angle, wobble offset and NSB level, the estimated values are obtained by interpolating between the results from the different tables. The energy of the event E_{event} is finally determined by averaging the energy estimates from all N telescopes, weighted by one over the square of the 90%-width value:

$$E_{\text{event}} = \frac{\sum_{i=1}^{N} E_i/\sigma_i^2}{\sum_{i=1}^{N} 1/\sigma_i^2} \tag{3.2}$$

Additionally, the χ^2-value of the energy estimation is derived

$$\chi^2(E_{\text{event}}) = \frac{1}{N-1} \sum_{i=1}^{N} \left(\frac{E_{\text{event}} - E_i}{\sigma_i^2} \right) \tag{3.3}$$

which can later be used in the gamma-hadron separation. It exploits the fact that the energy estimates from the individual images differ much more for the irregular hadronic showers then for the regular, compact gamma-ray images.

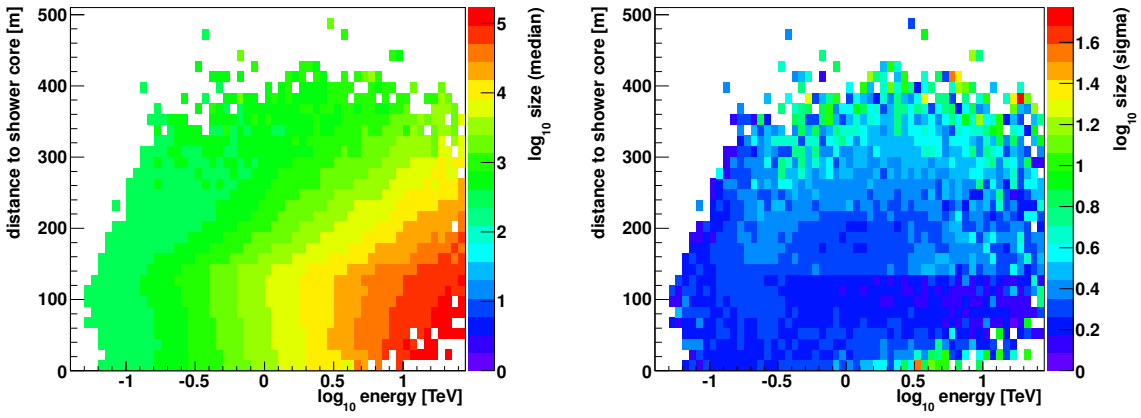

Figure 3.10.: Lookup table for the median (left) and the sigma value (right) used for the energy estimation of the reconstructed event. Both tables are shown for 20° zenith angle, a noise level corresponding to observations of a Crab Nebula-like FoV, and a wobble offset of 0.5°. The number of filled bins at low energies is limited by the requirement of the minimum number of pixels per image and at high energies by MC statistics and the finite size of the camera. At large impact distances, the decreasing Cherenkov photon density is the limiting factor for the detection of the shower and hence the filling of the lookup table with MC events.

3.2.4. Gamma-hadron separation

Once the event is reconstructed, the challenge is to seperate the gamma-ray primary from the much more numerous background events (see Section 2.2.2). This is done by cuts on the image shape and arrival direction of the events[9].

Shape cuts

The shape of the image is parameterized with the width and length parameters. As both parameters depend on the energy of the primary particle, the shower direction (and impact parameter) and the NSB level, lookup tables based on gamma-ray MC simulations are used. The lookup tables contain the median and the 90%-width values of the expected image width ($w_{MC}, \sigma_{\mathrm{width},MC}$) or length ($l_{MC}, \sigma_{\mathrm{length},MC}$) as a function of impact parameter R and the image size s. From these lookup tables, the mean-scaled width is derived as

$$MSCW = \frac{1}{N_{images}} \sum_{i=1}^{N_{images}} \left(\frac{\mathrm{width}_i - w_{MC}(R,s)}{\sigma_{\mathrm{width},MC}(R,s)} \right) \tag{3.4}$$

and similar for the mean-scaled length. By this definition, the mean-scaled parameters for gamma-ray showers are centered on zero and are normal distributed. As hadronic showers are less compact and more irregular, their images are longer and most notably wider then gamma-ray showers. Hence, the $MSCW$ and $MSCL$ distributions of the primaries are different, as shown in Figure 3.11. The cut values to discriminate background from signal events have been determined *a priori* by optimizing the sensitivity to detect a source with 5% of the flux of the Crab Nebula. They are listed in Table 3.3.

3.2.5. Signal extraction

To remove the isotropic cosmic-ray background, a cut on the arrival direction θ, defined as the angle on the sky between the assumed source position and the reconstructed shower direction, is applied. The cut value itself depends on the analyzed source. For a standard point-source analysis it is $\theta^2 < 0.008\,\mathrm{deg}^2$ while for extended (galactic) sources this value is in general larger. Together with the shape cuts, a background rejection of more than 99.5% can be achieved for a point-source analysis. These cuts, used later in this thesis, are summarized in Table 3.3.

[9] Cuts on the emission height and its χ^2-value as well as the χ^2-value of the estimated energy are additionally used in the CTA analysis (see Section 4.2.3).

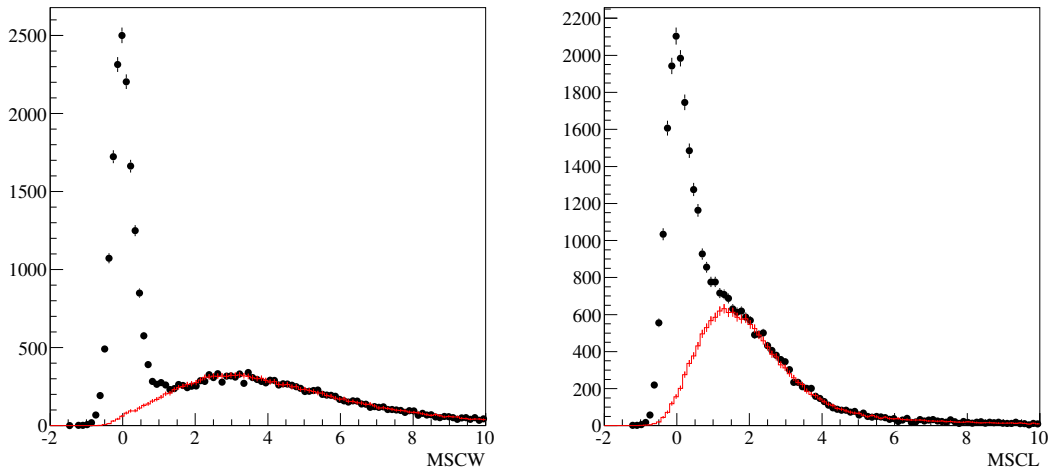

Figure 3.11.: Event distribution of the mean-scaled parameters as obtained from an analysis of the Crab Nebula (y-axis are the number of events). The black points show all reconstructed events in the ON region and the peak around zero arises from gamma-ray events. The red curves show events from the OFF regions and arise from background events. Hadron-initiated showers are thus much longer and most notably wider than gamma-ray initiated showers (see Section 3.2.5 for explanation of ON and OFF regions).

Estimation of the remaining background

The remaining background consists of gamma-like cosmic-ray events. To determine the statistical excess of gamma rays at the source position, the irreducible background has to be estimated. Therefore, the reconstructed shower direction for each gamma-ray-like event is filled into a so-called sky map. Within this sky map, two regions are defined: an ON region and an OFF region. The ON region is defined by a circular region of radius θ and is centered on the potential source position. For the OFF region, two different models are usually used: the reflected-region or the ring-background model. Both background-region models are illustrated in Figure 3.12 (see, e.g., Berge et al., 2007).

In the reflected-region model, the background is estimated using several circular regions (same size as the ON region) equidistant from the pointing position. The combined events from these regions are used to estimate the remaining background, scaled by the relative area between ON and OFF regions. As the OFF regions are at the same distance from the center of the camera as the ON region, no correction for the relative camera acceptance is required. The camera acceptance, as shown in Figure 3.13 worsens with increasing distance to the camera center and is, in general, assumed to be radial symmetric.

Image quality cuts	Moderate source cuts
minimum number of tubes > 4	distance of core position to telescope < 250 m
minimum size ≥ 500 dc	distance from the camera center $< 1.50°$
maximum loss cut ≤ 0.50	angular distance: $\theta^2 < 0.008$ deg^2
minimum fraction under image < 0.60	mean-scaled width: $-1.2 < MSCW < 0.35$
	mean-scaled length: $-1.2 < MSCL < 0.7$

Table 3.3.: Moderate source cuts used for the VERITAS data analysis of point sources.

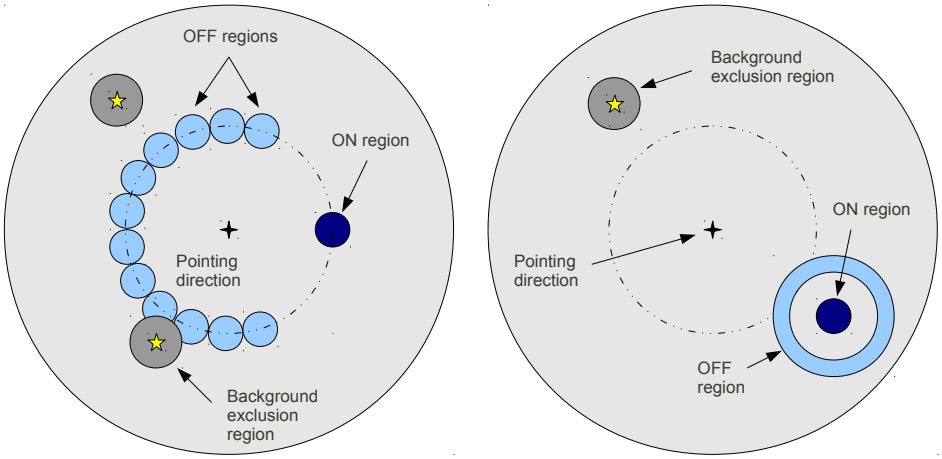

Figure 3.12.: Background estimation using the reflected-region model (left) and the ring-background model (right).

In the ring-background model, the OFF region is defined as a ring placed around the ON region. The radii of the ring are chosen such that the ratio between ON and OFF area is approximately 1:10. The normalization α is given by the area ratio modified by the radial acceptance of the camera. Such a radial acceptance curve (see Figure 3.13) can be obtained from gamma-ray-like events or MC simulations. The agreement between MC simulations and data is well up to camera distances of 1.5°. Therefore, a cut on the relative distance of the reconstructed event from the camera center of 1.5° is applied in the VERITAS data analysis.

By comparing the number of events in the ON region (N_{ON}) with the normalized number of events in the OFF region (N_{OFF}), the number of excess events,

$$N_{excess} = N_{ON} - \alpha N_{OFF}, \tag{3.5}$$

can be determined. To avoid possible under- or over-estimation of the background, regions

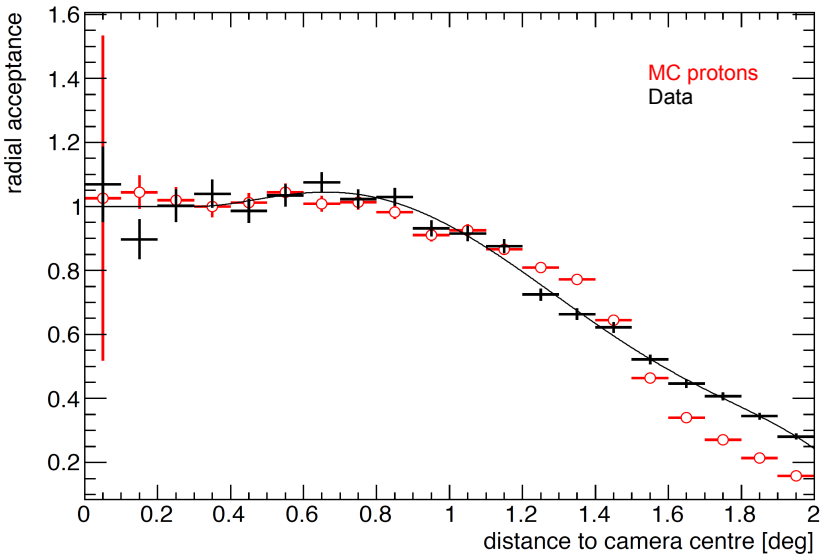

Figure 3.13.: Radial acceptance curve for the VERITAS camera as obtained from gamma-ray-like events (black) and proton MC simulations (red). It is assumed, that the acceptance in the camera is symmetric in azimuth.

around known gamma-ray emitters as well as bright stars (V magnitude brighter than 7) are excluded from the background regions. The resulting detection significance of the excess is calculated according to Eq. 17 in Li & Ma (1983) and is

$$S = \sqrt{2}\left\{ \mathrm{N_{ON}} \ln\left[\frac{1+\alpha}{\alpha}\left(\frac{\mathrm{N_{ON}}}{\mathrm{N_{ON}}+\mathrm{N_{OFF}}}\right)\right] + \mathrm{N_{OFF}} \ln\left[(1+\alpha)\left(\frac{\mathrm{N_{OFF}}}{\mathrm{N_{ON}}+\mathrm{N_{OFF}}}\right)\right]\right\}^{1/2}. \quad (3.6)$$

For the significant detection of a gamma-ray point source, the traditional requirement is a five standard deviation statistical significance ($S \geq 5$, usually denoted as "5σ"). Once the significance of the excess is determined, the excess events in the source region can be converted into a photon flux (or flux upper limit) by estimating the instrument response to photons of any given energy. This is done with the computation of effective areas as explained in the following.

3.2.6. Effective areas & energy threshold

The effective area describes the efficiency of the instrument for detecting gamma rays. The detector efficiency is derived from gamma-ray simulations that are fully propagated through the

data analysis chain. The effective area is defined as

$$A_{\text{eff}}(E) = (\pi\, R^2)\, \frac{N_{\text{selected}}(E)}{N_{\text{simulated}}(E)} \tag{3.7}$$

where πR^2 is the simulated area (in the shower plane) over which the impact points of the primary particle are uniformly distributed, N_{selected} are the number of showers which are selected, and $N_{\text{simulated}}$ is the number of showers simulated. In general, N_{selected} can be the number of events which trigger the telescopes or the number of events which pass the selection cuts. For the flux calculation, the effective area is calculated from the number of showers after cuts. It should be noted that the effective area depends on several observing parameters, i.e. the zenith and azimuth angle, the pointing offset from the source position and the background noise level, but as well on the applied cuts.

Typical effective area curves as function of reconstructed energy are shown in Figure 3.14 for different zenith angles. At energies above approximately 1 TeV, the effective area is relatively flat and of the order of $10^5\,\text{m}^2$. At energies below 1 TeV, the effective area drastically decreases; showing a strong dependence on the zenith angle. This can be understood in terms of shower development since low-energy showers develop early in the atmosphere and create much less Cherenkov light than high-energy showers. This emitted light has to travel a much longer path through the atmosphere for large zenith angles and the probability of photons getting absorbed is much higher than for low zenith angles.

The energy threshold can be defined as the peak in the differential counting rate assuming a Crab Nebula-like photon spectrum, as listed in Appendix A. In Figure 3.14, the energy threshold corresponding to the different zenith angles is given. One can clearly see, that it increases with increasing zenith angle. This makes it especially important to observe gamma-ray sources with a steep spectrum like blazars at low zenith angle to obtain the lowest possible energy threshold.

3.2.7. Flux determination and spectral reconstruction

The effective area allows to convert any measured count rate into a flux from the gamma-ray source. The integral flux Φ above the energy E_{thr} is defined as the number of particles per unit area per unit time,

$$\Phi(E > E_{\text{thr}}) = \frac{N}{T\,\langle A\rangle} \tag{3.8}$$

where $\langle A\rangle$ is an averaged effective area over the whole integrated energy regime. To obtain the averaged effective area, it is assumed that the source spectrum follows a spectral shape,

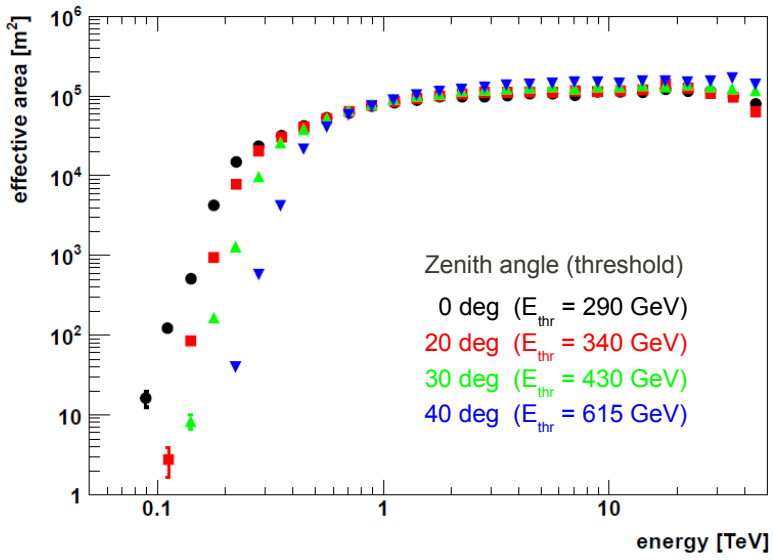

Figure 3.14.: Effective areas for the VERITAS array for moderate source cuts. The curves are shown for different zenith angles as a function of reconstructed energy and the energy threshold E_{thr} is given in the legend. It is defined as the peak in the differential counting rate assuming a Crab Nebula-like photon spectrum. The curves correspond to a Crab Nebula-like spectrum with a pointing offset of 0.5° and a noise level corresponding to observations of a galactic FoV.

expressed as

$$\phi(E) = \phi_0 \left(\frac{E}{E_0}\right)^{-\alpha} \tag{3.9}$$

where ϕ_0 is the normalization constant, E_0 a given normalization energy, and α is the photon spectral index. Assuming no change in spectral shape during the observation time, the flux can be calculated as follows:

$$\Phi(E > E_{thr}) = \frac{N(> E_{\mathrm{thr}})}{N_{theory}(> E_{\mathrm{thr}})} \times \int_{E_{\mathrm{thr}}}^{\infty} \phi_0 \left(\frac{E}{E_0}\right)^{-\alpha} dE \tag{3.10}$$

where $N(> E_{\mathrm{thr}})$ is the number of excess events (or the upper limit on the number of excess events) above the given energy threshold, and $N_{theory}(> E_{\mathrm{thr}})$ is the expected excess using the assumed spectral shape. It is given by

$$N_{theory}(> E_{\mathrm{thr}}) = t_{\mathrm{obs}} \times \int_{E_{thr}}^{\infty} \phi_0 \left(\frac{E}{E_0}\right)^{-\alpha} A_{\mathrm{eff}}(E) dE \tag{3.11}$$

where t_{obs} the dead-time corrected observing time and $A_{\mathrm{eff}}(E)$ is the effective area at the given energy. It should be noted that the resulting flux values depend on the assumed spectrum since the effective area has to be averaged over a finite energy bin width and the finite energy resolution will lead to spill-overs where events will migrate from one energy bin to another.

In order to produce a differential photon spectrum of the source, the flux is determined in energy bins whereas the bin width is at least the energy resolution of the instrument. The basic requirement used within this thesis is that the statistical significance (calculated using Eq. 3.6) of a spectral point has to be at least 2σ, otherwise an upper limit (using the method of Helene, 1983) is used to represent the flux measurement. A power-law function is then fitted to these discrete flux measurements and the associated errors to obtain the differential source spectrum.

To determine the temporal evolution of the source, especially important for transient sources like AGN, the integrated flux versus time is calculated. This is a so-called light curve and can be produced with different binnings (e.g. nightly, monthly, or yearly). When the time bin does not contain enough number of events an flux upper limit is derived using the method of Helene (1983).

3.3. The VERITAS camera upgrade

In summer 2012, the PMTs in each of the cameras have been replaced to lower the energy threshold and improve the overall sensitivity of VERITAS. The new photon detectors are 1-inch PMTs of Hamamatsu (type R10560-100-20; hereafter called R10560). They have a UV glass entrance window and a super-bialkali photo cathode resulting in a considerably higher quantum efficiency than classical bialkali photo cathodes used before. The hardware characteristics have been discussed in Otte et al. (2011) and Kieda et al. (2011). In this section, the study of the camera upgrade, carried out before the installation of the new PMTs, is presented with focus on the estimation of the overall and the low-energy performance.

3.3.1. Simulations of the VERITAS upgrade

To estimate the performance of the VERITAS array after the camera upgrade, the new PMTs are characterized and implemented into the MC simulation chain. The main differences of the new PMTs compared to the Photonis PMTs used before summer 2012 are the photon detection efficiency (PDE) and the pulse shape. Both are shown in Figure 3.15.

The Hamamatsu PMTs are significantly faster than the Photonis XP2970. The single photo-electron pulse shape has a full width at half maximum (FWHM) of 4.2 ns for the R10560, which is about 40% narrower than the pulse shape of the XP2970 (6.8 ns). This narrower pulse shape

can, for example, be used to improve the signal-to-noise ratio in the analysis by reducing the summation window in the trace analysis.

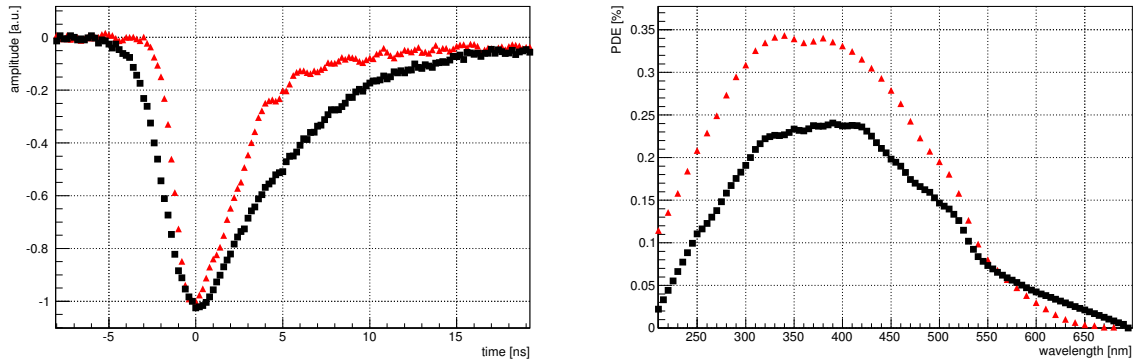

Figure 3.15.: Characterization of the PMTs as used in the simulations. (Left) Pulse shape produced by a single photo-electron. (Right) Photon detection efficiency as a function of wavelength. Black squares are before the upgrade (XP2970), red triangles are after the upgrade (R10560). Curves are obtained from measurements performed at UCSC and WashU (VERITAS Collaboration).

The PDE of both devices shows a typical curve. The efficiency increases up to wavelengths of about 320 nm, reaches a plateau, and decreases again at wavelengths larger than $400 - 450$ nm. This shows that the PMTs are very sensitive in the UV to blue wavelenght regime, where the Cherenkov photon spectrum on ground has its maximum (as shown in Figure 2.6). At longer wavelengths, the sensitivity decrease of the PMTs has the advantage that the detection of light from the NSB is also reduced as its contribution increases at wavelengths longer then 400 nm (see e.g. Hampf et al., 2011). To quantify the increase in efficiency, the performance values for both PMTs at 320 nm are usually compared. For the XP2970 PMT (before the upgrade), the PDE-value is 23% while the efficiency for the Hamamatsu devices is at 34%. Folding the PDE curve with the Cherenkov light spectrum in the focal plane of a VERITAS telescope, on average 23% of the Cherenkov photons will be detected with the R10560 PMT, which is a 35% higher light yield than that of the Photonis XP2970.

As with the higher light yield also the recording of NSB by the camera increases, the trigger thresholds have to be adjusted in order to cope with the higher NSB. The NSB trigger rate as a function of the trigger threshold is simulated; equivalent to taking a bias curve during normal operations. For the simulations a Crab Nebula-like NSB level is chosen, which is 130 MHz per pixel for the Photonis PMTs and 175 MHz for the Hamamatsu PMTs; the latter accounting for the 35% higher light yield. Under the assumption that the accidental telescope trigger rate

after the installations of the new PMTs is kept at 1 kHz (as prior to the upgrade; Figure 3.5), the obtained CFD threshold is 65 mV for the Hamamatsu PMTs and is kept at 50 mV for the Photonis PMTs. The camera trigger condition, i.e. three adjacent pixels within 6 ns, is kept for the upgrade simulations.

Once the trigger thresholds are determined, a full set of MC simulations is set-up for the upgrade and pre-upgrade array. The PMT characterizations (PDE, pulse shape and afterpulsing) are implemented into the detector simulation program. The photon conversion factor is kept the same as before the installation of the new PMTs, assuming that the new PMTs will be operated at the same nominal gain of $\sim 2 \times 10^5$. All simulations are done at a zenith angle of 20° with a pointing offset of 0.5°; the standard operation in VERITAS performing best at lowest energies. Simulated primary particles include gamma rays, protons and electrons.

3.3.2. Performance estimation

In Figure 3.16 the gamma-ray detection efficiencies on trigger level are shown. One can clearly see an increase in effective area at low energies (< 300 GeV) with the high-quantum efficiency PMTs compared to the Photonis ones. This directly translates into a lower energy threshold at trigger level. It is about 95 GeV with the Photonis PMTs and reduces down to approximately 75 GeV with the Hamamatsu PMTs, as obtained from the peak in the differential counting rate. Thus, the installation of the new PMTs in the cameras enables the detection of gamma-ray showers of much lower energy as more Cherenkov photons can be recorded. On the other hand it should be noted, that the array trigger rate due to cosmic rays will also increase (from about 250 Hz up to approximately 500 Hz). Without any changes to the readout, this will introduce a dead time of the order of 20% to the system[10].

In order to evaluate possible improvements in the overall performance after the camera upgrade, the simulations are analyzed with `eventdisplay`. To take advantage of the 40% shorter pulses after the upgrade the summation window in the trace analysis is reduced from 7 samples to 5 samples. This almost immediately cancels out the increased NSB contribution in the integrated charge per pixel. Further on, no cut optimization has been performed for the new PMTs and cuts used are similar to those of a standard point source analysis (as listed in Table 3.3), but without an image size cut.

The results of the analysis, i.e. the effective areas for gamma rays after cuts, are shown in Figure 3.17. At lowest energies, the lower energy threshold of the new PMTs leads to a clear increase in effective area while at higher energies the effective area is similar before and after the

[10] In order to reduce the dead time of the system several possibilities have been tested during the camera commissioning phase in fall 2012. Those included a shorter trigger coincidence time window and a reduced readout window, resulting at a dead time of about 15% for trigger rates of ~ 450 Hz.

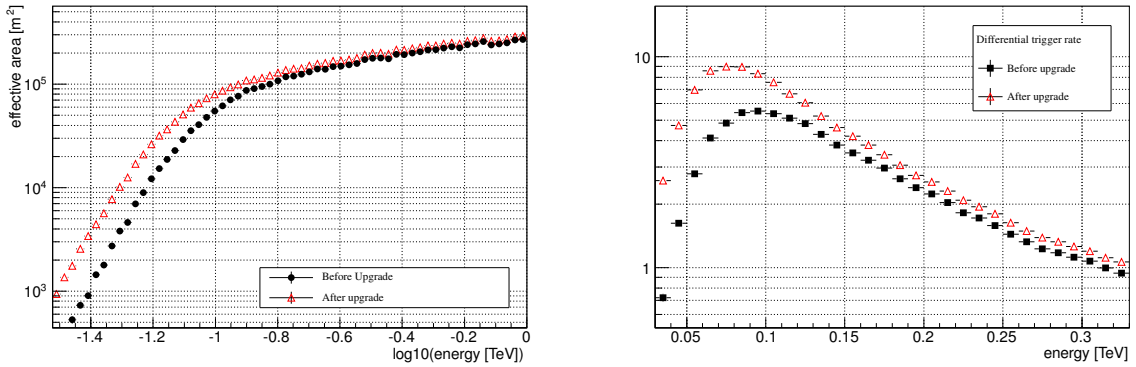

Figure 3.16.: Effective area and differential counting rate on trigger level assuming a Crab Nebula-like spectrum. Black squares are before the upgrade (XP2970), red triangles are after the upgrade (R10560).

upgrade. It should be noted that at energies above ~ 30 TeV, the drop in effective area is related to the finite size of the VERITAS camera and the maximum distance cut of 250 m, applied to avoid nearly parallel images which worsen the geometrical reconstruction of the event.

Another way to look at the improvements of the camera upgrade is to determine the sensitivity of the array. Traditionally, the representation of the sensitivity is in terms of integral sensitivity, including all events reconstructed above a given energy within an observation time of 50 hours. This representation is highly dependent on the source spectrum and thus might be misleading. A different way to represent the sensitivity of VERITAS (and later as well of CTA) is in terms of differential sensitivity. The differential sensitivity represents the lowest flux in a given energy bin which results in a significant detection after a certain observation time t_{obs}. It is calculated in small energy bins, i.e. five bins per decade in energy are used within this thesis. An observation time of $t_{\mathrm{obs}} = 50$ hours and a signal-free background region five times larger than the signal region ($\alpha = 0.2$) are assumed in the following. The basic requirements for a significant detection per bin are a 5σ statistical significance, at least 10 events and the number of gamma rays is 5% above the background rate. They can be summarized as follows:

$$\begin{aligned} S &\geq 5 \\ N_\gamma &\geq 10 \\ N_\gamma / (\alpha \cdot N_{\mathrm{OFF}}) &\geq 0.05 \end{aligned} \tag{3.12}$$

To obtain the differential sensitivity, a Crab Nebula spectrum for the gamma rays is assumed

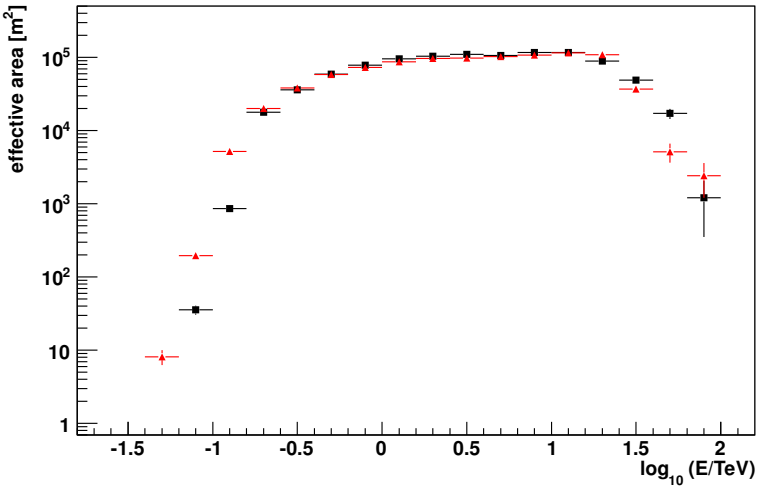

Figure 3.17.: Effective area for gamma-ray simulations at 20° zenith angle after analysis cuts. Black squares are before the upgrade (XP2970), red triangles are after the upgrade (R10560).

following the HEGRA measurements while proton and electron spectra are weighted according to measurements as listed in Appendix A. The errors in the sensitivity calculation are derived from the uncertainties in the gamma-ray and cosmic-ray background effective areas. The resulting sensitivity curve, multiplied by E^2, is shown in Figure 3.18. Even without a re-optimization of the cuts for the new PMTs, the sensitivity over the whole energy range is slightly increased for the high-quantum efficiency PMTs compared to the Photonis PMTs before the camera upgrade.

At the lowest energies, the increase in effective area (shown in Figure 3.17) and the lower energy threshold for the new PMTs results in an additional low energy bin in the sensitivity curve. The main limiting factor in this energy regime are the fluctuations in the air-shower development and hence the background. However, for short duration phenomena like flares from AGN or pulsed emission from pulsars, the increase in effective area will enable the detection of more gamma-rays which will lead to better flux estimates at lowest energies.

At moderate energies (between 300 GeV and 2 TeV), no increase in gamma-ray effective area could be achieved with the new PMTs but an improved sensitivity can be seen. This can be understood in terms of background rejection power. Due to higher light yield of the new PMTs, also more Cherenkov photons from background events (i.e. protons) are recorded and the images surviving the image cleaning are longer and wider. This makes a background rejection with shape cuts more efficient. In this energy regime, further improvements are expected after a proper cut optimization.

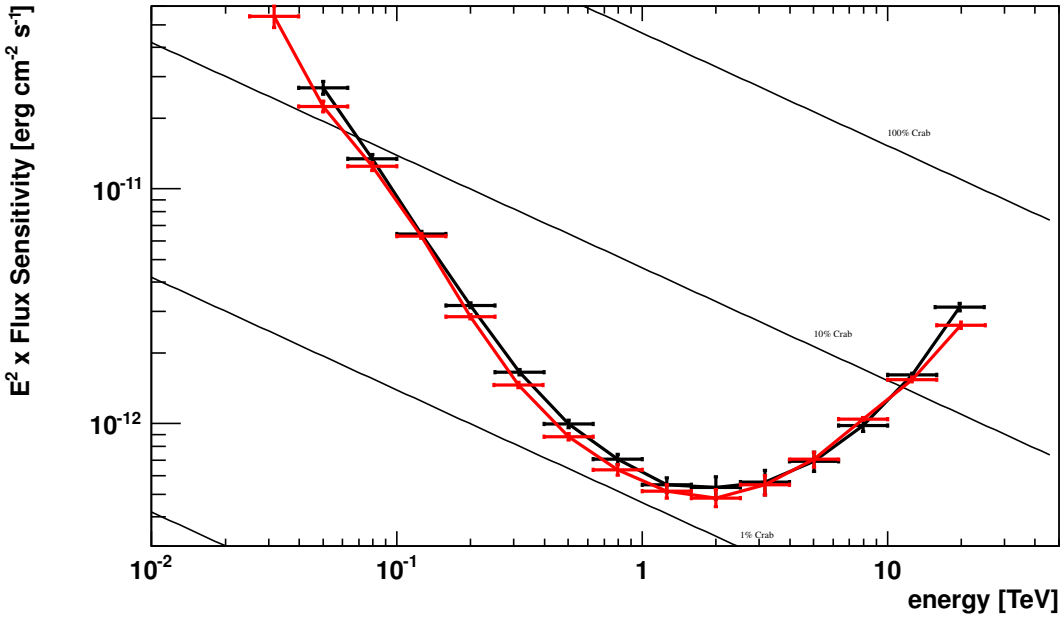

Figure 3.18.: Differential sensitivity curve of the VERITAS array for 50 hours of observations using the standard requirements given in Eq. 3.12. Simulations at 20° zenith and background includes cosmic-ray protons and electrons; cuts are not optimized cuts for the new PMTs. Black curve corresponds to before the upgrade (XP2970), red curve to after the upgrade (R10560).

At high energies (above a few TeV), neither the sensitivity curves nor the effective areas before and after the upgrade show significant deviations from each other. In this energy range, the sensitivity of the array is photon statistics limited and improves inversely proportional to the observation time. A possible improvement in this energy regime from the high-quantum efficiency PMTs might arise from the detection of farther distant showers, but this effect has not been investigated as a cut on the maximum distance from the array of 250 m has always been applied.

4. The Cherenkov Telescope Array (CTA)

The CTA project is an initiative to build the next-generation ground-based gamma-ray instrument. The design foresees a factor of 5-10 improvement in sensitivity in the current VHE gamma-ray domain of about 100 GeV to some 10 TeV, and an extension of the accessible energy range from well below 100 GeV to above 100 TeV, going far beyond of what can be reached by upgrading existing IACTs. The general concept of CTA is briefly presented in Section 4.1. To determine the arrangement and characteristics of the future CTA telescopes Monte Carlo (MC) simulations are employed. An overview of the simulated layouts used within this thesis is given in Section 4.2 where the baseline performance of CTA is also characterized. One of the basic assumptions in this standard set of simulations is that observations are carried out under dark sky conditions. Those dark sky conditions lead to about 1000 hours of observation time per year. An increase in observing time can be achieved when observations under partial moonlight are considered additionally. To explore the feasibility of these observations in terms of expected performance, a modified MC production has been set-up and analyzed by the author. It is presented in Section 4.3 and compared to the baseline performance.

4.1. The concept of CTA

The concept of CTA builds on the proven technique of IACTs (see Section 2.2). Through the deployment of the order of 50 to 100 telescopes, CTA aims to make significant progress over the existing experiments and further explore the Universe in the VHE regime (Actis et al., 2011). It will consist of two sites, one in the southern and one in the northern hemisphere, allowing full-sky coverage and, consequently, access to more potential VHE gamma-ray sources. For the first time in this energy range, CTA will be operated as an open observatory and will provide tools and support for data analysis to the astronomy and astroparticle-physics community.

4.1.1. Performance goals

The performance of CTA is driven by the scientific goals and motivations of the field (e.g., Hinton & Hofmann, 2009; Aharonian et al., 2008). A comparison between the scientific goals, costs and technical availability lead to the following performance goals (Acharya et al., 2013):

Sensitivity. CTA aims to be about a factor of ten more sensitive than any existing instrument in its energy range. As a consequence it will allow for the detection and in-depth study of a large number of known source types, it will explore a wide range of classes of suspected gamma-ray emitters and be sensitive to possible new phenomena that lie beyond the sensitivity of current instruments. From 100 GeV to several TeV, CTA intends to have a sensitivity a factor of one thousand below the flux of the strongest steady source of VHE gamma rays, the Crab Nebula.

Energy range. Broad coverage of the electromagnetic spectrum is crucial to understand the physical processes occurring in VHE sources. With a single facility CTA is aiming to cover four orders of magnitude in energy, from a few tens of GeV to a few hundred TeV, again a factor of ten more than any existing instrument. This will enable astrophysicists to distinguish between key hypotheses such as the leptonic or hadronic origin of gamma-ray emitting sources.

Angular resolution. Current instruments are able to resolve extended sources like SNRs, but they cannot probe the fine structures visible in other wavebands. As with CTA a gamma-ray-induced cascade is detected simultaneously by many telescopes, CTA intends to reach an angular resolution in the arc minute range, a factor of five better than the typical values for current instruments. This will help to identify possible counterparts at other wavelengths and may even allow the localization of VHE emission region(s) in some nearby AGNs.

To achieve an optimal performance over the full energy range considered, different telescope types are needed and the instrumentation has to be optimized in energy sub-ranges. In general, one can think about three different energy ranges: *the low energies* ($\leq$ 100 GeV), *the medium or core energies* (100 GeV$-$10 TeV), and *the high energies* ($>$ 10 TeV).

In the low-energy range, the event rates are high and the few photons from showers with energies down to a few tens of GeV can be efficiently detected with closely placed large size telescopes. The area of this part of the array can be relatively small, being of the order of a few 10^4 m^2. The major challenge in this energy regime is the reconstruction of the small images, the contamination by NSB photons and the gamma-hadron separation.

In the medium-energy range, the deployment of several tens of telescopes over a wide area will provide an array size which will be much larger than the Cherenkov light pool of a shower. This ensures that images will be uniformly sampled across the light pool and that a number of images are recorded close to the optimum distance from the shower axis (about $70 - 150$ m), where the light intensity is large and intensity fluctuations are small. The improved sensitivity

in this energy regime is obtained by the increased area covered, the higher quality of the shower reconstruction and improved background rejection.

In the high-energy range, the key limitation is the low gamma-ray flux and thus the number of detectable gamma-ray showers. Two implementation options can be considered: either a large number of small telescopes with mirror areas of a few m^2 and spacing matched to the size of the light pool of 100−200 m, or a smaller number of medium size telescopes which can see showers up to distance of ≥500 m, and can hence be deployed with a spacing of several hundred meters.

Determining the arrangement and characteristics of the CTA telescopes is a complex optimization problem, requiring a balance of cost against performance in different energy bands. In order to do this, Monte Carlo simulations have to be carried out which will be explained in detail in Section 4.2.

4.1.2. Technological concept

As the concept of CTA builds mainly on proven techniques, the major challenge is the large number of telescopes, i.e. their reliability, their maintainability as well as their construction on site. Current design efforts consider three telescope implementations: large size telescopes (LSTs), medium size telescopes (MSTs), and small size telescopes (SSTs) as shown in Figure 4.1.

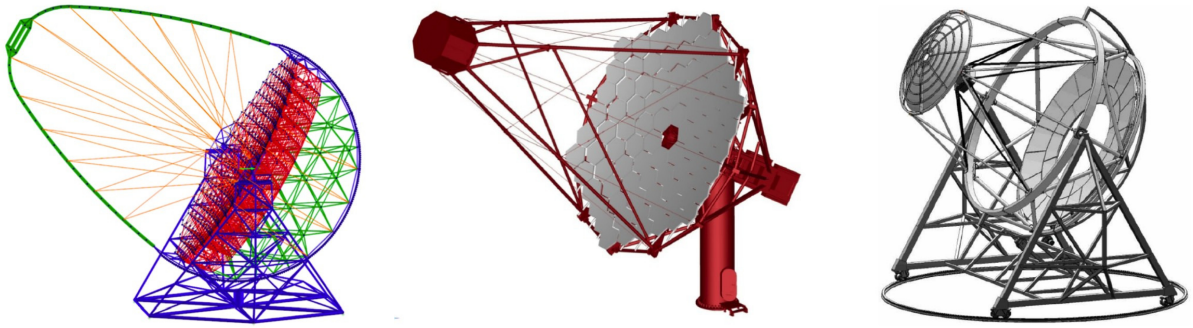

Figure 4.1.: Baseline design for the CTA telescopes; not to scale. (Left) Large size telescope with a 23 m diameter parabolic dish. (Middle) Medium size telescope with a 12 m diameter dish structure. (Right) Schwarzschild-Coude design for a possible MST or small-size telescope. Images taken from Acharya et al. (2013).

The LST design is similar to the MAGIC design, i.e. optimized for best performance at the lowest possible energy threshold. It consists of a 23 m diameter reflector. The optical dish structure is parabolic in order to keep the time dispersion smaller then the intrinsic time spread of the shower. Additionally, the LST is designed to be of a light-weight structure for fast re-pointing to catch transient sources like GRBs.

The MST in its current design is a 12 m reflector with 7-8° FoV, operating in the medium-energy range of CTA. Its optical dish structure is intermediate between Davies-Cotton and parabolic designs and combines the advantages of both designs, i.e. good imaging properties as well as small time dispersion. A full-scale mechanical prototype has been built in Berlin-Adlershof (Bähr et al., 2012). In addition, CTA is exploring a design for a dual-mirror MST of Schwarzschild-Couder (SC) optics (Vassiliev & Fegan, 2007). This allows to reach a large FoV (10°) with a very small camera size. The small size of the camera allows for finer pixelation and the use of cheaper photo sensors in the camera. As this is a new concept for IACTs, a prototype will be constructed at the VERITAS site to prove its viability.

Several concepts for the SST design are currently being explored with the aim of combining a large field of view ($\sim 10°$) with a good resolution of the shower images, as well as minimizing costs. One concept is of Davies-Cotton optics with a 4 m diameter reflector equipped with a fully digital camera based on Geiger-mode avalanche photo diodes (GAPDs), as pioneered by FACT[1]. Another concept is based on SC optics, which uses a secondary mirror to reduce the camera size and allows for a wide field of view with a light-weight camera, e.g. using GAPDs or multi-anode PMTs (e.g., Niemiec et al., 2013; Zech et al., 2013).

Altogether, CTA is now in the middle of a three-year preparatory phase aimed to be "construction ready" towards the end of 2014 after which the five-year construction phase will be started (Figure 4.2) at the candidate sites. Sites under consideration are located in Argentina, Namibia and Chile in the southern hemisphere and on the Canary Islands, in Arizona, Mexico, China and India in the northern hemisphere. Currently, all sites are being investigated in terms of geographical, observational and environmental conditions while additionally the local infrastructure and accessibility are considered. A site selection is anticipated in late 2013.

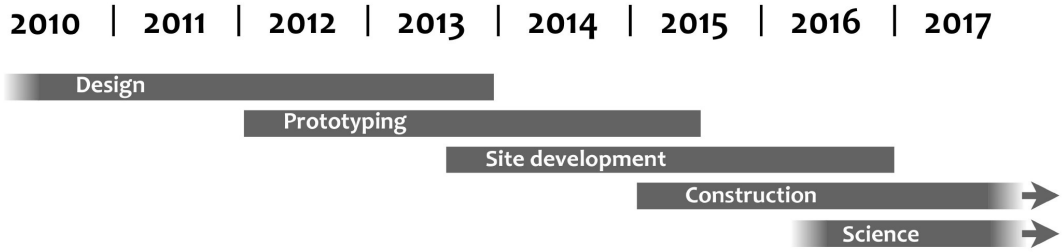

Figure 4.2.: Current timeline of the CTA project. Taken from Acharya et al. (2013).

[1] http://www.isdc.unige.ch/fact/

4.2. CTA Monte Carlo simulations

MC simulations of CTA are crucial to understand the performance and optimize the design prior to construction. The major challenge is to find an optimum[2] configuration which depends on the general design layout of the array (including telescope sizes and locations), but also on more technical aspects like telescope optics, camera field-of-view, pixel size, trigger logic and readout schemes. This is addressed by the simulation of a large array intended as a superset of many different candidate array layouts, known as CTA production-1. The configuration parameter choice is based on the technical design studies and the estimated costs involved. Before the array configuration is presented (Section 4.2.2) and the baseline performance of the configuration is evaluated (Section 4.2.3), the MC simulation chain is introduced briefly in the following.

4.2.1. Shower & detector simulation

The simulation of an IACT array consists of two parts: the simulation of the air shower development and emission of Cherenkov light by the shower particles and the detection of light and the recording of the signal by the detector. The CTA simulation chain is described in Bernlöhr (2008a).

The shower simulations are done with CORSIKA (version 6.735; Heck et al., 1998) using the IACT option for the Cherenkov light emission. The altitude of the CTA observatory is set to 2000 m (typical for several sites under consideration) with a geomagnetic field strength intermediate between that found in southern Africa and the Canary Islands. All showers are simulated at 20° zenith angle and primary particles include gamma rays, electrons and protons. The air shower simulations are generally carried out following an E^{-2} spectrum and the events are weighted in the analysis to achieve results equivalent to other spectral shapes.

The recorded Cherenkov photons are then passed to the detector simulation program, termed `sim_telarray` (Bernlöhr, 2008b). The simulation of the detector response includes the optical ray-tracing of the photons from the mirrors to the PMTs in the camera, the electronics and the digitization of the signals, as well as the trigger and readout system. Noise arising from NSB and electronics are added to the signal.

[2] The optimum configuration can be understood as the one which gives the best performance results within the given budget of CTA. As the "best" performance depends on the different physics cases, e.g. very low energy threshold for AGNs as well as sensitivity to the highest energies for cosmic-ray accelerators like SNRs, this task is non-trivial.

4.2.2. The production-1 configuration

Much of the work from early CTA MC studies by Bernlöhr et al. (2007) laid the foundations for what became known as the CTA production-1 array configuration, with the goal to characterize the performance of as many, and as varied, CTA candidate configurations as possible.

The production-1 configuration consists of 275 telescopes with five different telescope types and different spacings between the telescopes (Bernlöhr et al., 2013). The layout is shown in Figure 4.3. In the center of the array ten large-size telescopes (LSTs) are located with separation distances of about 60 to 200 m. This allows us to test the performance of subsets of two to six LSTs with different spacings in the low energy domain. Around the center, a large number of medium-size telescopes (MSTs) are placed covering a large area and wide range of possible spacings. This is needed to explore the trade-off between event quantity (large area coverage) and event quality (high telescope multiplicity) in this core energy range. To explore the high-energy domain, a multi-km^2 collection area is needed. Two possible solutions are implemented in the 275-telescope configuration: small-size telescopes (SSTs) with moderate spacing and widely spaced medium-size telescopes with a wide field-of-view (MST-WFs). These telescopes are arranged around the MSTs with grid-like and island-like layouts incorporated.

The main parameters of the different telescope types used in the simulations are summarized in Table 4.1. In addition, the most crucial assumptions for the production-1 are the following (denoted as the "standard" or "dark sky" production-1):

Parameter	Type 1 (LST)	Type 2 (MST)	Type 3 (SST)	Type 4 (MST-WF)
Diameter D (m)	24.0	12.3	7.4	12.3
Dish shape‡	parab.	DC	DC	DC
Mirror area (m^2)	412	100	37	100
Focal length f (m)	31.2	15.6	11.2	16.8
f/D	1.30	1.27	1.51	1.36
FoV diameter (deg)	5	8	10	10
Camera diam. (m)	2.8	2.2	2.0	2.2
No. of pixels	2841	1765	1417	1417
Pixel diam. (deg)	0.09	0.18	0.25	0.27

Table 4.1.: Geometrical parameters of the four main telescope types assumed in the CTA MC simulations (Bernlöhr et al., 2013).
‡ Parabolic or Davies-Cotton (DC).

Night sky background. The flux of the NSB assumed in the simulations corresponds to an extragalactic sky and is $\phi = 2.2 \cdot 10^{12}\,\text{photons}\,\text{m}^{-2}\,\text{s}^{-1}\,\text{sr}^{-1}$ (Preuss et al., 2002). This

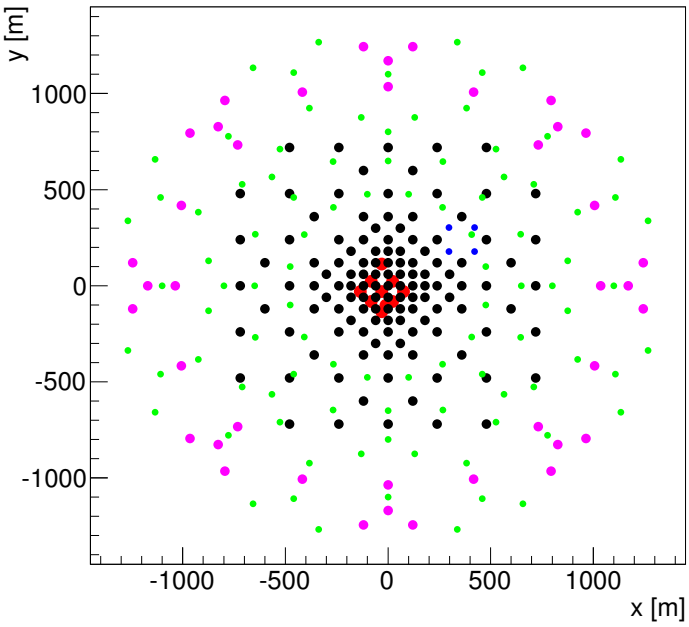

Figure 4.3.: The 275-telescope configuration used in the simulations described here. LSTs are shown in red, MSTs in black, SSTs in green, wide-field MSTs (MST-WFs) in magenta, and the four blue points represent a 4-telescope test set-up not used within this thesis. Their geometrical parameters are given in Table 4.1.

results in a NSB rate of the order of 100 MHz per pixel, i.e. one photo-electron per 10 ns. The NSB is assumed to be uniform across the whole camera.

Trigger. To suppress accidental camera triggers from the NSB, a 3-level-trigger scheme is used. In the first level, it is required that the signal in a pixel exceeds a certain (discriminator) threshold q. In the second level, a camera trigger is formed if at least three neighboring pixels (out of seven pixels on a hexagonal grid) passed the given threshold within a certain time window[3]. The threshold q is adjusted such that the camera trigger rate due to pure NSB events remains lower than 100 Hz for each camera type. Finally, an array trigger is applied before the readout is initiated, requiring at least two camera triggers from the same telescope type within a given time window[4].

[3] The coincidence time window for the camera trigger is 3 ns for LSTs, 6 ns for MSTs and 16 ns for the SSTs and MST-WFs. It is matched to the temporal development of the shower in the different energy regimes.

[4] The coincidence time window for the array trigger is 120 ns for LSTs, 300 ns for the closely placed MSTs, and 800 ns for the SSTs and MST-WFs, again matched to the temporal development of the shower.

Readout. For the readout scheme, a set-up similar to the H.E.S.S. telescopes is chosen, with two channels at a factor of 15 different gain, each read out by 12-bit ADCs at a frequency of 1 GHz. Sixteen samples (i.e. 16 ns) are added up in an integration window defined by the moment when the camera trigger fired.

In order to estimate the performance of CTA, candidate-array layouts (of comparable cost) are selected out of the 275-telescope configuration. Three of the possible candidate arrays are shown in Figure 4.4: Array B, C, and E. Array B consists of five LSTs with a 5° FoV and 37 MSTs with a FoV of 8°. This array is fairly compact and would be a low-energy implementation of CTA. Array C on the other hand is covering a wide area, consisting of 27 MSTs (8° FoV) surrounded by 26 wide field-of-view (10°) MSTs. No LSTs are included as the focus lies on the exploration of the high-energy regime. The Array E consists of four LSTs (4.6° FoV) in the center, 23 relatively closely spaced MSTs (8° FoV) and is surrounded by 32 SSTs with 10° FoV. This candidate array can be considered as balanced across the full energy range.

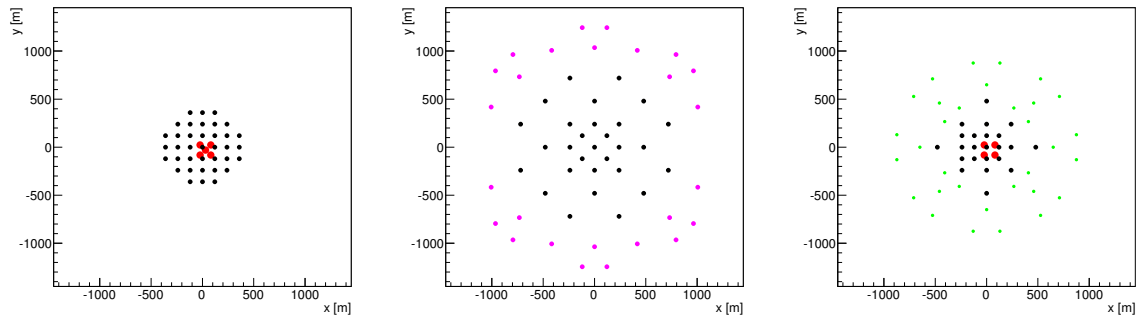

(a) Array B (b) Array C (c) Array E

Figure 4.4.: Layout of the three CTA candidate arrays used in this thesis. LSTs are shown in red, MSTs in black, SSTs in green, and MST-WFs in magenta.

4.2.3. Baseline performance of production-1

In the following, the analysis of these "standard" simulations is demonstrated on Array E using the performance curves provided by G. Maier. The results are discussed here and serve as reference for the later comparison with the performance under moonlight conditions.

Analysis description

To determine the performance of CTA production-1, the MC simulations are analyzed using the `eventdisplay` package. The relevant analysis steps are (Maier, 2011): (1) conversion of

the simulation output from `sim_telarray` to `eventdisplay` format, (2) parameterization of the image and reconstruction of the event, (3) gamma-hadron separation (using TMVA methods), and (4) determination of instrument response functions and sensitivity estimation.

In the converter, the candidate arrays are selected out of the 275-telescope configuration. Afterwards, the images in the cameras are parameterized as explained in Section 3.2.2. As only ADCs are simulated in the CTA production-1, no trace analysis is needed and the signals are the integrated charges within a time window of 16 ns. The image cleaning is a fixed two-stage tail-cut cleaning which will be explained in more detail in Section 4.3.2. Image quality cuts are applied (listed in Table 4.2) before the event is reconstructed (see Section 3.2.3). To account for the differences of the different telescope types, the lookup tables for the energy estimation and mean-scaled parameters are filled for each telescope type separately.

Parameter	LST	MST	SST	MST-WF
image cleaning tail cuts [pe]	11.0/5.5	11.0/5.5	9.2/4.6	16.8/8.3
minimum number of pixels per image	> 4	> 4	> 3	> 4
maximum loss value	≤ 0.2	≤ 0.5	≤ 0.5	≤ 0.5

Table 4.2.: For each telescope type, the image cleaning tail cuts are listed as image/border (in photo-electrons) and the quality cuts on the minimum number of pixels per image and the maximum loss value are given.

The major difference compared to the VERITAS data analysis is the gamma-hadron separation. Due to the wide energy range covered, the cuts are optimized in dependence of the reconstructed energy of the event. The cut on the arrival direction θ is set to the angular resolution (80% containment radius) after quality cuts. For the optimization, boosted decision trees (BDTs) as implemented in the TMVA package[5] are used. The BDTs are trained and applied in several overlapping energy bins (typically 12 bins while the best suited energy bin is chosen for each event). The different input variables for the optimization are: mean-scaled width (*MSCW*) and length (*MSCL*), second largest image amplitude per events (*SizeSecondMax*), χ^2-value of the energy estimate (*EChi2*), height of the maximum emission (*EmissionHeight*), and χ^2-value of the emission height estimation (*EmissionHeightChi2*). Their distributions for gamma rays and protons are shown in Figure 4.5 and Figure 4.6 for low energies ($E < 60\,\mathrm{GeV}$) and high energies ($E \approx 10\,\mathrm{TeV}$), respectively.

The BDT output is a single cut variable in the interval -0.5 to 0.5. The optimal cut is selected at the value giving the highest significance, assuming a Crab Nebula-like gamma-ray spectrum and a proton background spectrum as listed in Appendix A. Figure 4.7 shows the signal and

[5] `http://tmva.sourceforge.net/`

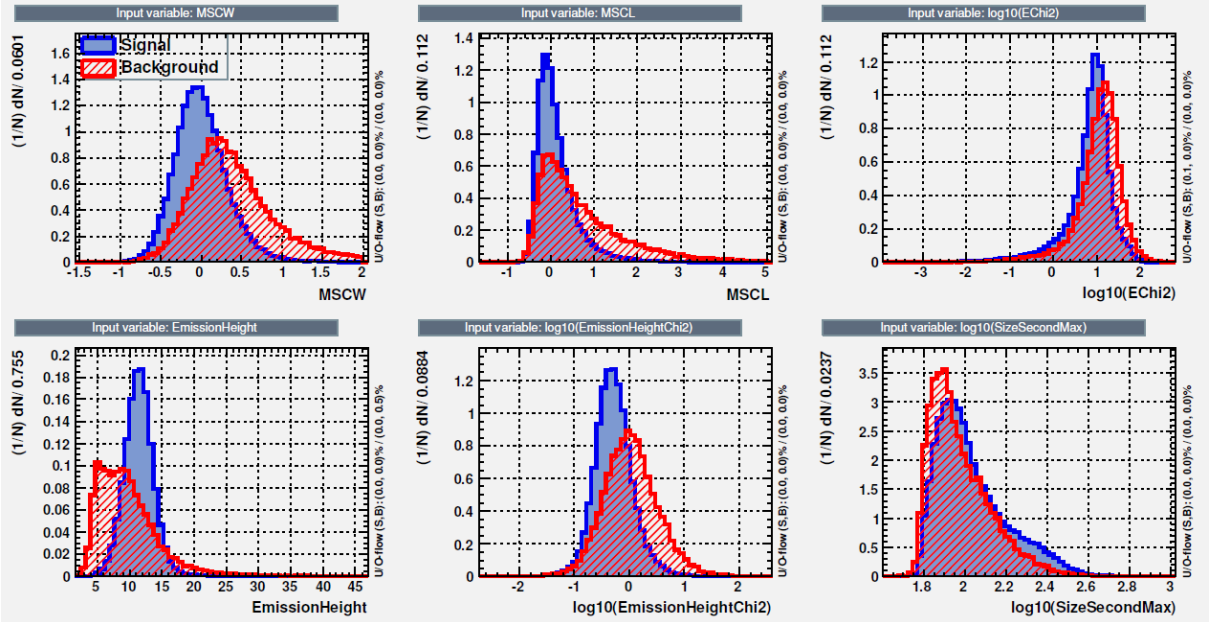

Figure 4.5.: Distribution of cut variables for events with low energies ($E < 60\,\mathrm{GeV}$). Signal events (blue) are simulated gamma rays, background events (red) consist of protons only. Figure taken from Maier (2011).

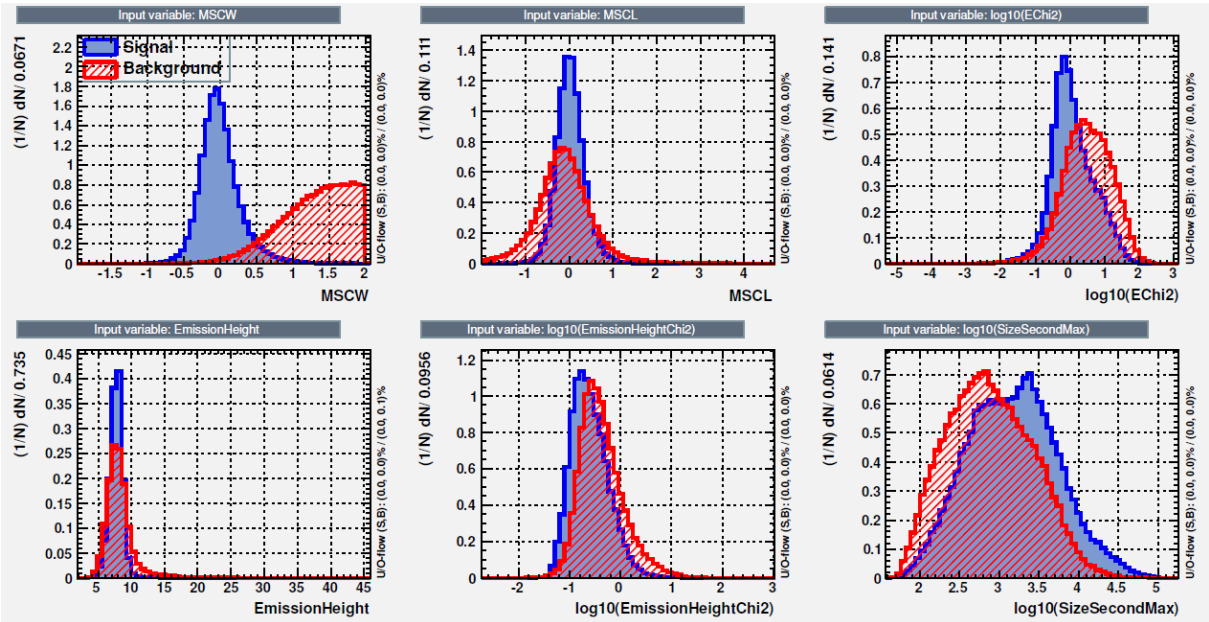

Figure 4.6.: Distribution of cut variables for events with high energies ($E \approx 10\,\mathrm{TeV}$). Signal events (blue) are simulated gamma rays, background events (red) consist of protons only. Figure taken from Maier (2011).

background efficiencies and the significance in dependence of the BDT cut value. For the low energy events, the most important cut parameters are the emission height and the χ^2-value of the energy estimation while for the high energy events the mean-scaled width and the second largest image size are the most effective gamma-hadron discriminants. It should be noted, that this optimization procedure might be limited by proton statistics at very high energies (above several tens of TeV). In these cases, the optimal cut value from the last bin with sufficient statistics is used.

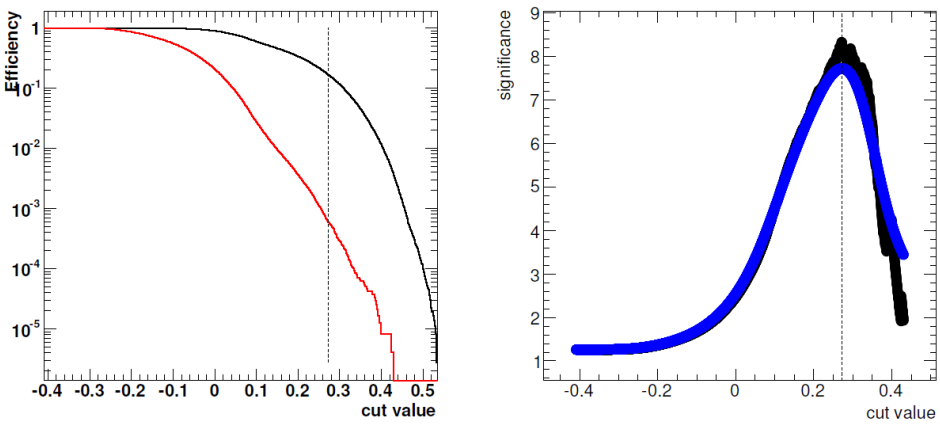

Figure 4.7.: (Left) Example of signal (black) and background (red) efficiencies as a function of the BDT cut value. (Right) Significance as function of the BDT cut value as explained in the text. The blue line shows the smoothed version of the actual values (black points) and is used for the determination of the maximum of the curve (vertical dashed line in both plots). Figures taken from Maier (2011).

In the following, these optimized cuts are used to determine the baseline performance parameters effective area, angular and energy resolution, and sensitivity for Array E. For a comparison of the different candidate arrays and the different analysis chains used within CTA, the reader is referred to Stamatescu et al. (2012) and Bernlöhr et al. (2013).

Effective area

The effective area describes the efficiency of the instrument to detect air showers and is shown in Figure 4.8 for gamma rays. It covers a wide energy range and is smoothly increasing with increasing energy. In the low energy regime, the increase in effective area for Array E compared to the VERITAS effective area arises from the large mirror area of the LSTs, able to detect more Cherenkov light from these low-energy gamma-ray showers. In the core energy regime, the amount of 23 closely spaced MSTs with their large field-of-view results in an effective area

increase of approximately one order of magnitude compared to VERITAS. At higher energies the wide area covered by the SSTs further increases the effective area to more than 10^6 m^2.

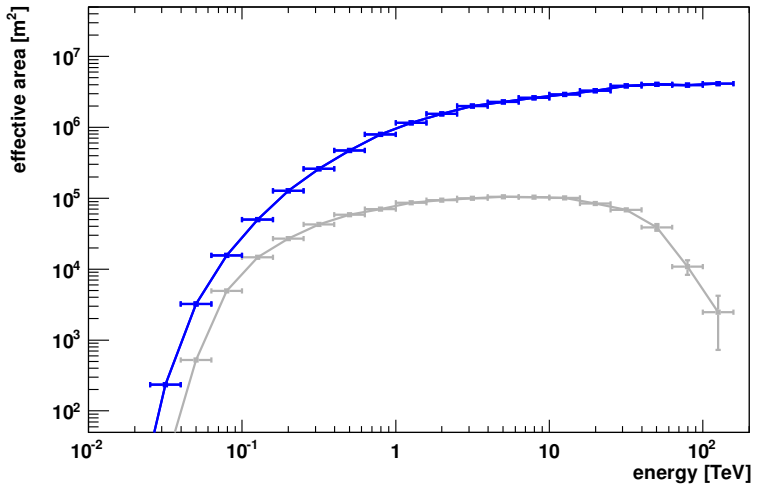

Figure 4.8.: Effective area after cuts for gamma-ray events using Array E (blue curve). The VERITAS upgrade effective area from Figure 3.17 is shown for reference (grey curve).

Angular and energy resolution

The angular resolution of IACTs is typically defined as the angular distance (or radius) from the (simulated) source position within which 68% or 80% of the reconstructed events are contained. The 68% confidence level is the one used for the results presented in this thesis and is shown for Array E in Figure 4.9 (left). In general, the angular resolution improves with increasing energy. For low-energy events, the Cherenkov photon density is relatively low and thus fewer telescope images can be used in the geometrical reconstruction. With increasing energy, more images are recorded by the array and the high telescope multiplicity results in an improved angular resolution; reaching about three arc minutes at 1 TeV. It should be noted that with cuts optimized on angular resolution rather than on significance, the performance goal of arc minute resolution at TeV energies is likely to be reached.

The energy resolution of an array of Cherenkov telescopes is a measure of the uncertainty in how well the system can infer the energy of the primary gamma-ray photon that initiates the air shower. The energy resolution at the 68% confidence level is shown on the right side of Figure 4.9 for Array E. In general, the energy resolution is improving towards higher energies and is below 10% at energies above 1 TeV. For low energetic events, statistical fluctuations in the air shower developments, especially upward fluctuations in the Cherenkov light emission are

more likely to be triggered by the telescopes and thus, limit the energy resolution in this energy regime.

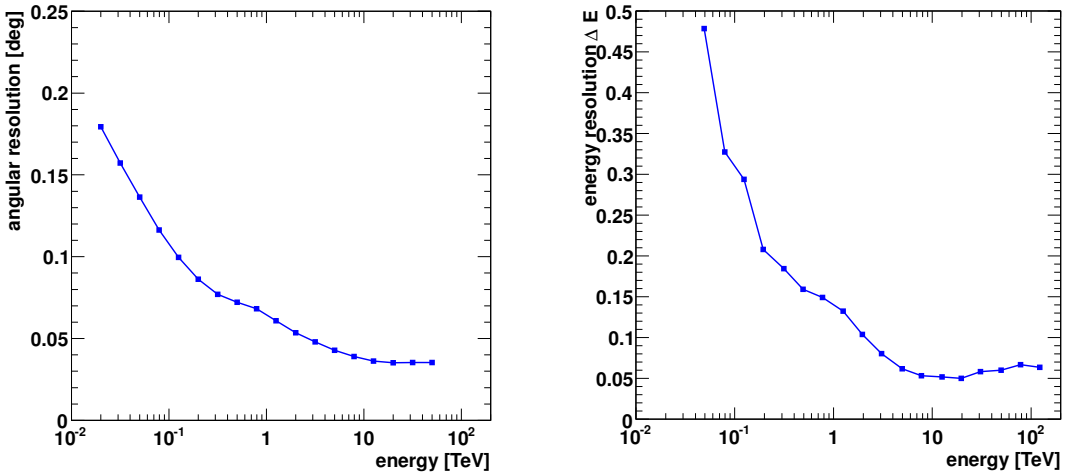

Figure 4.9.: Angular (left) and energy (right) resolution at the 68% confidence level for Array E as a function of energy.

Sensitivity

To evaluate the performance of CTA over the full energy range, the differential sensitivity is determined for 50 hours of observations and an on-to-off source ratio of 1/5. The standard requirements, using five bins per energy decade, are: a significance above 5σ (Eq. 17 in Li & Ma, 1983), at least 10 events per bin and the number of gamma rays is 5% above the background rate (see Eq. 3.12). The errors in the sensitivity curve are derived from the uncertainties in the gamma-ray and cosmic-ray background effective areas. They are dominated by the limited number of simulated proton events. Sensitivity calculations at the lowest and highest energies are in many cases limited by the available number of proton events after gamma-hadron separation cuts.

The resulting differential sensitivity curve, multiplied by E^2, for Array E is shown in Figure 4.10. It covers a large range in energy (four orders of magnitude) and shows a clear improvement compared to the sensitivity of VERITAS. In the low-energy regime ($\leq$ a few hundred GeV), the poor angular/energy resolution results in a limited gamma-hadron separation and thus a high background rate. Therefore, the sensitivity in this energy regime is typically limited by background systematics and shower fluctuations. In the medium-energy range (few hundred GeV to a few TeV), the best differential sensitivity is reached. This is due to the large number of

images available for the reconstruction, which results in a good angular/energy resolution and allows a very good gamma-hadron separation. At higher energies (above several TeV), where the background rates are low due to their steeply falling spectra, the sensitivity is signal limited and the wide area covered by the SSTs results in a sensitive instrument up to energies of about 100 TeV.

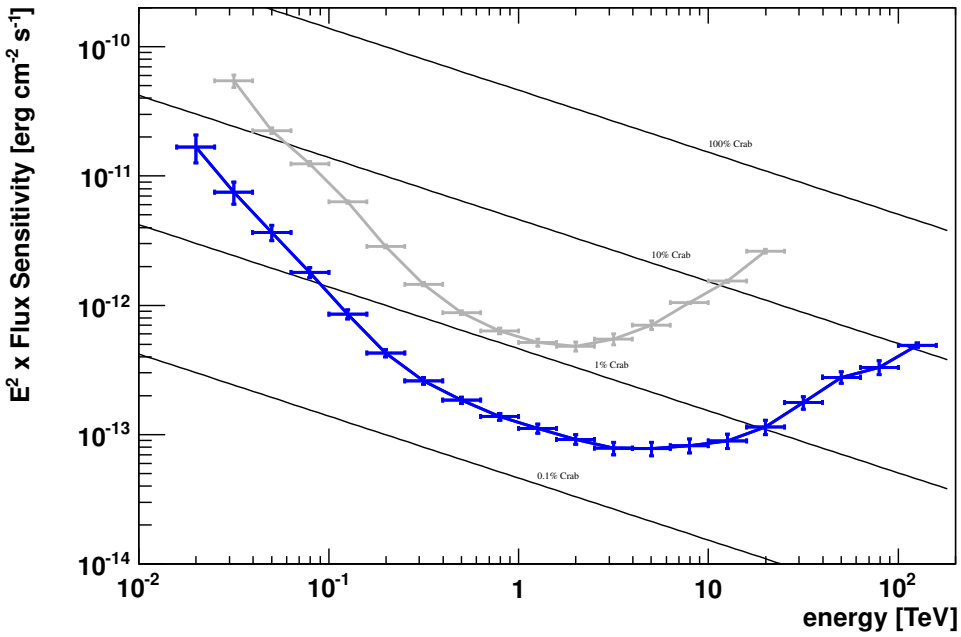

Figure 4.10.: Differential sensitivity curve for Array E (blue curve) for 50 hours observations using the standard requirements given in Eq. 3.12. Simulations are done at 20° zenith angle and background includes cosmic-ray protons and electrons. The grey curve corresponds to the VERITAS upgrade sensitivity for reference.

4.3. Moonlight observations with CTA

Observations with ground-based gamma-ray telescopes are normally carried out during clear, dark and moon-less nights. This leads to about 1000 hours of observing time per year. This time can be increased when observations under partial moonlight are performed, as it is routinely done by MAGIC (Britzger et al., 2009) and VERITAS (Section 3.1.3). To determine if CTA should be operated under moonlight conditions, its performance under this special aspect is estimated. Therefore, a new MC simulation has been set-up and analyzed. The obtained

results are compared with the performance of the candidate arrays under standard (dark-sky) conditions.

4.3.1. Moonlight simulation settings

It has been shown in Section 3.1.3, that the NSB level under moonlight conditions is highly variable and depends on the Moon phase, its elevation and the separation angle between the Moon and the telescope pointing. As it is impractical to simulate all possible background levels due to CPU time and disk-space requirements, only one increased NSB level is considered. The NSB level is chosen to be 4.5 times higher then in the standard simulation. This is comparable with observations where the Moon phase is approximately 50% and would add approximately 30% observation time. With this increased background from NSB photons, the accidental trigger rate is expected to be higher for the same trigger settings. In order to keep the trigger rates at a reasonable level, the pixel (discriminator) thresholds q have to be adapted. Therefore, the accidental trigger rate due to pure NSB is simulated in dependence of the discriminator threshold. Two different camera triggers are tested, requiring three (or four) neighboring pixels above the threshold value q within a certain coincidence time window.

The results of these NSB simulations are presented in Figure 4.11, showing that the accidental trigger rates for all telescope types are much higher under moonlight conditions compared to the standard NSB settings used in the production-1. Additionally, for the 3-pixel coincidence the discriminator threshold at a given NSB trigger rate is higher compared to the 4-pixel coincidence due to the more pronounced afterpulsing effects.

To determine the optimum pixel threshold for both camera trigger conditions under moonlight conditions, the same criteria as for the dark sky NSB settings is applied, i.e. the single telescope trigger rate has to be below 100 Hz. The obtained values for the pixel threshold are summarized in Table 4.3. Comparing these values to the dark-sky simulations shows that the pixel threshold for the same trigger scheme (i.e. 3-fold pixel coincidence) is increased by more then 50% for all telescope types under moonlight conditions. This will naturally lead to an increase of the detection energy threshold for each telescope type.

In order to judge which trigger condition will perform best at lowest energies, the trigger effective areas at the chosen pixel threshold as well as the energy thresholds are determined. The increase in the discriminator threshold reduces the effective area on trigger level compared to the standard thresholds, as shown in Figure 4.12. This effect is most pronounced at low energies. However, there is no clear difference between a 3-fold or 4-fold camera trigger. The calculation of the energy thresholds, defined as the peak in the differential trigger rate for a Crab Nebula-like spectrum, results in the same energy threshold for both applied trigger conditions

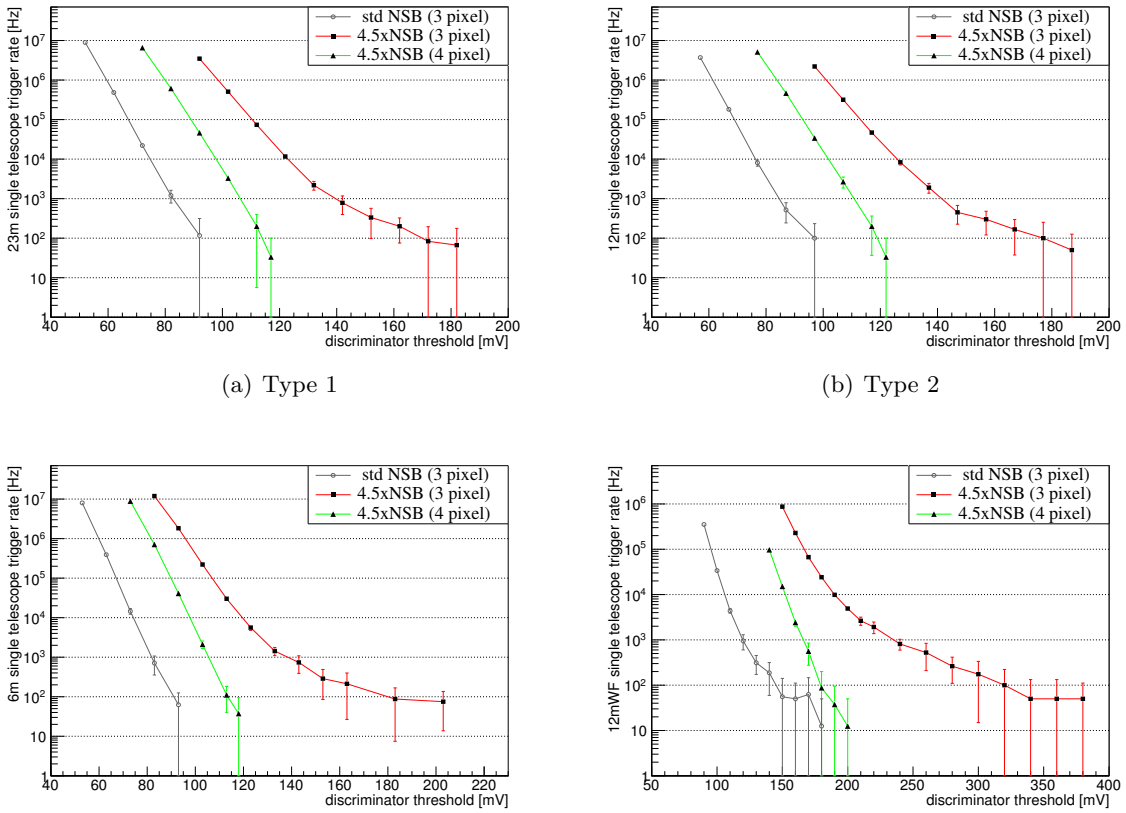

(a) Type 1

(b) Type 2

(c) Type 3

(d) Type 4

Figure 4.11.: Telescope trigger rates due to pure NSB in dependence of the pixel thresholds for the different telescope types for a dark sky patch (gray), moonlight with 3-pixel coincidence (red) and moonlight with 4-pixel coincidence (green).

under increased NSB. The values are given in Table 4.3 and are about twice as high as the energy threshold under dark sky conditions.

To estimate the performance of the full CTA observatory during moonlight a Monte Carlo production has been set up, including shower and slightly modified detector simulation for the 275-telescope layout. As the NSB is added to signal within the detector simulation, no modifications to the shower simulation need to be made, while the modifications to the detector simulations are: (a) increase of the NSB value by a factor of 4.5, (b) change of the camera trigger condition from a 3-fold to 4-fold pixel coincidence[6], and (c) adjustment of the pixel threshold to the values listed in Table 4.3.

[6] A 4-fold pixel coincidence was used, as no difference in performance at trigger level could be seen and the afterpulsing effects are less pronounced in this case.

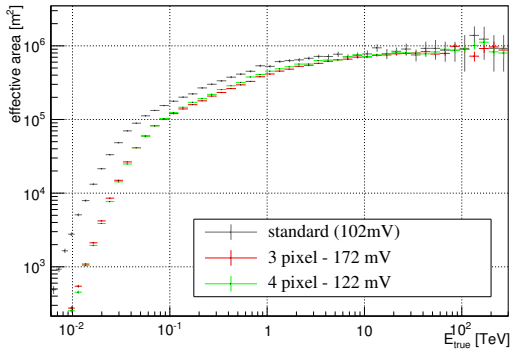

(a) Type 1

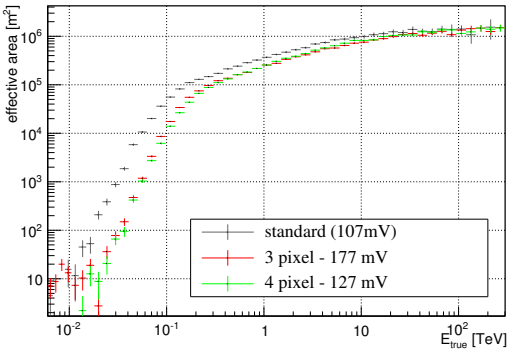

(b) Type 2

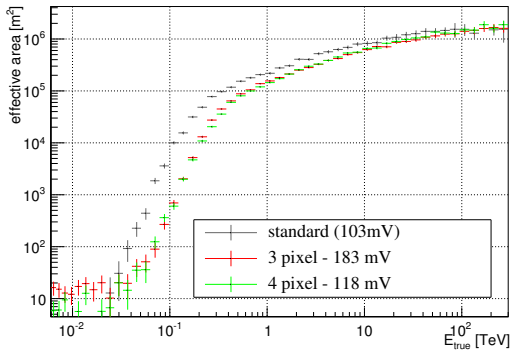

(c) Type 3

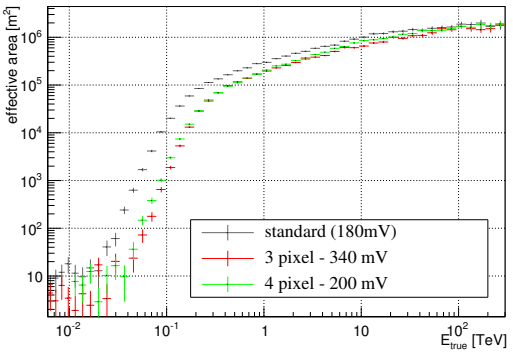

(d) Type 4

Figure 4.12.: Effective areas in dependence of the simulated MC energy E_{true} on trigger level for the different telescope types. Shown are the curves for a dark sky patch (gray), moonlight with 3-pixel coincidence (red) and moonlight with 4-pixel coincidence (green).

Telescope Type	NSB (p.e./ns)		Pixel Thresh. (mV)		Energy Thresh. (GeV)	
	dark sky	moonlight	dark sky	moonlight	dark sky	moonlight
Type 1 (LST)	0.122	0.550	102	172 (122)	17	36 (36)
Type 2 (MST)	0.120	0.540	107	177 (127)	70	137 (137)
Type 3 (SST)	0.085	0.383	72	183 (118)	130	270 (270)
Type 4 (MST-WF)	0.274	1.233	180	340 (200)	110	210 (210)

Table 4.3.: NSB level for dark-sky and moonlight conditions for the different telescope types in production-1. The pixel thresholds for moonlight conditions are using a 3-pixel (4-pixel) next neighbor camera trigger. The energy threshold is defined as the peak in the differential counting rate for a Crab Nebula-like spectrum.

4.3.2. Analysis of moonlight simulations

As already mentioned in Section 2.2.2, the light from the NSB adds noise to the Cherenkov light recorded by the camera and can result in additional uncertainties in the determination of orientation, intensity and shape of the image. To reduce the noise contribution from the shower images, an image cleaning is performed. The image cleaning used here is a two-stage tail-cut cleaning with fixed image and border thresholds. It requires a pixel to have an integrated signal greater then n_i (image pixel) and a neighboring pixel to have at least an integrated signal above n_b (border pixel) with $n_i > n_b$. The tail cuts are adjusted for the higher NSB levels according to

$$\text{tailcut} = n_{i/b} \times \sqrt{\frac{\text{NSB}}{100\,\text{MHz}}} \tag{4.1}$$

and hence vary between the telescope types. Isolated pixels (a single pixel above n_i without bordering pixels) are cleaned away with this routine. This cleaning method is different to the VERITAS analysis where the image and border thresholds are variable (determined by their signal-to-background ratio, see Section 3.2.2).

Since the determination of the optimum image cleaning thresholds is non-trivial two sets of fixed tail-cuts are used which are based on experience rather than on an optimization process. For the first set (hereafter called **10/05**) the cleaning thresholds are $n_i = 10$ and $n_b = 5$ and for the second set (hereafter called **07/04**) they are $n_i = 7$ and $n_b = 4$. The absolute values given in photo-electrons are listed in Table 4.4.

NSB condition	cleaning levels	Type 1 (LST)	Type 2 (MST)	Type 3 (SST)	Type 4 (MST-WF)
dark sky	**10/05**	11.0/5.5	11.0/5.5	9.2/4.6	16.8/8.3
moonlight	**10/05**	23.4/11.7	23.2/11.6	19.6/9.8	35.1/17.5
moonlight	**07/04**	16.4/9.4	16.2/9.3	13.7/7.8	24.6/14.0

Table 4.4.: Absolute image cleaning values (in p.e.) for different night sky background conditions. The values are listed as "image/border".

To illustrate the influence of the different tail cuts for the increased NSB level, Figure 4.13 shows the same event seen in one telescope with the two different cleaning values: (left) the tail cuts used for dark sky conditions, (right) the 07/04 tail cuts adapted for the increased NSB level. It is clearly visible that without scaling the tail cuts according to the NSB the image parameterization is distorted by the noise contribution in the camera, resulting in a poor reconstruction of the image. Using the NSB-adapted 07/04 tail cuts, the image is nicely reconstructed.

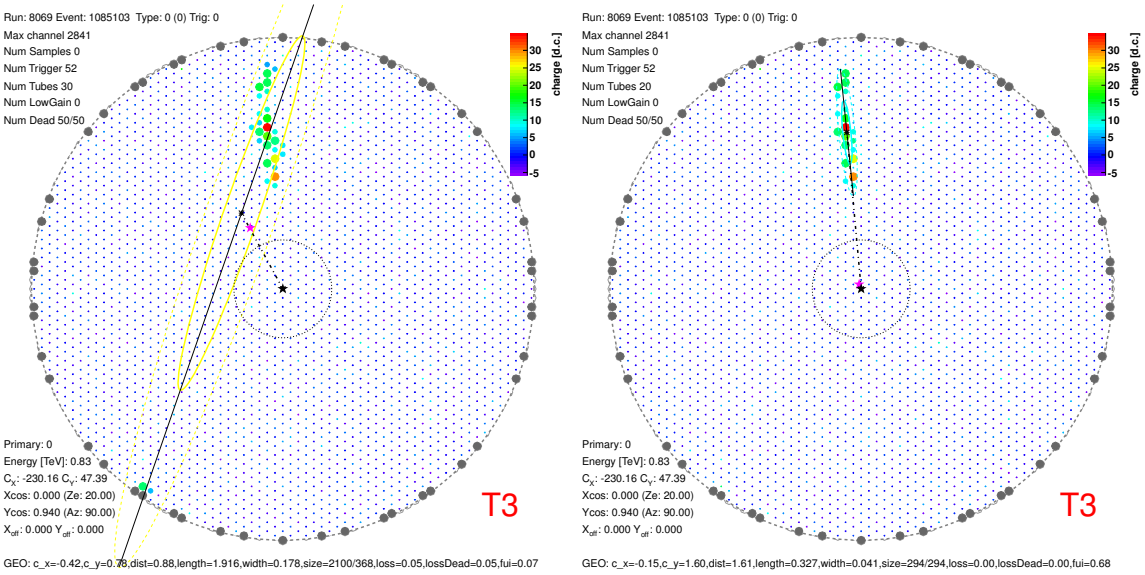

Figure 4.13.: Camera display (LST) for the same event using different image cleaning values for the moonlight simulation. (Left) Tail cuts as used for dark sky conditions (10/05 dark) lead to a wrong parameterization of the image due to noisy pixels. (Right) Tail-cut values are accounted for the increased NSB level (07/04 moon) The absolute values in photo-electrons are listed in Table 4.4. The star indicates the simulated (black) and reconstructed (magenta) arrival direction of the gamma ray in the camera.

The cleaned shower image is then parameterized and the event is reconstructed, applying the same quality cuts as given in Table 4.2. Since the higher NSB level has influence on the distribution of the reconstructed image parameters, lookup tables are filled for each image cleaning set separately. They are then used to estimate the energy and the mean-scaled parameters of each event. For the gamma-hadron separation, BDTs, as previously mentioned, were used.

4.3.3. Performance of CTA under moonlight conditions

To evaluate the performance of CTA under moonlight conditions the instrument response functions and the sensitivity curves are obtained for the different arrays. Three of the possible candidate arrays are used for illustration[7]: Array B, C, and E. Their performance parameters are compared to the performance obtained under dark-sky conditions.

[7] All commonly used candidate arrays have been analyzed by the author, but it became apparent that they can be grouped into three classes in terms of performance. Therefore, only one candidate array for each of these classes is used and presented in more detail.

Effective area & energy threshold

Figure 4.14 shows the gamma-ray effective areas after gamma-hadron separation cuts for the selected arrays for moonlight conditions (using both image cleaning sets) as well as for dark sky conditions. For all candidate arrays the effective area under moonlight conditions is reduced with respect to the dark-sky simulations. This is expected from the studies of the single telescope effective areas at the trigger level (Figure 4.12). The difference between dark-sky and moonlight conditions in effective area is less pronounced at the analysis level than on trigger level. A possible reason for this effect is that the image cleaning thresholds are too strict for the dark-sky conditions and we thus loose showers at low energies in the analysis. Additionally, the loss of effective area occurs in different energy ranges, depending on the selected candidate array. This could be due to the overlapping energy regimes of the different telescope types and the fact that the pre-selection cuts were not optimized (e.g. minimum number of pixels used per image) for each sub-array separately.

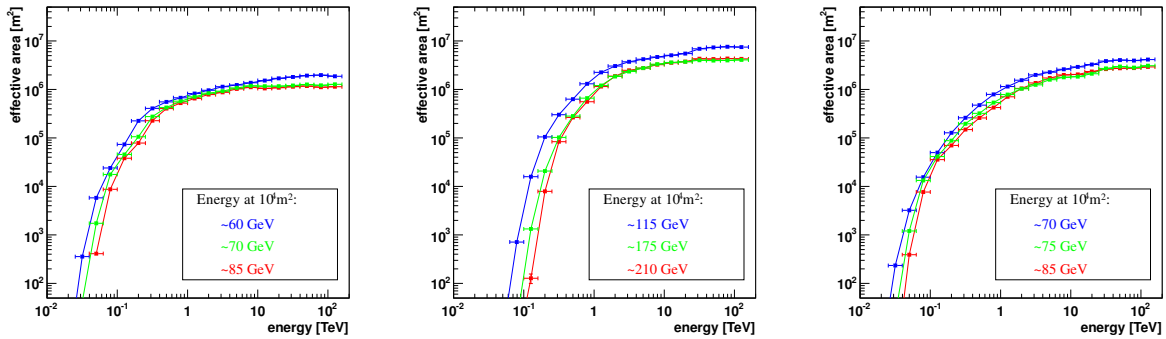

(a) Array B (b) Array C (c) Array E

Figure 4.14.: Gamma-ray effective areas for the different sub-arrays after gamma-hadron cuts for dark sky (blue) and moonlight conditions with the different cleaning levels (red: 10/05, green: 07/04). The energy values for an effective area of 10^4 m^2 are given in the legend and can be interpreted as energy threshold of the given candidate array (see text for details).

Another way to look at the effective area of gamma-ray events is in terms of the energy threshold of the instrument. The energy threshold of a Cherenkov telescope array has previously been defined as the energy at the maximum in the differential counting rate. However, this definition is not very sensitive to the lowest accessible energies in CTA due to the different telescope types used. Therefore, one can compare the energies at a fixed effective area. The values are listed in the plots of Figure 4.14 for an effective area of 10^4m^2. The errors on these

energy values are approximately ± 0.1 in $\log_{10}$(energy[TeV]). This demonstrates several things: firstly, the energy threshold for moonlight conditions increases compared to dark sky conditions. Depending on the image cleaning (and the sub-array) this effect can be quite small and one nearly reaches the energy threshold under dark sky conditions. Secondly, for most of the sub-arrays the energy threshold under moonlight conditions is still below 100 GeV (only exception are those arrays without LSTs which hardly reach the 100 GeV at $10^4 \mathrm{m}^2$ for dark sky conditions).

Angular & energy resolution

The angular resolution for the different candidate arrays (Figure 4.15) shows a very good agreement between dark-sky and moonlight conditions. The same good agreement can be seen in the energy resolution (Figure 4.16) for the different arrays. For Array B the angular resolution at high energies gets worse because it is very compact and most of the high energy showers are located outside the array. This also means that most of the images tend to be close to parallel. By applying a less strict tail-cut cleaning, noisy pixels are added to the image and the reconstruction of the impact parameter and hence the angular and/or energy resolution worsens. However, this effect is already visible in the standard analysis and a method to reconstruct those nearly parallel images better is currently under investigation (e.g., the disp method, Senturk et al., 2011).

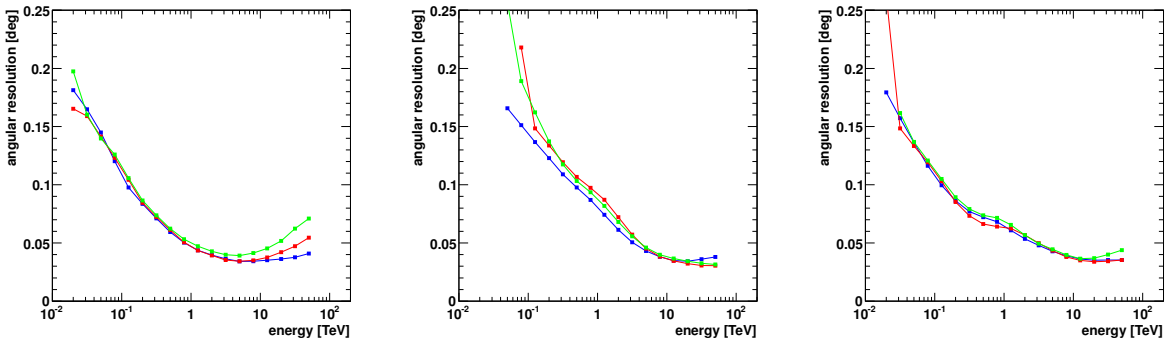

(a) Array B (b) Array C (c) Array E

Figure 4.15.: Angular resolution (68% containment radius) as a function of energy for different sub-arrays for dark sky (blue) and moonlight conditions with the different cleanings (red: 10/05, green: 07/04).

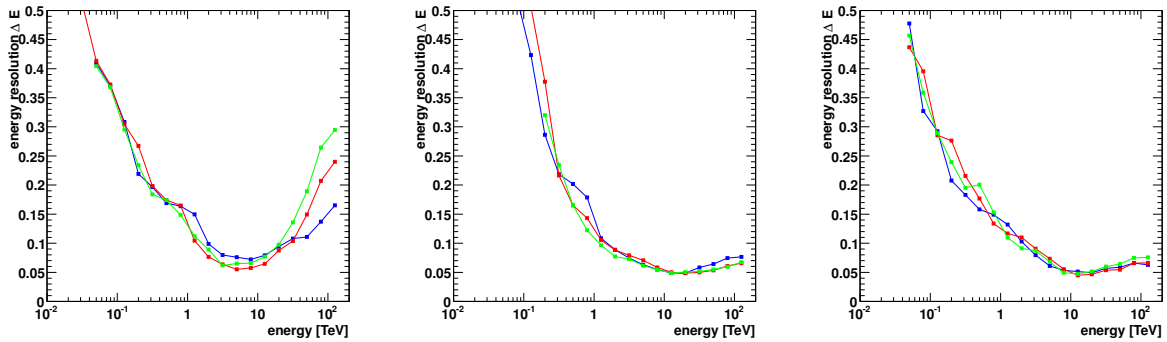

(a) Array B (b) Array C (c) Array E

Figure 4.16.: Energy resolution as a function of energy for different sub-arrays for dark sky (blue) and moonlight conditions with the different cleanings (red: 10/05, green: 07/04).

Sensitivity

In Figure 4.17 the sensitivity curves for the three candidate arrays are shown for moonlight conditions using both image cleaning sets as well as for dark sky conditions. Comparing the sensitivities of the different arrays obtained under dark-sky to those under moonlight conditions shows that the sensitivity under moonlight is slightly worse over the whole energy range, especially at the lowest energies. Additionally, the looser image cleaning applied to the moonlight simulations (07/04) mostly performs better over the whole energy range compared to the 10/05 cleaning applied to the moonlight simulations. Exceptions are those candidate arrays without LSTs where the low energy performance is much worse for the moonlight conditions than under dark sky which may hint to too strict cuts for the MSTs.

4.4. Summary & Outlook of CTA simulations

The analysis of the CTA simulations presented here clearly demonstrates that the main performance goals of CTA can be met. With an array configuration similar to Array E and an image-moment-based analysis, an improvement of the order of one magnitude in energy range and sensitivity is possible to reach. Furthermore, an increase in observation time by up to 30% can be achieved if operations under partial moonlight are performed. The analysis shown here results in a very good agreement in angular and energy resolution between moonlight and dark-sky conditions and the differential sensitivity under moonlight conditions is comparable within a factor of two to the results obtained for dark sky conditions. These results have been confirmed by an independent analysis (Farnier & Lenain, 2011) using this special MC simulation set pro-

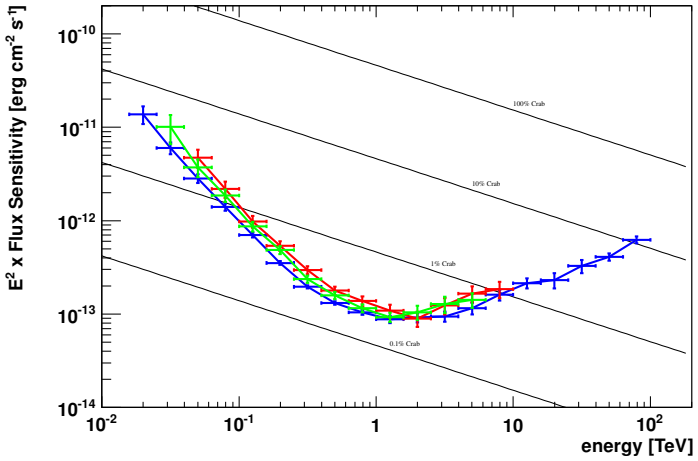

(a) Array B

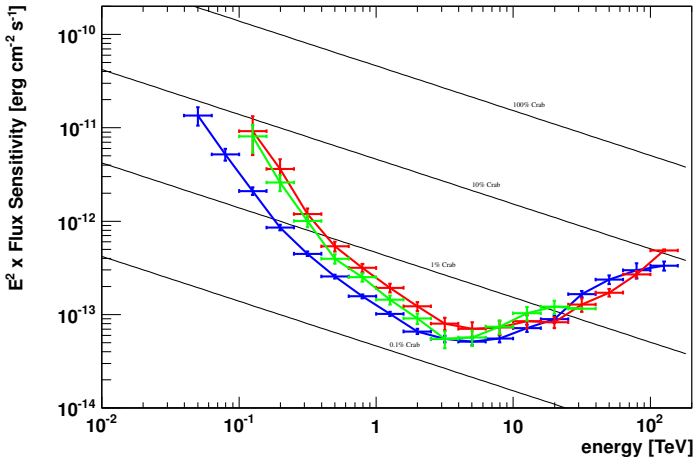

(b) Array C

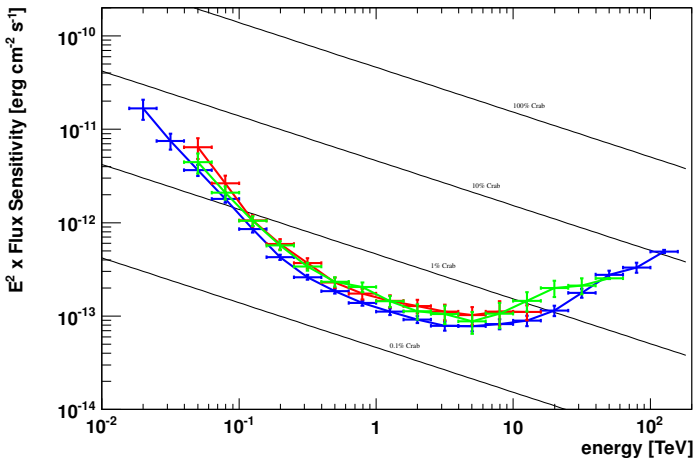

(c) Array E

Figure 4.17.: Sensitivity for different sub-arrays for dark-sky (blue) and moonlight conditions with the different cleanings (red: 10/05, green: 07/04).

vided by the author. It is therefore likely, that moonlight observations will become a regular operation mode in CTA.

The MC simulations used here were only the first iteration in layouts and technical implications, more studies are ongoing. A new array layout, the production-2 configuration, is now under study, where the lessons learnt from the first production are accounted for. Special emphasis is given to a more realistic implementation of site parameters (geomagnetic field, observation level) and the technical developments carried out within the collaboration. Developments of the analysis are as well ongoing which are expected to improve the overall performance of CTA even further.

5. Blazars as Targets for VHE Astronomy

Blazars are a subclass of active galactic nuclei. They represent to date about one third of the population of VHE gamma-ray emitter and are dominated by non-thermal emission. A general overview about AGN, with focus on the observations of blazars, is given in Section 5.1. Long-term observations of the blazar B2 1215+30 with VERITAS are presented in Section 5.2. These VHE measurements are complemented with contemporaneous multi-wavelength observations.

5.1. Active Galactic Nuclei

Active galactic nuclei (AGN) are among the most powerful objects in the Universe. The nucleus in AGN produces more radiation than the entire galaxy. The luminosity from this core region is typically in the range of 10^{45} to 10^{49} erg/s, compared to 10^{44} erg/s for the rest of the galaxy. The emitted radiation is usually highly variable and is dominated by non-thermal emission. AGN are observed across the whole electromagnetic spectrum, from radio to gamma rays.

There are several sub-classes of AGN which were historically discerned, e.g., by their radio emission (radio-loud or radio-quiet) or their optical emission line properties (see, e.g., Antonucci, 1993). Radio-loud objects emit collimated beams or jets of plasma while most of the AGN ($\sim 90\%$) do not show these large scale jets and are classified as radio-quiet (e.g., the so-called Seyfert Galaxies). So far, only radio-loud objects have been detected at very high energies. These radio-loud objects can be further sub-divided based on their radio morphology into compact (blazars) and extended radio sources (Fanaroff-Riley Galaxies; FR I and FR II). Presently, it is believed that the various AGN sub-classes are connected to each other and that the observed characteristics of AGN can be attributed to the geometry of the system; in particular, the orientation of the jets with respect to the observer. In this unified scheme (Blandford & Königl, 1979; Urry & Padovani, 1995), illustrated in Figure 5.1, an AGN consist of the following constituents:

Black hole. A super-massive black hole (SMBH) of 10^6 to 10^{10} solar masses lies in the center of the galaxy. Even though other massive, dense, and non-luminous objects (e.g. a cluster of neutron stars or white dwarfs) could also explain the motion of stars and gas near the

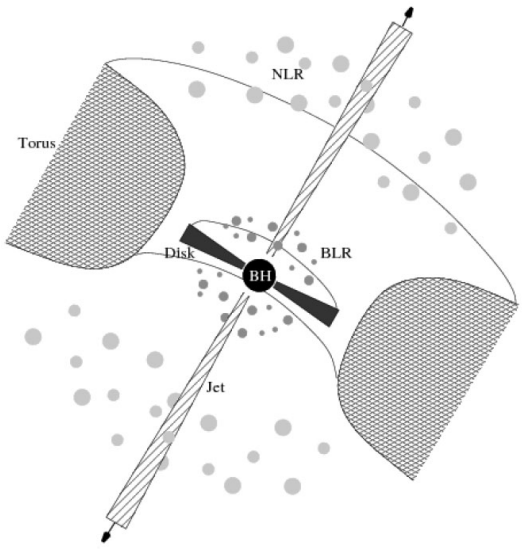

Figure 5.1.: Illustration of the current paradigm of an AGN (not to scale; example lengths in parentheses). The central black hole (for an $M = 10^9 M_\odot$ black hole (BH), the Schwarzschild radius is $R_S \sim 1 \times 10^{-4}$ pc) is surrounded by an accretion disk (~ 0.01 pc). The broad emission lines originate in clouds orbiting above the disk (at ~ 1 pc). A thick dusty torus (inner radius ~ 10 pc) obscures the broad-line region (BLR) when the AGN is seen from the side; narrow lines are produced in clouds much further from the central source (~ 1000 pc) which form the narrow-line region (NLR). Radio jets (extending to about 10^6 pc) emanate from the region near the black hole in the case of radio-loud AGN. The graph is adapted from Middelberg & Bach (2008) with the typical dimensions taken from Rosswog & Brüggen (2007).

center of the active galaxy, the black hole is the most likely candidate as the central engine (see, e.g., Frank et al. (2002) for a discussion).

Accretion disk. The SMBH accretes matter which forms an accretion disk. The gravitational energy is converted into heat and electromagnetic radiation inside the disk which emits radiation mainly at optical/ultraviolet (UV) wavelengths.

Broad-line region. The thermal radiation from the disk ionizes the gas clouds close to the black hole. As these clouds move very fast, their emission lines, seen in the UV/optical, are broadened due to the Doppler effect.

Narrow-line region. In addition to the broad emission lines, slower moving gas clouds further away from the black hole are responsible for narrow-line absorption and emission spectrum of the AGN.

Dusty torus. The optical and UV radiation are obscured along the equatorial line of sight by a torus or wrapped disk of gas and dust well outside the accretion disk. This torus absorbs parts of the radiation emitted from the central region and re-emits the energy at infrared wavelengths.

Jets. Under favorable conditions, some of the material escapes the system as collimated outflows of plasma which appear in directions perpendicular to the accretion disk. Observations in radio (and optical) reveal detailed information about jets (Figure 5.2) and show that these outflows can extend from sub- up to hundreds of kilo-parsecs. Additionally, different jet morphologies exist: from bright and highly collimated jets (as in FR II) to low-luminous and less collimated jets (as in FR I galaxies).
It is not yet known what jets are made of and which of the components (e.g., protons, electrons, Poynting flux) carries the dominant fraction of the jet energy and momentum. In a similar fashion, it is not firmly established how jets form and what collimates them over vast distances (see, e.g., Böttcher et al. (2012) and references therein).

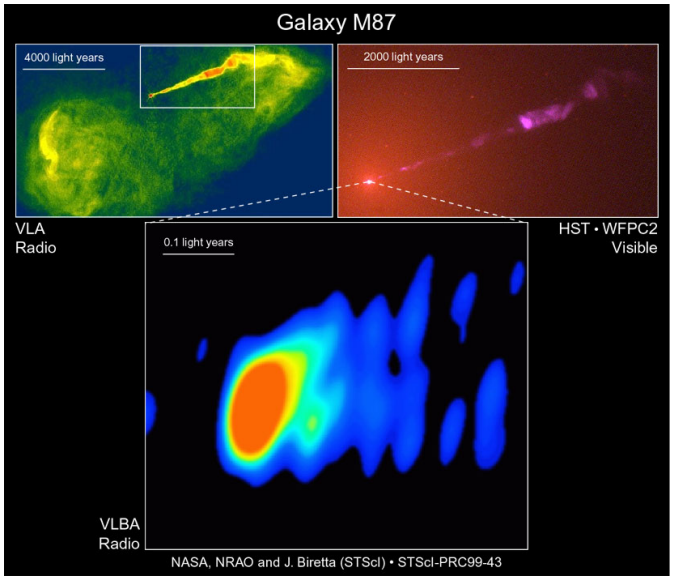

Figure 5.2.: Images of the radio galaxy M 87 at different spatial scales and different wavelengths. The Very Large Array radio image (top left) shows the kpc-scale jet inflating radio lobes. The Hubble Space Telescope optical image (top right) shows the structure of the kpc-scale jet. The Very Large Baseline Array image (bottom center) shows the sub-pc scale jet very close to the black hole. Credits: National Radio Astronomy Observatory/National Science Foundation, NASA and John Biretta (STScI/JHU), National Radio Astronomy Observatory/Associated Universities, Inc.

Radio observations of AGN jets also reveal that individual components propagate away from the core with apparent motions exceeding the speed of light. Such "superluminal" motion can be explained by a near-alignment of the jet with the line of sight of the observer combined with highly-relativistic motion of the radio plasma. Let us assume that the radio knot moves with a relativistic speed $v = \beta_\Gamma c$ along the jet, which is directed at a small angle θ with respect to our line of sight (c being the speed of light). The apparent motion, measured by the observer, is given by

$$\beta_{app} = \frac{\beta_\Gamma \sin\theta}{(1 - \beta_\Gamma \cos\theta)}. \tag{5.1}$$

The velocity distribution of the fastest measured radio jet components peaks at $\beta_{app} \sim 10$, but seems to possess a tail extending up to ~ 50 (Lister et al., 2009; Piner et al., 2012). This indicates that characteristic flow speeds in AGN jets may reach bulk Lorentz factors, $\Gamma = (1 - \beta_\Gamma^2)^{-1/2}$, up to ~ 50, thus being highly relativistic.

5.1.1. Blazars

According to unified schemes, blazars are AGN with a relativistic jet closely aligned to the line of sight of the observer and therefore constitute a relatively rare class of objects. They are sub-divided in two classes: flat spectrum radio quasars (FSRQs) and BL Lacertae objects (BL Lacs). FSRQs are typically distinguished from BL Lac objects by the presence of strong and broad optical emission lines. Other observational features, such as superluminal motion (e.g., Jorstad et al., 2001) and rapid variability (e.g. Valtaoja et al., 1992), suggest that relativistic beaming effects play a key role in blazars. Using the definition of the relativistic Doppler factor

$$D \equiv \frac{1}{\Gamma(1 - \beta_\Gamma \cos\theta)} \tag{5.2}$$

and applying relativistic transformations, it turns out that the observed flux from an astronomical object at frequency ν is related to the emitted flux in the rest frame of the source via

$$\begin{aligned} F_{\rm obs}(\nu_{\rm obs}) &= D^3 F_{\rm em}(\nu_{\rm em}), \\ \nu_{\rm obs} &\propto D\,\nu_{\rm em}, \\ \Delta t_{\rm var}^{\rm obs} &\propto D^{-1}\Delta t_{\rm var}. \end{aligned} \tag{5.3}$$

The observed flux is thus highly amplified as the plasma is moving along the jet towards the observer while the measured variability time scales are shortened. The strong boost of the flux means as well that the observed emission from the jet dominates the overall energy output and

radiation from other parts (e.g., from the disk) are likely to be outshined.

The spectral energy distribution (SED[1]) of blazars spans about 20 orders of magnitude in energy as shown in Figure 5.3. A typical blazar SED consists of two distinct, broad components. The low-energy component ranges from radio to UV/X-rays and can be covered by several (hundreds) different observatories. The second, high-energy component peaks between X-rays and gamma rays and observations in this energy regime can be performed with space-borne detectors like the *Fermi*-LAT and ground-based IACTs.

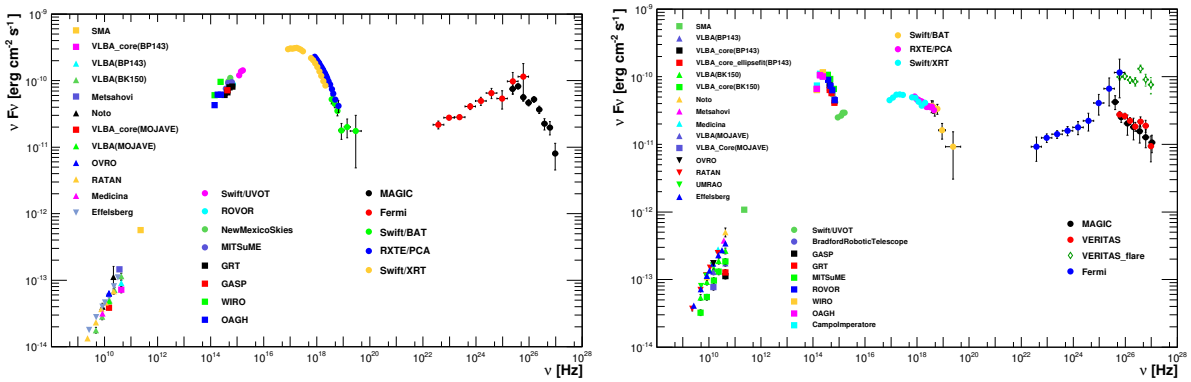

Figure 5.3.: Spectral energy distribution of two blazars during multi-wavelength campaigns with the participating instruments indicated in the figure. Both objects show the two-bump structure typical for blazars. (Left) Mrk 421 in 2009 (Abdo et al., 2011). (Right) Mrk 501 in 2009 (Abdo et al., 2011). Mrk 501 additionally shows a third component at about 10^{14} Hz which is the contribution of the host galaxy.

The non-thermal, continuum spectrum of blazars is commonly attributed to the radiation of particles that are accelerated to highly relativistic energies within the jets. It is thought that this double-bumped structure is produced by synchrotron and inverse Compton emission of relativistic electrons, which is supported by the high polarization observed at radio and optical frequencies (e.g., Wills et al., 1992). However, alternative models to explain this structure exist and an overview of the emission processes in blazars is given in Section 6.1.

5.1.2. VHE observations of blazars

Most of the detected extragalactic VHE gamma-ray sources belong to the blazar class which currently (May 2013) counts 52 objects (Wakely & Horan, 2013). The majority of them ($> 75\%$) are high-synchrotron-peaked BL Lacs with their low-energy component peaking at $\nu_{peak} >$

[1] A blazar SED is usually shown in a νF_ν representation, where the photon flux F_ν times the frequency ν is given as a function of $\log \nu$. Such a plot directly shows which part of the spectrum carries most of the energy as the area below the curve is proportional to the energy emitted by the photons in a certain $\log \nu$ interval.

10^{15} Hz, but also blazars with lower synchrotron-peak frequencies have been detected, including three FSRQs (3C 279, PKS 1510-089, and 4C +21.35).

At present, blazars up to redshift $z > 0.5$ (i.e., PKS 1424+240 at $z \geq 0.6035$ and 3C 279 at $z = 0.536$) have been detected in VHE gamma rays. The measurement of VHE emission from such distant sources has been a surprising result, as the high-energy photons emitted by the sources are absorbed by the interaction with low-energy photons from the extragalactic background light (EBL; e.g., Dole et al., 2006). When traveling cosmological distances, the attenuation of VHE photons by gamma-gamma interaction producing an electron-positron pair can alter the observed spectra substantially, resulting in a spectral steepening at very high energies. This absorption feature in the gamma-ray spectrum can also be used to measure the EBL flux density (see, e.g., Ackermann et al., 2012; Abramowski et al., 2013) which is, for direct detection methods, limited by strong foreground emission in the UV, optical and infrared wavelenghts.

The VHE emission of blazars shows clear variability on different time scales spanning from longer than months down to a few minutes (Aharonian et al., 2007; Aleksić et al., 2011; Arlen et al., 2013). The observed VHE fluxes are typically in the range of a few percent of the Crab Nebula flux for the average states. The sensitivity of the current generation of IACTs limits the detection of much lower flux states within reasonable observation times. Fluxes in states of high activity have reached up to ~ 10 times the Crab Nebula flux in the VHE regime, as seen in Mrk 421 in 2013 (Cortina et al., 2013) and PKS 2155-304 in 2006 (Aharonian et al., 2007). With increasing activity in the VHE regime, a spectral hardening has been observed in a few blazars (e.g. Mrk 421, Acciari et al., 2011a; Mrk 501, Acciari et al., 2011b; PKS 2155-304, Abramowski et al., 2010). While such a behavior can be explained with an increase of the Doppler boost, the softening of the spectrum with increasing flux observed during the quiescent state of PKS 2155-304 (Abramowski et al., 2010), is quite puzzling and gave for the first time a hint of intrinsic differences between the low and the high state in these objects. The fast VHE variability (sometimes measured during high flux states) can be used to constrain the size (and location) of the emission region. These rapid flux variations can also be used to derive constraints on an energy-dependent violation of Lorentz invariance, as predicted in various models of quantum gravity (e.g., Albert et al., 2008).

Observations at other wavelengths, simultaneous with the VHE observations, reveal the complexity of the phenomena at play in these objects. In some blazars a clear evidence for a correlation between VHE gamma-ray and X-ray emission, especially during increased flux states, has been observed (e.g. Mrk 421, Fossati et al., 2008). This lead to the assumption that the non-thermal continuum emission of blazars originates from the same electron population accelerated to TeV energies within the jet. However, the connection is only weak for other blazars (e.g.

Mrk 501, Gliozzi et al., 2006) or even non-existing, as seen during a so-called "orphan" flare of 1ES 1959-650 in 2002, where the TeV gamma-ray flux increased by a factor of ten without a noticeable flux increase in X-rays (Krawczynski et al., 2004).

Recently, some new VHE gamma-ray sources have been detected following triggers indicating a high state of these sources in the optical regime (Reinthal et al., 2012). Even though this points toward a possible correlation between TeV and optical emission, this study is still inconclusive.

5.2. An example of VHE blazar observations: B2 1215+30

B2 1215+30 is one of the first BL Lac-type objects to be identified (Browne, 1971) and was one member of the small set of objects used to define the class. It was first detected in the Bologna Northern Cross telescope survey conducted at 408 MHz (Colla et al., 1970) and is also referred to as ON 325 or 1ES 1215+303. The distance to this blazar is uncertain and two different redshift values can be found in the literature: z = 0.130 (Akiyama et al., 2003; NED[2]) and z = 0.237 (Lanzetta et al., 1993; Simbad[3]). While both redshift values have been obtained based on spectroscopic measurements, none of the claimed spectral features could be confirmed with high-resolution measurements: neither with the FAST instrument on the FLWO 60" telescope in 2011 (E. Falco, priv. comm.) nor with a high signal-to-noise spectrum obtained with the Lick Observatory Kast double spectrograph on the Shane 3-m telescope in 2013 (M. Fumagalli, priv. comm.).

In the following the results of VERITAS observations taken in the direction of B2 1215+30 between December 2008 and March 2012 are presented. This blazar is in the same field of view as the bright VHE blazar 1ES 1218+304[4] which is regularly observed by VERITAS (Benbow et al., 2011). The analysis of this VERITAS long-term data set has been carried out by the author. These data are complemented with high-energy gamma-ray observations taken by *Fermi*-LAT. Results from multi-wavelength observations[5] obtained in 2011, quasi-simultaneous with VERITAS, are used to construct the SED of B2 1215+30.

5.2.1. Very-high-energy observations with VERITAS

The VERITAS observations reported here include observations of B2 1215+30 and 1ES 1218+304; two sources seperated by 0.76° and thus within the same field of view. Most of the observations had 1ES 1218+304 as the principal target, resulting in different pointing offsets from the

[2] NASA/IPAC Extragalactic Database: `http://ned.ipac.caltech.edu/`
[3] SIMBAD Astronomical Database: `http://simbad.u-strasbg.fr/simbad/`
[4] B2 1215+30 and 1ES 1218+304 are 0.76° away from each other.
[5] The analysis of the MWL data sets was carried out by members of the VERITAS Collaboration, presented in Prokoph et al. (2012) and Aliu et al. (2013).

position of B2 1215+30 (from 0.3° to 1.3°) as all data were taken in "wobble mode", with a pointing offset of 0.5° from the camera center. Combining the observations on both sources, VERITAS observed B2 1215+30 for more than 92 hours between December 2008 and March 2012. The run quality selected data (see Appendix B.2 for the complete runlist) are divided into three data sets, corresponding to yearly observation epochs. The first one spans 34 hours from December 2008 to May 2009 at a mean zenith angle of 20 degrees, the second data set was recorded between January and June 2011 (42 hours) at a mean zenith angle of 15 degrees, and the third data set was taken from January to March 2012 (16 hours) with a mean zenith angle of 13 degrees. Due to the different pointing positions and the non-uniform radial acceptance of the camera, the average sensitivity for the VERITAS exposure on B2 1215+30 is reduced. Correcting for this effect, the total effective exposures on B2 1215+30 (in 0.5° wobble offset), are 29, 38, and 14 hours for the different observation epochs, respectively.

The data analysis is performed with `eventdisplay` as explained in Section 3.2 using the cuts given in Table 3.3. The remaining background is estimated using a ring background model with $\theta^2 \leq 0.008\,\mathrm{deg}^2$ and a ring, placed around the ON region, with inner and outer radii of 0.46° and 0.54°, respectively. Regions around bright stars (V magnitude brighter than 7) as well as the region around the position of 1ES 1218+304 were excluded from the background estimation.

The analysis of the total data set over the time period from December 2008 to March 2012 yields 261 excess events and a detection significance of 9.0σ according to Eq. 17 in Li & Ma (1983). The results of the three observing periods are presented in Table 5.1 and show a clear detection with a significance of 10.4σ in 2011, while in 2008/2009 and in 2012 the source is not detected with a significance greater than 3.4σ.

Data set	Exposure [hours]	Zenith [deg]	N_{ON}	N_{OFF}	α	Significance [σ]
2008/2009	34 (29)	20	304	2288	0.1243	1.1
2011	42 (38)	15	472	2325	0.1161	10.4
2012	16 (14)	13	136	828	0.1179	3.4
TOTAL	92 (81)	16	912	5441	0.1198	9.0

Table 5.1.: VERITAS results of B2 1215+30 for the three different observing epochs. The exposure time is given in hours, while the value in brackets gives the effective time on B2 1215+30 (in 0.5° wobble offset equivalent). N_{ON} and N_{OFF} are the number of events in the ON and OFF region, while α is the acceptance corrected area ratio of both regions and the resulting significance of the detection of B2 1215+30 is calculated according to Eq. 3.6.

Before presenting the results of these two latter periods, I concentrate on the 2011 data set where the significant detection allows a spectral analysis. Figure 5.4 (left) shows the significance sky map for the 2011 data set. The derived differential photon spectrum of the 2011 data set is shown in Figure 5.4 (right). It can be fitted by a power law ($\chi^2/\mathrm{ndf} = 1.25/2$):

$$\frac{dN}{dE} = (2.3 \pm 0.5_{\mathrm{stat}} \pm 0.9_{\mathrm{syst}}) \left(\frac{E}{300\,\mathrm{GeV}}\right)^{-(3.6\pm0.4_{\mathrm{stat}}\pm0.3_{\mathrm{syst}})} . \tag{5.4}$$

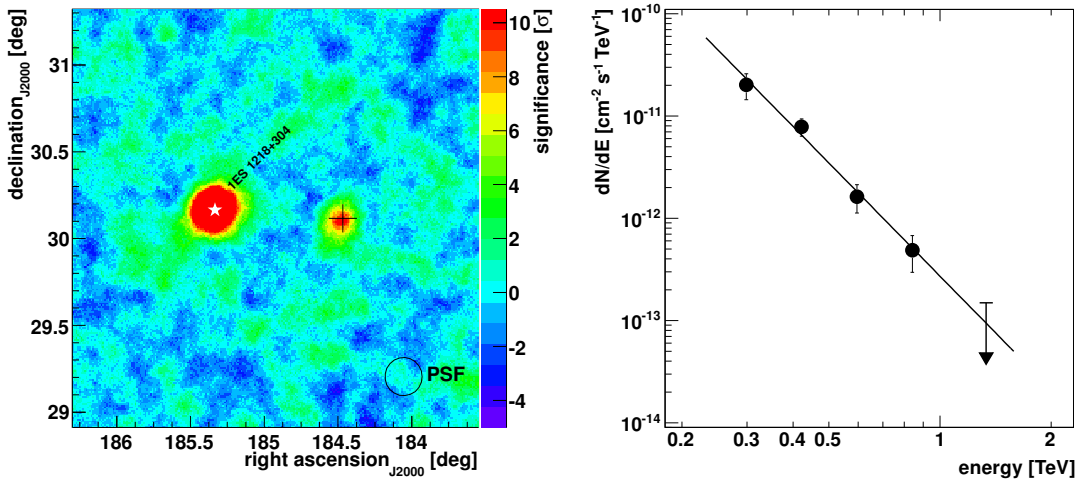

Figure 5.4.: (Left) VERITAS significance sky map of B2 1215+30 in 2011. The black cross shows the position of B2 1215+30 and the white star indicates the position of 1ES 1218+304. Both sources are point-like, but appear to have a different size due to the saturation of the color scale. (Right) Differential photon spectrum of B2 1215+30 obtained with VERITAS in 2011. The spectral points are fitted with a power-law. The error bars denote 1σ uncertainties, and an 95% upper limit is drawn for a spectral point with less then 2σ significance.

The flux above 200 GeV is $(8.0\pm0.9_{\mathrm{stat}}\pm3.2_{\mathrm{syst}})\times10^{-12}\,\mathrm{cm}^{-2}\mathrm{s}^{-1}$. This corresponds to 3.4% of the Crab Nebula flux (Hillas et al., 1998) above the same energy threshold. A monthly binned[6] light curve above 200 GeV is produced and shown in Figure 5.5. A constant fit to these flux points shows no evidence for deviation from a steady flux ($\chi^2/ndf = 4.7/5$). No significant flux variations within any monthly bin were detected either.

The analysis of the data available outside the 2011 season revealed lower gamma-ray fluxes, as shown in Figure 5.6. The 2008/2009 data set analysis resulted in a gamma-ray excess of 1.1σ

[6] A monthly bin corresponds to a period of 29.5 days (= duration of the lunar cycle), starting on the night of the full Moon.

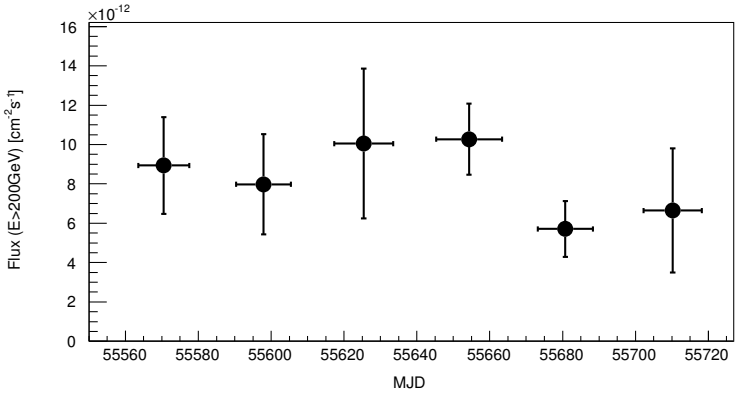

Figure 5.5.: Monthly binned VERITAS light curve above 200 GeV as measured in 2011. Vertical error bars show 1σ statistical uncertainties on the flux, horizontal error bars indicate the width of the corresponding observing interval within the monthly bins. A fit to a constant gives $\chi^2/ndf = 4.7/5$, showing no evidence for variability on monthly time scales. The light curves for the other VERITAS seasons are given in Appendix B.3.

significance at the source location. Using the method of Helene (1983), this excess corresponds to a 99% upper limit above 200 GeV of $4.5 \times 10^{-12}\,\mathrm{cm}^{-2}\mathrm{s}^{-1}$, assuming the same spectral index as derived in 2011, and is <2% of the Crab Nebula flux above the same energy threshold. In 2012, the source is observed with a significance of 3.4σ. Given that it is an established VHE emitter a flux is derived: $F(E > 200\mathrm{GeV}) = (2.9 \pm 1.1_{\mathrm{stat}} \pm 1.1_{\mathrm{syst}}) \times 10^{-12}\,\mathrm{cm}^{-2}\mathrm{s}^{-1}$, corresponding to about 1.2% of the Crab Nebula flux above the same energy threshold. The hypothesis of a constant flux between the three VERITAS seasons is excluded at the level of 4.3σ ($\chi^2/ndf = 22.4/3$). This shows that the source was significantly fainter in 2008/2009 and 2012 compared to the relatively bright flux state in 2011.

This bright flux state and hints for long-term variability of B2 1215+30 were also reported by MAGIC, who discovered this BL Lac object in early January 2011 during observations triggered by an optical high state (Mariotti et al., 2011). In 2011, MAGIC observed B2 1215+30 for 21 hours between January and February and derived an integral flux above 200 GeV of $(7.7 \pm 0.9_{\mathrm{stat}}) \times 10^{-12}\,\mathrm{cm}^{-2}\,\mathrm{s}^{-1}$ with a photon spectral index of $\Gamma = 2.96 \pm 0.14_{\mathrm{stat}}$ (Aleksić et al., 2012b); consistent with the results obtained here. Observations between January and February 2010 by MAGIC revealed a 3.5σ excess at the source location, which can be translated into an integral flux of $(3.4 \pm 1.0_{\mathrm{stat}}) \times 10^{-12}\,\mathrm{cm}^{-2}\,\mathrm{s}^{-1}$. Combining the results from VERITAS and MAGIC shows long-term variability of B2 1215+30, as presented in Figure 5.6. No short-term variability has been detected by any of the two instruments between December 2008 and March 2012.

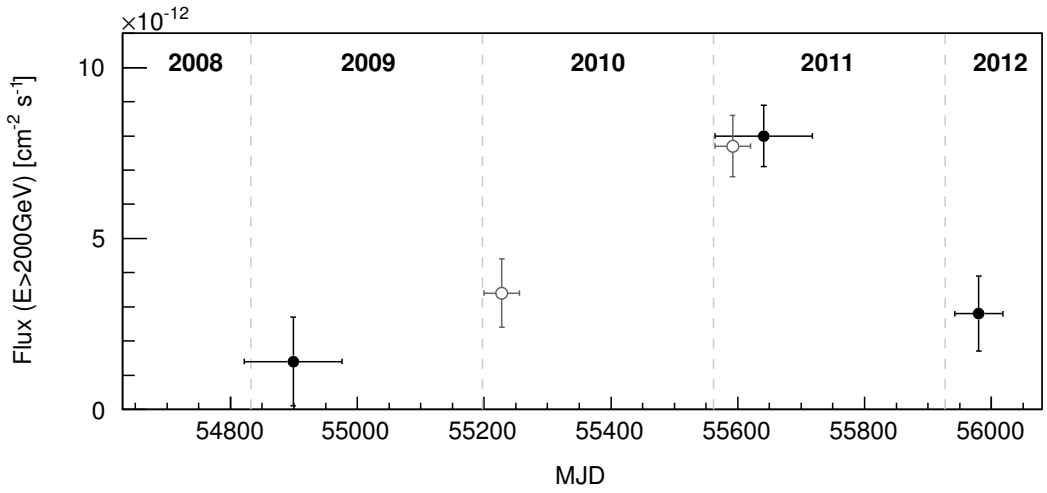

Figure 5.6.: Long-term observations of B2 1215+30 in the VHE regime between December 2008 and March 2012. Flux points are shown for VERITAS (black points) and MAGIC (gray open points). Vertical error bars show 1σ statistical uncertainties, horizontal error bars indicate the width of the corresponding observing interval. It shows a bright flux state in 2011 compared to the fainter flux states during the other seasons.

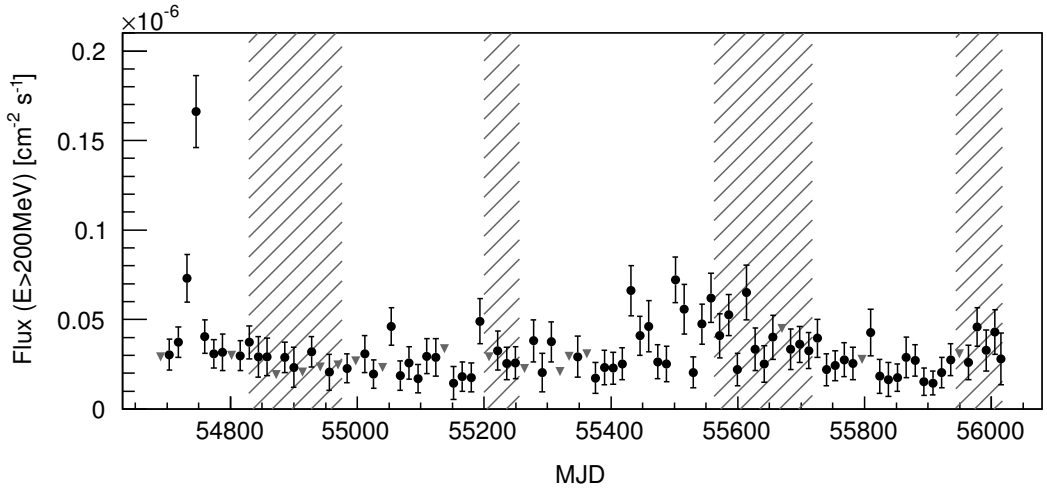

Figure 5.7.: Bi-weekly binned light curve of B2 1215+30 as obtained by *Fermi*-LAT using the first 48 months of the *Fermi* mission. Flux points are shown with 1σ error bars and an 95% upper limit is calculated for bins with a TS-value less than 4. The gray shaded areas indicate the time periods when quasi-simultaneous observations in the VHE regime were obtained by VERITAS and/or MAGIC.

5.2.2. High-energy observations with *Fermi*-LAT

The Large Area Telescope (LAT) on board the *Fermi* satellite is a pair-conversion gamma-ray telescope sensitive to photon energies from 20 MeV to a few hundred GeV (Atwood et al., 2009). It is continuously observing the high-energy gamma-ray sky, and thus also B2 1215+30, since June 2008. B2 1215+30 is listed in the *Fermi* bright source list (Abdo et al., 2009a), and appears in all later *Fermi* catalogs (e.g. Ackermann et al., 2011). In the following, all data from the first 48 months of operation are used.

A binned likelihood analysis was performed using the LAT ScienceTools (version v9r23p1) and P7SOURCE_V6 instrument response functions. "Diffuse" class events with $0.2 < E/\mathrm{GeV} < 100$ in a square region of interest (ROI) of $20^\circ \times 20^\circ$ around B2 1215+30 were selected. As the bright FSRQ 4C +21.35 is 8.87° away from B2 1215+30 it would fall right at the edge of the ROI. To avoid truncation of the source contribution in the analysis, the center of the ROI was shifted by 4° towards 4C +21.35 (to fully include it in the ROI). Further quality selection was performed by rejecting events with a zenith angle $> 100^\circ$ and a rocking angle $> 52^\circ$ in order to avoid contamination from albedo photons from the Earth's limb.

A background model was constructed including nearby gamma-ray sources and diffuse emission. All known gamma-ray sources from the second *Fermi* catalogue (2FGL; Nolan et al., 2012) within the ROI were included in the model. As in the 2FGL catalogue, a log-parabola function was used for sources with significant spectral curvature. Otherwise, spectra were described as power laws. The spectral parameters of the sources inside the ROI were left free during the fitting procedure. Sources outside the ROI, but within 5° of the ROI edges, were also included to account for possible photon contamination due to the large LAT point spread function, but their spectral parameters were fixed to the 2FGL catalog values. The galactic and extragalactic diffuse gamma-ray emission together with the residual instrumental background were modeled using the publicly-available files[7].

A 14-day binned light curve above 200 MeV was produced using the first 48 months of the *Fermi* mission which is shown in Figure 5.7. As already reported in Nolan et al. (2012), B2 1215+30 showed variability within this period with a very bright flux state at the beginning of the mission. A fit to a constant taking all flux points into account yielded a χ^2/ndf of 224.8/95, thus excluding a constant flux with a significance of 7.1σ. In the following, I will concentrate on the time periods contemporaneous with the VHE observations, starting with the bright VHE flux state in 2011.

During the epoch quasi-simultaneous with the 2011 VERITAS observations (MJD 55560 –

[7] The files used were gal_2yearp7v6_v0.fits for the Galactic diffuse and iso_p7v6source.txt for the isotropic diffuse component as available at `http://fermi.gsfc.nasa.gov/ssc/data/access/lat/BackgroundModels.html`.

55720), the flux above 200 MeV is compatible with being constant ($\chi^2/ndf = 11.1/10$) and a spectrum was derived using this subset of observations only. During that 160-day period, B2 1215+30 is detected with a test statistic value of $TS = 363$, corresponding to a significance of about 19 σ. Potential contamination from the nearby source 1ES 1218+304 (at 0.76° distance) was checked by producing a residual TS map; no features or asymmetries in the TS distribution of B2 1215+30 were seen. The spectrum, shown in Figure 5.8, is compatible with a power law with a photon index $\Gamma = 1.97 \pm 0.08$. This is consistent with the photon index given in the 2FGL catalog of $\Gamma_{\mathrm{2FGL}} = 2.02 \pm 0.04$. The integral flux above 200 MeV during this period is $(3.45 \pm 0.34) \times 10^{-8}\,\mathrm{cm}^{-2}\,\mathrm{s}^{-1}$.

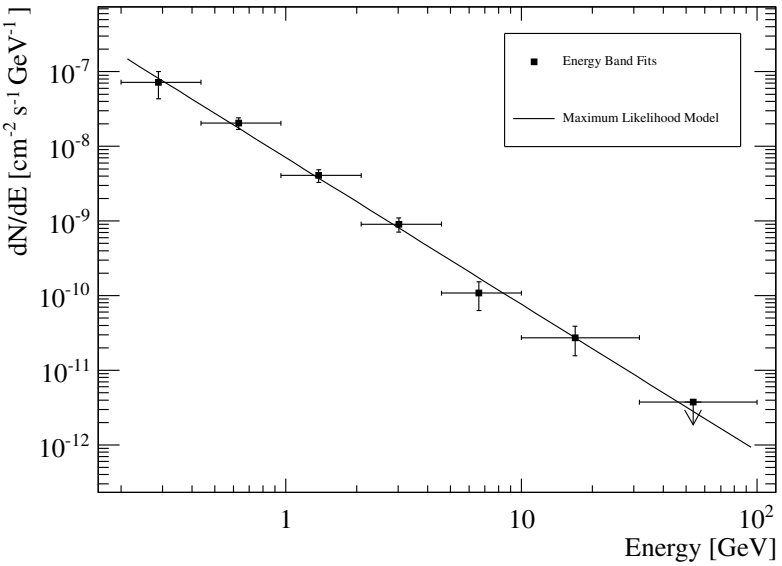

Figure 5.8.: *Fermi*-LAT spectrum quasi-simultaneous with the 2011 VERITAS observations. Courtesy of Manel Errando.

Given the long-term variability seen in the VHE regime, an integral flux above 200 MeV quasi-simultaneous with the VERITAS and MAGIC observations was derived. The values are listed in Table 5.2 together with the VHE observing periods. The hypothesis of a constant gamma-ray flux above 200 MeV contemporaneous with the different VHE observing periods could be rejected at the 3σ-level. No significant short-term flux variations within those time periods (covering several months) have been detected due to the uncertainties on the flux estimation.

5.2.3. A multi-wavelength picture of B2 1215+30 in 2011

In 2011, contemporaneous with the bright VHE flux state, MWL observations were obtained at optical (Super-LOTIS, MDM, *Swift*-UVOT) and X-ray (*Swift*-XRT) frequencies in addition

Data set (MJD)	$F(E > 200\,\mathrm{MeV})$ $[10^{-8}\mathrm{cm}^{-2}\mathrm{s}^{-1}]$	χ^2/ndf	$F(E > 200\,\mathrm{GeV})$ $[10^{-12}\mathrm{cm}^{-2}\mathrm{s}^{-1}]$
2008/2009 (54822 – 54976)	1.8 ± 0.3	18.9/10	1.4 ± 1.3
2010/2011 (55564 – 55718)	3.5 ± 0.3	11.1/10	8.0 ± 0.9
2011/2012 (55942 – 56018)	3.0 ± 0.4	6.6/5	2.8 ± 1.1
2009/2010 (55200 – 55256)	2.3 ± 0.5	2.2/3	3.4 ± 1.0
2010/2011 (55564 – 55620)	4.0 ± 0.6	7.9/3	7.7 ± 0.9

Table 5.2.: *Fermi*-LAT results contemporaneous with the VERITAS (upper part) and MAGIC (lower part) observations at very high energies. The columns are the following: Data set gives the observing season with its start and end date in MJD; $F(E > 200\,\mathrm{MeV})$ is the integrated *Fermi*-LAT; χ^2/ndf lists the resulting fit values assuming constant *Fermi*-LAT fluxes; and $F(E > 200\,\mathrm{GeV})$ is the integrated VHE flux within the listed time period.

to the high-energy gamma-ray observations by *Fermi*-LAT detailed above. They are used to construct the SED of B2 1215+30 and will later be used to model the emission of this BL Lac object.

X-ray observations with *Swift*-XRT

The X-ray telescope (XRT) on board of the *Swift* satellite is designed to measure X-rays in the $0.2 - 10$ keV energy range (Burrows et al., 2005). Target of opportunity observations were obtained in January 2011 (MJD $55565 - 55573$), following the detection of VHE emission from B2 1215+30, as well as in April/May 2011 (MJD $555673 - 55686$). All data presented here were taken in photon counting mode with negligible pile-up effects.

The data reduction and calibration were done using HEASoft, XSPEC version 12.6.0 and the swxpc0to12s6_20070901v011.rmf response function. The data were grouped, requiring a minimum of 20 counts/bin, and then fitted with an absorbed power law model. The galactic column density of $N_\mathrm{H} = 1.74 \times 10^{20}\mathrm{cm}^{-2}$ was used, taken from the LAB neutral hydrogen survey (Kalberla et al., 2005). When it was left free during the fit, the column density value was consistent with what was found by the LAB survey.

The spectral analysis of data showed the blazar in different states, as shown in Figure 5.9. The observations performed in January indicate a harder and brighter flux state, allowing the data to be fitted with an absorbed power law up to 10 keV. The highest integrated flux was found on January 4 (MJD 55565) with $F_{[2-10\mathrm{keV}]} = (3.31 \pm 0.22) \times 10^{-12}\,\mathrm{erg\,cm^{-2}\,s^{-1}}$ and a photon index of 2.46 ± 0.05. The observations taken in April/May show the object in a lower flux state, with too poor statistics in the energy bins above 5 keV to constrain a spectral fit.

However, combining the exposures from all the observations of April/May allows a fit in the 0.4 to 10 keV range with an integrated flux of $F_{[0.4-10\mathrm{keV}]} = (4.25 \pm 0.16) \times 10^{-12}\,\mathrm{erg\,cm^{-2}\,s^{-1}}$ and a photon index of 2.74 ± 0.04.

An X-ray flux-index correlation study, performed on the entire data set, resulted in a correlation coefficient of $r = -0.88$ with an uncertainty of < 0.1. This implied a strong (negative) correlation between spectral index and integrated flux of the X-ray observations.

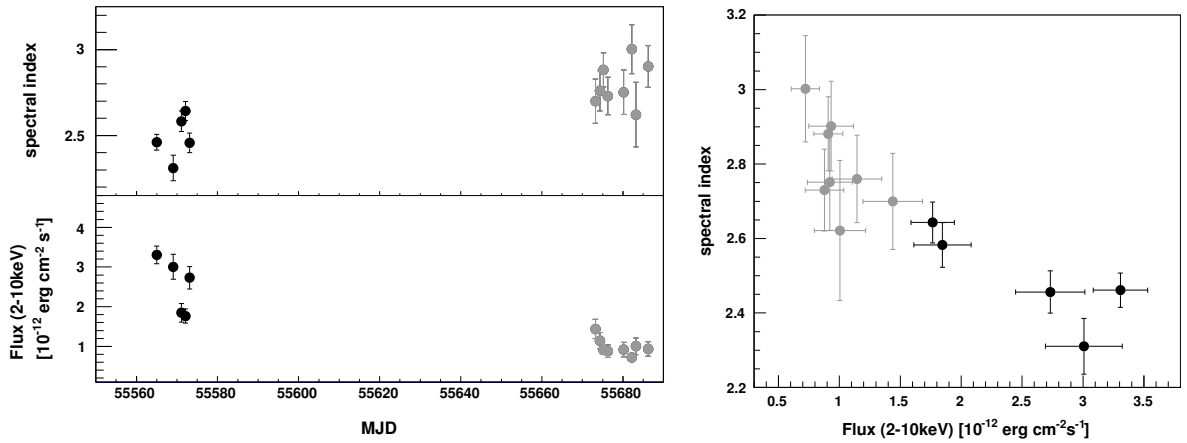

Figure 5.9.: *Swift*-XRT observations of B2 1215+30 in 2011. (Left) X-ray light curve for the integrated flux (lower panel) and the spectral index (upper panel) showing the blazar in a brighter and harder flux state in January (black points) compared to April/May (gray points). (Right) Flux-spectral index correlation in the X-ray regime in 2011. The correlation coefficient is $r = -0.88$, implying a strong (negative) correlation. Analysis courtesy: A. Furniss & J. Grube.

UV and optical observations with *Swift*-UVOT, Super-LOTIS and MDM

In the ultraviolet (UV) and optical regime, *Swift*-UVOT (Roming et al., 2005) observations were taken in January and April/May 2011. All exposures (covering different pass bands) were taken in *image mode*, where the image is accumulated on board the satellite discarding the photon timing information within each single exposure to reduce the telemetry volume and the time of transmission.

The photometry was computed using the 5 arcsec aperture and, where possible, the recommended background region (annulus, 20 to 30 arcsec radius) following the prescription in Poole et al. (2008) and Breeveld et al. (2010). A dedicated inter-calibration study between optical, UV and X-ray datasets was carried out, adopting the N_{H} parameter for the hydrogen column (ob-

tained from the LAB survey). The results were reddening corrected using $E(B-V) = 0.023$ mag (Schlegel et al., 1998). Then, the corresponding optical/UV galactic extinction coefficients were computed ($R_V = 2.667$) and applied (Fitzpatrick, 1999). The host galaxy contribution of B2 1215+30 was estimated using the PEGASE-HR code (Le Borgne et al., 2004) extended for the ultraviolet UVOT filters and by using the R-band photometric results of Nilsson et al. (2007).

For each filter, the integrated flux was computed by using the related effective frequency and not convolving the filter transmission with the source spectrum. This may produce a moderate overestimation (around 10%) of the integrated flux. The total upper limit systematic uncertainty is 15% and the resulting light curve is shown in Figure 5.10.

In the optical regime, B2 1215+30 was monitored using the Super-LOTIS (Livermore Optical Transient Imaging System[8]) robotic telescope over the period December 2010 − June 2011. In addition to these R-band observations, B2 1215+30 was observed with the 1.3 m McGraw-Hill telescope of the MDM observatory[9] during one week in May 2011 (MJD 55706 − 55709), using standard V, R, and I filters.

The optical data were bias-subtracted and flat-fielded using the routines of the Image Reduction and Analysis Facitily (IRAF; Tody, 1993, 1986). Comparative photometry with stars of known magnitude was performed and the resulting light curve in Figure 5.10 showed clear variability. The results obtained here are in line with the variability seen on the publicly available light curves from the Tuorla Observatory[10].

For the construction of the optical SED using MDM observations, the magnitudes were corrected for Galactic extinction according to Schlegel et al. (1998). The values are $A_V = 0.079$, $A_R = 0.064$, and $A_I = 0.046$, as provided by the NED.

Spectral energy distribution of B2 1215+30 in 2011

The combination of the results from the MWL data analyzes is a well sampled light curve in time and energy for the first half of 2011, shown in Figure 5.10. It covers a wide range of frequencies and the data are used to construct an SED. As no variability was detected in the high- or very-high-energy regimes, the *Fermi*-LAT data contemporaneous with the VERITAS observations in 2011 are used (MJD 55560−55720). Given the clear variability at lower frequencies, especially in X-rays, two spectra are extracted: one to represent the high X-ray state in January (MJD 55565) and the other one to represent the low X-ray state observed in April/May (using the combined spectrum from all observations between MJD 55673 − 55686). *Swift*-UVOT data simultaneous with the X-ray observations were used when available, while the quasi-simultaneous optical

[8] http://slotis.kpno.noao.edu/LOTIS/
[9] http://mdm.kpno.noao.edu/
[10] http://users.utu.fi/kani/1m/ON_325.html

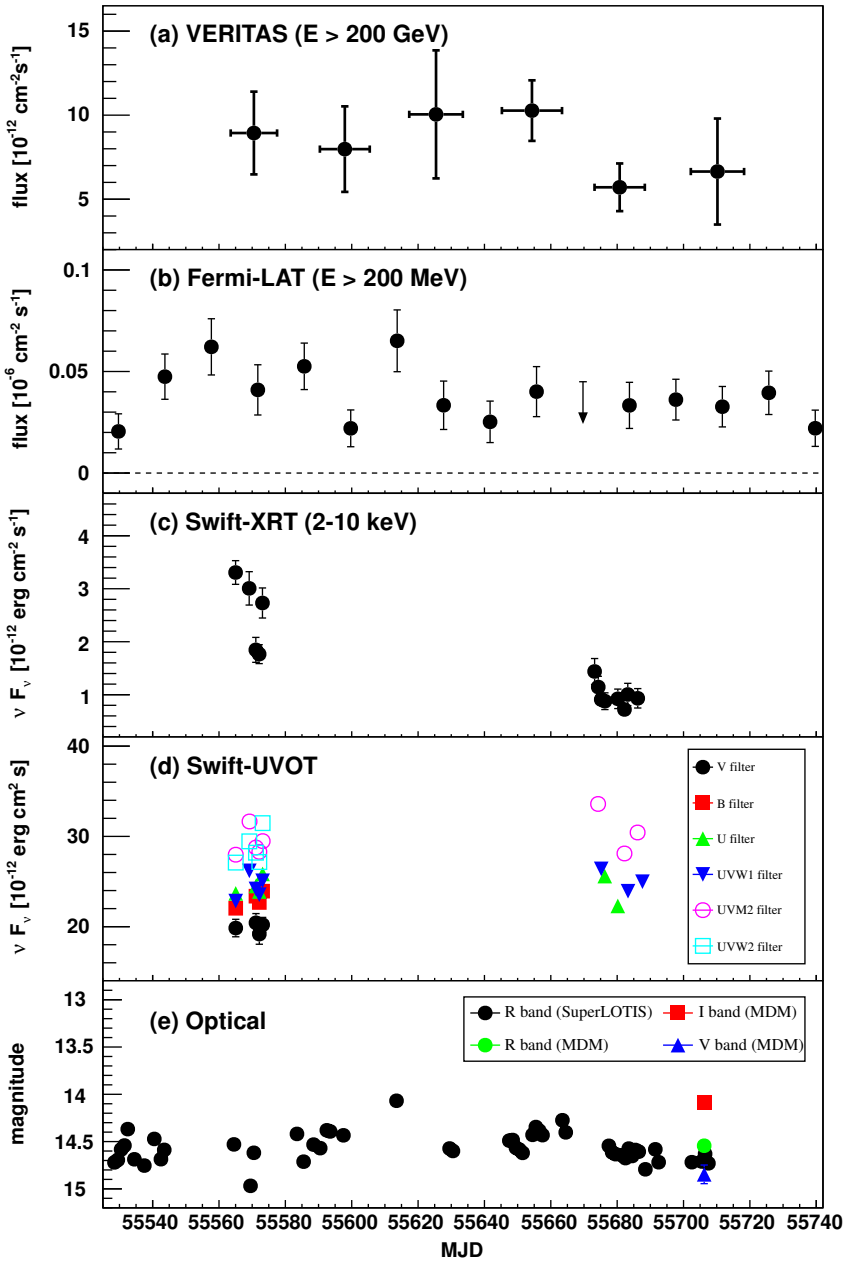

Figure 5.10.: Multi-wavelength light curve of B2 1215+30 for the first half of 2011. (a) Monthly binned VHE gamma-ray light curve above 200 GeV as measured by VERITAS. (b) Bi-weekly binned *Fermi*-LAT light curve above 200 MeV. (c) X-ray light curve measured by *Swift*-XRT. (d) *Swift*-UVOT light curve for the different band pass filters (given in the legend). (e) Optical light curve. The black points represent the measurements by Super-LOTIS in the R-band, with a statistical error of $\sim 0.1-0.2$ mag. The V, R, and I points illustrate the data from MDM observations.

spectrum from MDM (MJD 55706 − 55709) is additionally used in the SED representing the low X-ray state. To complete the low-energy part of the SED, archival data in the micrometer wavelength regime, taken from Antón et al. (2004), and radio observations, as provided by the NED, are included.

The extracted broadband SED, in the νF_ν representation, can be found in Figure 5.11. It shows a two-bump structure typical for blazars. Based on the location of the synchrotron peak between UV and X-rays, B2 1215+30 can be classified as an intermediate- or high-synchrotron-peaked blazar ($\nu_{\mathrm{sync}} \sim 10^{15..16}$) according to Nieppola et al. (2006) or Ackermann et al. (2011), respectively.

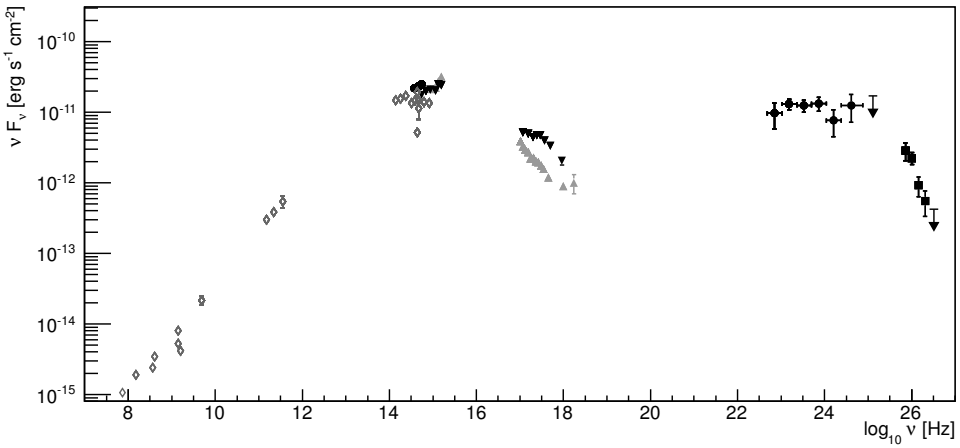

Figure 5.11.: Spectral energy distribution of B2 1215+30 in 2011. The data points are (from low to high frequencies): (◊) archival data from NED, (•) optical data from MDM, (▼) high X-ray state observed by *Swift*-XRT & UVOT, (gray ▲) low X-ray state observed by *Swift*-XRT & UVOT, (•) high-energy gamma-ray data from *Fermi*-LAT, and (■) VHE gamma-ray data from VERITAS.

What causes this emission and which mechanisms can explain the observed variability, especially in the X-ray regime, are questions which will be addressed in the following chapter by modeling the broadband emission of B2 1215+30.

6. Modeling of Blazar Emission

A powerful tool to gain insight into the physics of blazars is to model their spectral energy distribution (SED). As the emission from blazars is dominated by non-thermal emission, extending up to TeV energies, particles have to be accelerated to relativistic energies inside the jet. A short introduction into gamma-ray production mechanisms is presented in Section 6.1 in which a general overview about existing blazar emission models is given. In Section 6.2, one of these models, i.e., the synchrotron-self Compton (SSC) model, is presented in detail. It is used to model the emission of B2 1215+30 in Section 6.3 where the obtained results are discussed and put in context with other VERITAS-detected blazars.

6.1. Gamma-ray emission in blazars

Except for possible production by top-down processes such as the decay of heavy particles, VHE gamma rays are produced only in the interactions of accelerated charged particles (electrons or protons or both) with ambient matter or radiation fields. In the following, a brief overview of particle acceleration mechanisms is given (Section 6.1.1) and the main non-thermal emission processes are outlined (Section 6.1.2). Some common models for the emission in blazar jets are presented in Section 6.1.3.

6.1.1. Acceleration of charged particles

For the production of the observationally required non-thermal power-law distribution of particles in the jets of AGN (see, e.g., Kirk & Duffy, 1999, for a review), Fermi processes (Fermi, 1949) are the most efficient and plausible mechanisms (Rieger et al., 2007).

First-order Fermi acceleration (e.g., Blandford & Eichler, 1987), sometimes also referred to as diffusive shock acceleration, is a process where particles cross shock fronts multiple times, with an energy gain per crossing proportional to the shock velocity β. Only a few particles can be accelerated to extreme high energies before they escape, thus naturally accounting for the commonly required power-law particle spectra $n(\gamma) \propto \gamma^{-q}$ with spectral indices $q \simeq 2$. As this process is also a sufficiently fast and efficient mechanism, first-order Fermi

acceleration at strong shocks is among the most common scenarios for particle acceleration in jets.

Second-order Fermi acceleration is caused by turbulences downstream of shocks where particles gain or lose energy through scattering. As the probability of gaining energy by head-on scattering is larger than losing energy by rear-on scattering, the energy of particles will statistically increase in the end.

However, Fermi processes cannot account for all observational phenomena (Rieger et al., 2007). Alternative acceleration mechanisms, such as magnetic reconnection (e.g., Schopper et al., 1998), and shear-layer acceleration (e.g., Rieger & Duffy, 2006) have been proposed, e.g. to account for different spectral indices of the non-thermal particle spectrum. In the end, it is most likely that a combination of these different processes takes place in the extreme environment of blazars.

6.1.2. Non-thermal emission processes

Once the particles have been accelerated to VHE energies, they emit photons through several processes. The most important are outlined in the following and can be found in textbooks (e.g., Rybicki & Lightman, 1979; Longair, 1992).

Synchrotron radiation

Any charged particle moving through a magnetic field B will follow a spiral trajectory and consequently emits radiation. In the case of relativistically moving particles this is called *synchrotron radiation* and is most efficient for light particles like electrons. The average energy-loss rate of an electron in a magnetic field is given by

$$-\left(\frac{dE}{dt}\right)_{\text{sync}} = \frac{4}{3} c\, \sigma_T\, u_B\, \gamma^2 \tag{6.1}$$

where $u_B = B^2/8\pi$ is the magnetic field energy density, σ_T is the Thomson cross section, and γ is the electron energy (defined by $E = \gamma m_e c^2$). The typical time scale in which an electron looses its energy is given by the cooling time

$$\tau_{\text{sync}} = \frac{E}{(dE/dt)_{\text{sync}}} \propto \frac{1}{B^2 E}. \tag{6.2}$$

If the electron distribution is a power law of the form $n(\gamma) \propto \gamma^{-p}$, electrons at the high-energy end loose their energy first and will deviate from the original power law. The emitted synchrotron

spectrum is of the form

$$F_\nu \propto B^{(p+1)/2}\,\nu^{-(p-1)/2}, \tag{6.3}$$

and follows in principle the power-law form of the electron distribution. At a certain minimum energy, the electrons will absorb the synchrotron photons by synchrotron-self absorption (the medium becomes optically thick). Below this minimum frequency the photon spectrum is given by $F_\nu \propto B^{-(1/2)}\nu^{5/2}$, depending only on the magnetic field strength.

Inverse Compton scattering

The interaction of relativistic electrons with low-energy photons through inverse Compton (IC) scattering provides one of the principal gamma-ray production processes, where the energy is transferred from the high-energy electrons to the photons. The average loss-rate of the electron in single IC scatterings is

$$-\left(\frac{dE}{dt}\right)_{\rm IC} = \frac{4}{3} c\sigma_T\, u_{ph}\, \gamma^2 \tag{6.4}$$

where u_{ph} is the energy density of isotropic seed photons. In the classical Thomson regime (elastic scattering) the photons in the electron rest frame have energies much smaller than the electron rest mass energy. The cross section in that case is approximately constant ($\propto \sigma_T$) and the maximum energy of the up-scattered photons is $E_{max} = 4\gamma^2 E_{ph}$ while their average energy is $\langle E\rangle = 4/3\gamma^2 E_{ph}$. At high energies, quantum physics effects become important and the scattering is no longer elastic. This is the so-called Klein-Nishina regime in which the scattering cross section begins to decrease dramatically (i.e., when $h\nu/(m_e c^2)\,\gamma \sim 1$). This means as well that Compton scattering is not very efficient at very high energies and the maximum outgoing-photon energy is $E_{max} = \gamma m c^2$.

If the electron distribution is a power-law distribution, the resulting IC spectrum can, in general, also be described by a power law. In the Thomson regime, it follows the synchrotron spectrum, i.e. $F_\nu \propto \nu^{-(p-1)/2}$, while in the Klein-Nishina limit it is steeper, $F_\nu \propto \nu^{-p}$.

Neutral pion decay

As the lightest hadrons with $m_\pi \approx 140$ MeV, pions are among the end products of most hadronic cascades. Charged ($\pi^\pm$) and neutral (π^0) pions are produced with the same probability in proton-proton or photon-meson interactions. Most neutral pions decay almost immediately into two gamma rays, while charged pions usually undergo further interactions due to their longer lifetime before they eventually decay into electrons and neutrinos.

Bremsstrahlung

When charged particles are deflected in electric fields, they radiate bremsstrahlung and the emitted photon spectrum follows the power-law form of the accelerated particles with the same spectral index. Ultra-high-energy cosmic rays (UHECR; $E > 10^{19}$ eV) can emit via bremsstrahlung gamma rays in the TeV regime.

6.1.3. Blazar emission models

Blazar SEDs span a wide range in energy, making simultaneous multi-wavelength observations an important tool to disentangle the underlying non-thermal processes. A review of the different blazar models is given, e.g., in Böttcher (2012).

In the most common models, the SED of blazars is described by emission produced inside the blazar jets and the low-frequency peak is believed to be synchrotron emission from relativistic electrons. For the origin of the high-energy peak, two different scenarios exist which are dominated by either leptonic or hadronic emission, depending on the particles responsible for the emission. Therefore, a good spectral characterization of the high-energy peak is essential to reveal the dominant emission processes which cannot be infered from the synchrotron peak.

Leptonic models

In leptonic models, the high-energy component arises from inverse Compton scattering of high-energy electrons with low-energy target photons. These seed photons can be either from the synchrotron radiation of the same electron population (synchrotron-self Compton; SSC) or from different radiation fields in the blazar environment (external Compton; EC). In both models, the broadband emission comes from the same particle population within the jet which is supported by the correlation seen between X-ray and VHE gamma-ray variability.

In the SSC models (e.g., Marscher & Gear, 1985; Maraschi et al., 1992; Böttcher & Chiang, 2002), a population of relativistic electrons moves along the magnetized jet, generating synchrotron photons with frequency $\nu_{\rm sync} \propto B\,E^2$, where B is the magnetic field strength and E is the energy of the particles. These photons are up-scattered in energy by the same electron population that emitted them, to frequencies $\nu_{\rm IC} \propto \nu_{\rm sync} E^2 \propto BE^4$ (see Section 6.2 for a detailed description). While these SSC models have been successfully applied to BL Lac objects like Mrk 421 (Abdo et al., 2011) or Mrk 501 (Abdo et al., 2011), they have difficulties to explain the dominant gamma-ray component observed, e.g., in FSRQs or low-frequency-peaked blazars (Dermer & Lott, 2012).

By introducing external photon fields, the gamma-ray dominance can usually be successfully modeled as an additional gamma-ray component can emerge (as, e.g., in the FSRQ 3C 279

Böttcher, 2007). Possible photon fields in EC models are (i) optical/UV/X-ray emission from the disk (e.g., Dermer et al., 1992; Dermer & Schlickeiser, 1993), (ii) reprocessed optical/UV emission from circumnuclear material (e.g. the BLR, Sikora et al., 1994; Dermer et al., 1997) (iii) infrared emission from warm dusk (e.g., Błażejowski et al., 2000) and/or (iv) the cosmic microwave background (CMB, e.g., Harris & Krawczynski, 2002).

In addition to the different target photon sources several variations of multi-zone-jet models have been proposed to account for rapid variability and large Doppler factors, required to describe the SED in some objects. These include the spine-sheath model of Sol et al. (1989) (or Tavecchio & Ghisellini, 2008), the decelerating-jet model of Georganopoulos & Kazanas (2003), as well as several internal-shock models (e.g., Graff et al., 2008; Joshi & Böttcher, 2011).

(Lepto-) Hadronic models

In the dominant hadronic scenarios, the high-energy component is explained by gamma-ray emission from VHE protons. To accelerate protons to the necessary ultra-relativistic energies ($E_p \geq 10^{18}$ eV), high magnetic fields of several tens of Gauss are required (much higher than in leptonic models). These VHE protons can produce secondary gamma rays, e.g., by (i) interaction with matter inside the jet (e.g., via relativistic blast waves, Pohl & Schlickeiser, 2000), (ii) directly via synchrotron emission in a highly magnetized jet (proton-synchrotron model, e.g., Aharonian, 2000), or (iii) indirectly through secondary electrons produced in a cascade induced by proton interactions with external photons ($p - \gamma$ model, e.g., Mannheim, 1993; Mücke & Protheroe, 2001). However, the low plasma density usually found in the jets results in relatively long cooling times, making it challenging to account for short-term variability.

The most attractive feature of hadronic models comes from the multi-messenger link. As hadronic interactions imply neutrino production, a detection of an AGN by a neutrino telescope like IceCube[1] would clearly favor hadronic models. At the same time it would imply acceleration of particles up to very high energies, strongly suggesting AGN as sources of UHECRs observed on Earth. On the other hand, hadronic models require in general more extreme and fine-tuned model parameters than leptonic models − one of the reasons why in general leptonic models are still preferred.

6.2. Synchrotron-self Compton model

The synchrotron self-Compton (SSC) models stand out by their simplicity, requiring only a small number of parameters to describe the broadband emission of blazars. In Section 6.2.1, the

[1] `http://icecube.wisc.edu/`

SSC model from Böttcher & Chiang (2002) is described in detail. The different parameters and possible constraints are discussed in Section 6.2.2 using the model code provided by M. Böttcher.

6.2.1. Model description

The radiating plasma is modeled as a spherical emission region ("blob") of comoving radius R which is propagating with relativistic speed $\beta_\Gamma c$ along the jet axis. The jet is directed at a small angle θ with respect to the line of sight to the observer. It is fixed to the superluminal angle, $\theta \simeq 1/\Gamma$, for which the (bulk) Lorentz factor Γ equals the Doppler factor $D = [\Gamma(1-\beta_\Gamma \cos\theta)]^{-1}$. As the results of the model depend mainly on the Doppler factor, other combinations of θ and Γ resulting in the same Doppler factor are also possible.

Into the emission region, a population of ultra-relativistic non-thermal electrons is continuously injected following a power-law distribution with low- and high-energy cutoffs γ_1 and γ_2, respectively, so that

$$Q_\mathrm{e}(\gamma, t) = Q_0(t)\, V_b\, \gamma^{-q} \tag{6.5}$$

while Q_0 is related to the total particle density n_e by $Q_0 = n_e\,(1-q)/(\gamma_2^{1-q} - \gamma_1^{1-q})$ and V_b is the co-moving volume of the emission region. As the blob is propagating along the jet, the electrons lose energy through synchrotron emission in a tangled magnetic field of co-moving strength B and through Compton scattering on the synchrotron radiation field. This is a simple adaption of the internal shock model where the particles, efficiently accelerated at the shock front, fill the downstream region of the shock.

Within the model, a quasi-equilibrium is assumed between particle injection, radiative cooling and particle escape. The latter is described by an escape timescale parameter $\eta_\mathrm{esc} \geq 1$ with $t_\mathrm{esc} = \eta_\mathrm{esc} \cdot R/c$. As a result, a break in the electron distribution will occur self-consistently at a Lorentz factor γ_b, where $t_\mathrm{esc} = \tau_\mathrm{cool}(\gamma_\mathrm{b})$. Depending on whether γ_b is larger or less than γ_1, the system will be in the slow or fast cooling regime. In the slow cooling regime ($\gamma_\mathrm{b} > \gamma_1$), the equilibrium-electron distribution (EED) will be a broken power law of the form

$$n_e(\gamma) \propto \begin{cases} \gamma^{-q} & \text{for } \gamma_1 < \gamma < \gamma_\mathrm{b} \\ \gamma^{-(q+1)} & \text{for } \gamma_\mathrm{b} < \gamma < \gamma_2 \end{cases} \tag{6.6}$$

while in the fast cooling regime ($\gamma_\mathrm{b} < \gamma_1$), the broken power law is given by

$$n_e(\gamma) \propto \begin{cases} \gamma^{-2} & \text{for } \gamma_\mathrm{b} < \gamma < \gamma_1 \\ \gamma^{-(q+1)} & \text{for } \gamma_1 < \gamma < \gamma_2 \end{cases} \tag{6.7}$$

The resulting spectral index below the break in the fast cooling regime, $q_1 = 2$, is rather typical for astrophysical sources and is a direct result of cooling through synchrotron or IC scattering in the Thomson regime. In other SSC models, where the injected electron distribution is described by a broken power law rather than obtained self-consistently, this might be a result of first-order Fermi acceleration at the shock front.

The minimum electron energy is directly related to the radiative cooling in the emission region. It is given by

$$\gamma_{\min} = \frac{3 m_e c^2}{4 c \sigma_T \, \tau_{cool} (u_{ph} + u_B)} \tag{6.8}$$

and can, in principle, cool down to $\gamma \sim 1$ if the source evolution time is long enough. However, as the minimum energy is inversely proportional to the cooling time, high-energy particles ($\gamma \sim 10^5$) lose their energy more rapidly than low-energy electrons ($\gamma \sim 10^3$). In other words, a minimum Lorentz factor of $\gamma_{\min} \gg 1$ is usually obtained in the model, implying that the acceleration process at the shock front is very efficient, which results in a highly relativistic electron distribution.

Once the quasi-equilibrium electron distribution is obtained, the resulting kinetic power in relativistic electrons, is evaluated

$$L_e = \pi R^2 \Gamma^2 \, \beta_\Gamma c \, m_e c^2 \int_1^\infty d\gamma \, n_e(\gamma) \gamma \tag{6.9}$$

and compared to the power carried in the magnetic field (Poynting flux),

$$L_B = \pi R^2 \Gamma^2 \, \beta_\Gamma c \, u_B \tag{6.10}$$

where $u_B = B^2/(8\pi)$ is the magnetic energy density. The ratio of the two is the resulting relative partition parameter $\epsilon_\mathrm{B} \equiv L_\mathrm{B}/L_\mathrm{e}$. It can be used to obtain information about the energy balance within the jet which contains information on the jet launching and acceleration mechanisms.

Altogether, the SSC model described here has eight free (but correlated) parameters, listed in Table 6.1, whereas the injection luminosity is related to the electron density in the blob by $L_\mathrm{inj} \propto R^2 D^2 Q_0$. In all model calculations, the luminosity distance to the source is calculated using the standard ΛCMD cosmology parameters with $\Omega_m = 0.3$ and $\Omega_\Lambda = 0.7$ and a Hubble constant of $H_0 = 70$ (km/s)/Mpc. Additionally, the absorption of VHE gamma rays on the extragalactic background light is taken into account using the EBL model of Finke et al. (2010)[2].

[2] This absorption model is consistent with the absorption derived from EBL models of Franceschini et al. (2008) and Gilmore et al. (2009).

Parameter	Symbol	Value	Parameter	Symbol	Value
Electron distribution					
Injection luminosity	$L_{\rm inj}$ [erg/s]	$4 \cdot 10^{43}$	Doppler factor	$D = \Gamma$	20
Low energy cutoff	γ_1	$4 \cdot 10^4$	Magnetic field strength	B [G]	0.5
High energy cutoff	γ_2	$5 \cdot 10^5$	Escape time parameter	$\eta_{\rm esc}$	3
Spectral index	q	2.6	Emission region radius	R [cm]	$3 \cdot 10^{15}$

Table 6.1.: Input parameters for the SSC model used within this thesis. The different parameters are explained within the text. The listed values are obtained from the modeling of the emission of Mrk 421 in 2006 ($z = 0.031$, Acciari et al., 2009a). They are referred to in Section 6.2.2 as a baseline emission model.

6.2.2. Model parameter and constraints

In general, most of the SSC input parameters can be constrained by simultaneous observations in different wave bands (Tavecchio et al., 1998). They are most stringent if fast variability and/or correlations between different frequency bands are observed. It is beyond the scope of this thesis to go through all possible constraints, but I will show on a few examples how the modeled emission changes in dependence of some of these input parameters.

As a baseline parameter set, the values used to model the emission of the prototype VHE blazar Mrk 421 ($z = 0.031$) in April 2006 are used (Acciari et al., 2009a, listed in Table 6.1). In the first step of the model, the equilibrium-electron distribution (EED) is obtained, shown in the right side of Figure 6.1. It shows a broken power law with a break at $\gamma_b = 4 \cdot 10^4 = \gamma_1$ and is thus in the fast cooling regime (Eq. 6.7) with a minimum electron Lorentz factor of $\gamma_{min} \simeq 5 \cdot 10^3$. The overall radiative output is shown in the right side of Figure 6.1 in the typical νF_ν-representation and yields results close to equipartition ($\epsilon_B \simeq 0.4$).

The first peak in the SED is due to synchrotron emission and shows several distinct spectral features. The low-energy break (around 10^{15} Hz) arises from the low-energy cutoff in the electron distribution below which the spectral shape of the synchrotron emission is determined by the low-frequency synchrotron spectrum of a mono-energetic electron. The synchrotron-peak frequency (at around 10^{17} Hz) is proportional to the break energy of the EED, given by $\nu_{\rm sync} \propto \gamma_b^2 B$ (Kino et al., 2002). The spectral shape below and above the peak are given by Eq. 6.3 and follow the shape of the cooled electron distribution. This means that through observations in the optical to X-ray regime, the spectral index of the electron distribution can be constrained. At around 10^{19} Hz, a steep cutoff in the synchrotron emission occurs which is purely determined by the maximum energy of the accelerated electrons. In other words, if a cutoff in the synchrotron peak of the SED is observed, one can directly obtain the maximum Lorentz factor γ_2 of the electron

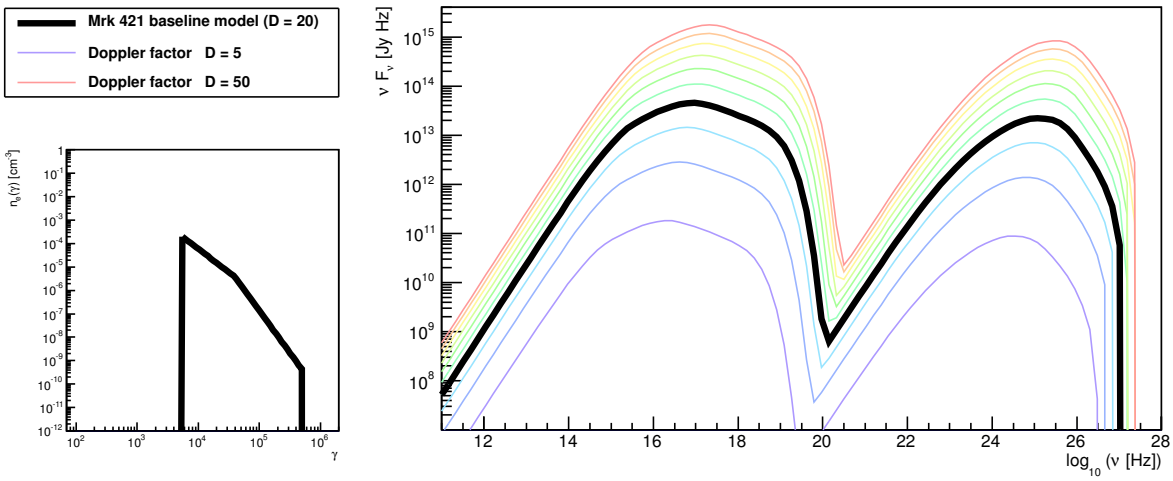

Figure 6.1.: SSC model for Mrk 421 in 2006 (black lines) using the input parameter listed in Table 6.1. (Right) The obtained equilibrium-electron distribution shows a broken power-law distribution in the fast-cooling regime. (Left) SED as obtained by the applied SSC model. The black curve represents the baseline model parameters, while the rainbow-colored SEDs show the observed emission from the same EED by changing the Doppler factor from $D = 5$ to $D = 50$ in steps of five. See text for details.

distribution.

The second peak in the SED is due to inverse Compton scattering which follows, in general, the shape of the synchrotron peak. The IC-peak frequency is related to the synchrotron-peak frequency as $\nu_{\rm comp} \simeq (4/3)\,\gamma_b^2 \nu_{\rm sync}$. In the MeV/GeV range, the IC spectrum comes mainly from scattering in the Thomson regime. Therefore, the spectral index of this emission should be similar to the index of the scattered radiation field. However, the complexity of the scattering (several different regimes from the synchrotron emission) produces a curved spectrum below the IC peak and spectral features, as observed in the synchrotron emission, are smeared out (Katarzyński, 2012). In the GeV/TeV regime, the observed fluxes decrease steeply, due to Klein-Nishina effects and (especially for more distant blazars) EBL absorption.

Doppler factor

As already mentioned in Section 5.1.1, the Doppler factor links the emission in the rest frame of the jet to the observed emission. Changing the Doppler factor thus changes the observed luminosities and frequencies. By keeping the same equilibrium-electron distribution, the frequencies are "blue-shifted" for increasing Doppler factors ($\propto D$) while the luminosities are

strongly boosted ($\propto D^4$), as indicated by the color-coded SEDs in Figure 6.1. As in the model the Doppler factor is equivalent to the bulk Lorentz factor, a constrain on its upper value can be obtained by the unification schemes: a very high Doppler factor means a very small viewing angle (e.g., $D = 50$ means $\theta_{sl} \simeq 1.15°$) which is statistically unlikely if blazars are a sub-class of the overall AGN population. For small Doppler factors[3], the boosting is relatively moderate, resulting in low fluxes which makes it difficult to observe them, especially in the VHE regime. A lower limit on the Doppler factor can usually be obtained from superluminal motion measurements (Section 5.1) and/or the transparency of the source to VHE gamma rays (Dondi & Ghisellini, 1995).

Magnetic field

The influence of the magnetic field strength B inside the blob is demonstrated in Figure 6.2. An increase of the magnetic field inside the blob results in shorter cooling time scales (Eq. 6.2) and changes the equilibrium-electron distribution. The high-energy electrons cool faster and thus a larger number of low-energy electrons fill the blob before they escape. This results in a lower minimum Lorentz factor of the EED. Since the injection luminosity of the uncooled electron distribution is kept constant, the normalization (e.g., at the break energy) gets lower.

The obtained SEDs are shown in the left side of Figure 6.2. An increase of the magnetic field strength increases the synchrotron-peak frequency by the same order. This dependency can, in general, be used to constrain the break frequency γ_b ($= \gamma_1$ in the fast cooling regime) and the magnetic field. In the Thomson regime, this can be expressed as (Tavecchio et al., 1998):

$$B = \frac{1+z}{D} \frac{\nu_{\mathrm{sync}}^2}{2.8 \times 10^6 \, \nu_{\mathrm{comp}}} \tag{6.11}$$

and is one of the major constraints on the magnetic field. In addition to the shift of the synchrotron-peak frequency, a smaller value for γ_{min} shifts the low-frequency cutoff of the synchrotron peak towards lower frequencies. This results in a different shape of the low-energy part of the IC spectrum. The total luminosity of the synchrotron peak and the total luminosity of the Compton peak are related to each other by $L_{\mathrm{comp}}/L_{\mathrm{sync}} = u_{\mathrm{sync}}/u_{\mathrm{B}}$ which can be expressed in terms of the magnetic field by:

$$B^2 \propto \frac{1}{R^2 D^4} \frac{\nu_{\mathrm{sync}} L_{\mathrm{sync}}^2(\nu_{\mathrm{sync}})}{\nu_{\mathrm{comp}} L_{\mathrm{comp}}(\nu_{\mathrm{comp}})} \tag{6.12}$$

[3] The lowest Doppler factor is set to $D = 5$ ($\theta_{sl} \simeq 11°$). Lower values of D would result in larger jet viewing angles and hence would not be classified as blazar.

where νL_ν is the observed luminosity at the synchrotron/inverse Compton-peak frequency.

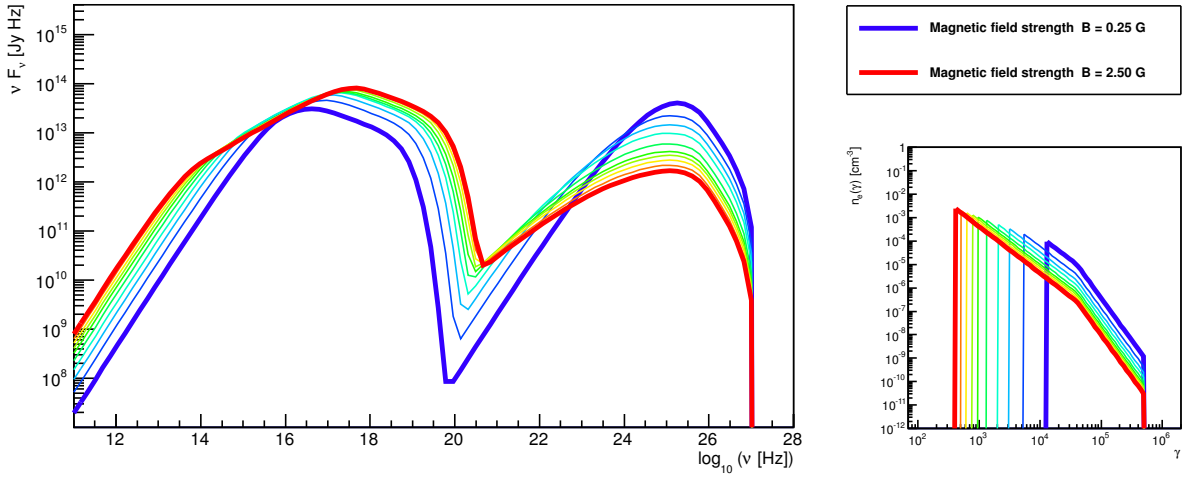

Figure 6.2.: Results of the SSC model as obtained by changing the magnetic field strength. The rainbow colors represent the values from $B = 0.25$ G to $B = 2.5$ G in steps of 0.25 G. All other input parameter are kept constant, as listed in Table 6.1. The left part of the figure shows the SEDs as obtained by the applied SSC model. The colors correspond to the observed emission from the equilibrium-electron distribution shown on the right side. See text for details.

Size of the emission region

Following causality arguments, any observed variability leads to an upper limit on the size of the emission region through

$$R \leq c\delta t_{\mathrm{var}} \frac{D}{1+z}. \tag{6.13}$$

Thus, measuring very fast variability results in a very small emission region which poses severe problems to one-zone models: the smaller the emission region is, the higher gets the electron density in this region and the shorter is the mean free path for the electrons. Thus, less synchrotron photons are emitted and the observed synchrotron emission cannot be accounted for in the model. A possible solution to this problem would be to increase the Doppler factor to very large values. However, this would also increase the high-energy-peak luminosities and such large Doppler factor are generally considered as unlikely. Therefore, it is argued that the fast variability seen in the VHE regime originates from a different region than, e.g., the X-ray or radio emission; supporting models with multiple emission zones.

6.3. Modeling the emission of B2 1215+30

In the following, the SED of B2 1215+30, obtained from quasi-simultaneous observations in 2011 presented in Section 5.2.3, is modeled with the SSC model detailed above. In the first step, all obtained data are taken into account assuming a redshift of $z = 0.13$. As the data in the radio to micrometer wavelength regime are archival only, their influence on the obtained model parameters is evaluated by ignoring them during the modeling. Due to the distance uncertainty, it will later be discussed how the results are affected if a redshift of $z = 0.237$ is adopted instead.

SSC model applied to the full data set

The lines in Figure 6.3 represent the results of the SSC model for which the archival data in the micrometer wavelength regime are taken into account. The overall SED for both X-ray states in 2011 can be well described by the model. The model parameters used are listed in Table 6.2 (Column A).

The used Doppler factor is $D = 30$. Following the discussion above, a lower Doppler factor would require a lower magnetic field and hence a larger emission region, resulting in variability time scales longer than days or even weeks. This lower Doppler factor scenario would contradict the measurements of X-ray variability during the January observations. The magnetic field strength is found to be quite low, resulting in a very small relative partition parameter. A magnetic field far below equipartition ($\epsilon_B \approx 0.1 - 1$), as found here, might indicate a particle-dominated jet, in which the magnetic field in the emission region is self-generated and/or amplified in shocks. In contrast, a magnetic field near or above equipartition would be consistent with a Poynting-flux-dominated jet in which magnetic field energy is transferred to particles, reaching approximate equipartition in the high-energy emission zone.

In order to account for the two different X-ray states observed in 2011, the electron injection spectral index together with the magnetic field strength within the modeled emission region were changed. The injection index during the high X-ray state in January ($q = 2.8$) is found to be harder than during the low X-ray state in April/May ($q = 3.4$); both tightly constrained by the energy spectrum measured with *Swift*-XRT. Under the assumption that the particles in the jet are accelerated within relativistic shocks, the spectral change in the electron distribution may be explained by a change in the shock field obliquity: a larger angle between magnetic field and shock front results in a harder particle spectrum (see, e.g., Sironi & Spitkovsky, 2009). This change of the injection spectrum also leads to flux variations in the high-energy peak. However, neither *Fermi*-LAT nor VERITAS are sensitive to those variations given the flux level of the source during the observation period reported here.

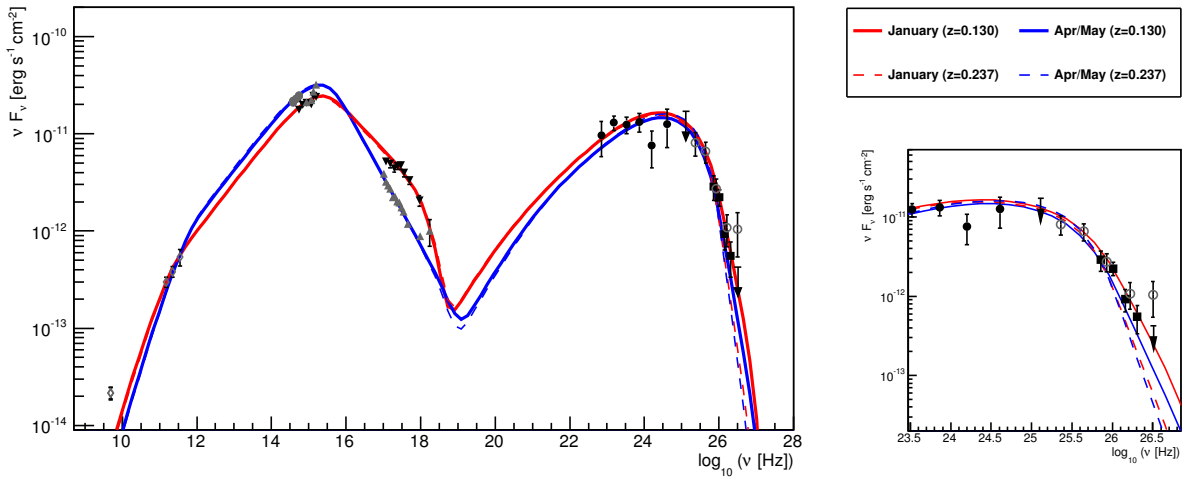

Figure 6.3.: Spectral energy distribution of B2 1215+30 during 2011 together with the SSC model assuming a redshift of $z = 0.130$ (solid lines) and a redshift of $z = 0.237$ (dashed lines). The data points are the following (from low to high frequencies): (◊) archival data, (•) optical data from MDM, (▼) high X-ray state observed by *Swift*-XRT & UVOT, (▲) low X-ray state observed by *Swift*-XRT & UVOT, (•) *Fermi*-LAT, (■) VERITAS, and (○) MAGIC. The blue lines represents the model for the low X-ray state in January and the red lines the model for the high X-ray state in April/May, respectively. The right side of the figure is a zoom into the high-energy peak. The model parameters are given in Table 6.2. See text for details.

SSC model applied to contemporaneous data only

The results above are obtained by taking the archival data at around 10^{11} Hz into account. At those frequencies, a spectral break occurs in the modeled emission due to the low-energy cutoff in the equilibrium electron distribution. The position of this break is determined by the escape time scale, resulting in a large value for $\eta_{\rm esc}$. Due to possible variability in this wave band, the SED of B2 1215+30 is also modeled ignoring those archival data. This is illustrated in Figure 6.4 for the January data set. The only changes made to the model parameters are to reduce the value of $\eta_{\rm esc}$ and, at the same time, reduce the electron injection power $L_{\rm inj}$ by the same order. In this way, the high-energy part of the EED is kept the same while the minimum Lorentz factor increases. This means that the escape time scale gets shorter and the low-energy break in the SED occurs at higher frequencies. It was found that a value up to ten times smaller for $\eta_{\rm esc}$ could be used to model the SED while the lowest value is constrained by the low-energy data points of the *Fermi*-LAT spectrum. The values are listed in Column B of Table 6.2 for the January

	High X-ray state in January			Low X-ray state in Apr/May		
	(A)	(B)	(C)	(A)	(B)	(C)
z	0.13	0.13	0.237	0.13	0.13	0.237
$L_{\rm inj}$ [erg/s]	2.5×10^{46}	2.5×10^{45}	6.5×10^{46}	1.9×10^{46}	1.9×10^{45}	6.4×10^{46}
γ_1	3.0×10^{4}	3.0×10^{4}	2.7×10^{4}	4.5×10^{4}	4.5×10^{4}	5.0×10^{4}
γ_2	8.0×10^{5}	8.0×10^{5}	8.0×10^{5}	2.0×10^{6}	2.0×10^{6}	2.0×10^{6}
q	2.8	2.8	2.8	3.4	3.4	3.4
η_{esc}	3300	330	6000	2500	250	5000
B [G]	0.02	0.02	0.015	0.01	0.01	0.005
D	30	30	50	30	30	50
R [cm]	5.0×10^{16}	5.0×10^{16}	5.0×10^{16}	1.3×10^{17}	1.3×10^{17}	1.9×10^{17}
L_e(jet) [erg/s]	5.0×10^{44}	2.9×10^{44}	1.4×10^{45}	6.5×10^{44}	3.6×10^{44}	2.4×10^{45}
L_B(jet) [erg/s]	3.4×10^{42}	3.4×10^{42}	5.3×10^{42}	5.7×10^{42}	5.7×10^{42}	8.5×10^{42}
$\epsilon_B = L_B/L_e$	6.78×10^{-3}	1.16×10^{-2}	3.76×10^{-3}	8.74×10^{-3}	1.59×10^{-2}	3.52×10^{-3}
δt_{var} [h]	17.4	17.4	11.4	45.3	45.3	43.5

Table 6.2.: SSC model parameters for B2 1215+30 in 2011 for the low- and high-X-ray state. The upper part of the table are the input parameters, the lower are the output parameters derived from the model. The columns are the following: (A) all data including archival micro-meter wavelength data; (B) contemporaneous data only; (C) same as (A) but with a different redshift assumption. See text for details.

and April/May observations. With this lower escape time scale value, the system is closer to equipartition because the injection power for the electron distribution is lower (with the same value for the magnetic field strength). This clearly shows that due to the lack of simultaneous data in the 10^{11} Hz domain, $\eta_{\rm esc}$ and $L_{\rm e}$ are unconstrained, resulting in a range of parameter combinations that describe the observed SED well.

SSC model assuming a different redshift

Another difficulty of the modeling and the possible interpretation is the uncertainty on the redshift. The same model is therefore applied to the SED using $z = 0.237$, shown in Figure 6.3. It turned out that both X-ray states can as well be modeled by a change of the electron injection spectral index together with the magnetic field strength. In this case, the Doppler factor needs to be larger ($D = 50$, see Column C in Table 6.2) to compensate for the EBL absorption at high energies and the model-predicted fluxes are found to be slightly below the VERITAS spectral points. Nevertheless, this is still compatible with the VERITAS measurement considering systematic errors, therefore, this redshift cannot be excluded.

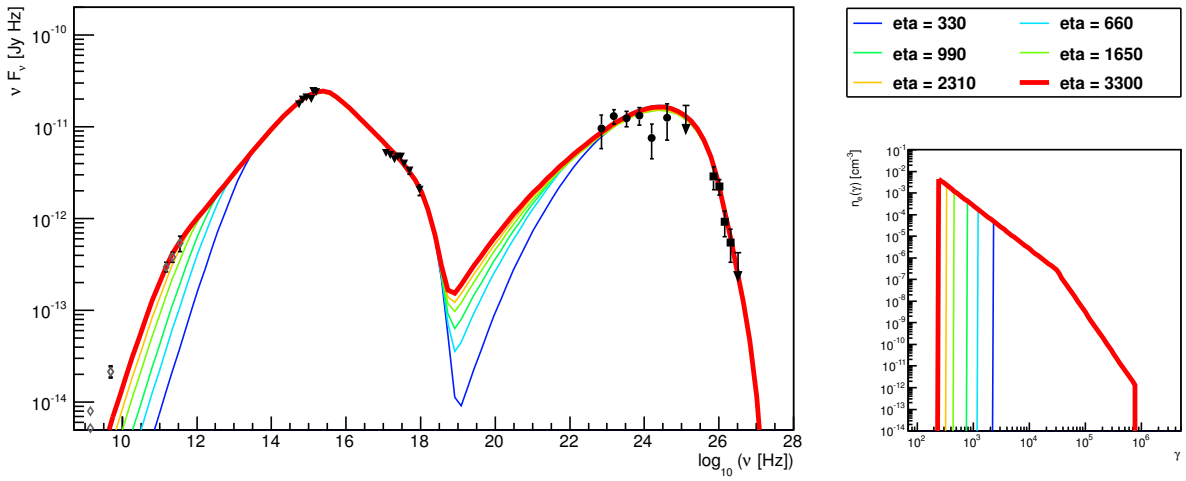

Figure 6.4.: Results of the SSC model for the January data set as obtained by changing the escape time scale parameter η_{esc} and the injection luminosity (by the same order). The rainbow colors represent values from $\eta_{\mathrm{esc}} = 330$ to $\eta_{\mathrm{esc}} = 3300$ as given in the legend, data points are explained in Figure 6.3. All other input parameters are kept constant, as listed in Column A of Table 6.2. (Left) SEDs as obtained by the applied SSC model. (Right) Equilibrium-electron distribution. See text for details.

6.3.1. Discussion

To put the above presented results of the modeling of B2 1215+30 into a wider context, they are compared to those obtained by modeling other VHE blazars. Therefore, all the VERITAS-detected blazars which have contemporaneous MWL data and have been modeled with the same SSC model (i.e., the one of Böttcher & Chiang, 2002) are used. In total, nine blazars are found and the parameters extracted from the modeling are listed in Table 6.3. Three of those blazars − 1ES 0806+524 (Acciari et al., 2009b), Mrk 421 (Acciari et al., 2009a), and W Comae (Acciari et al., 2008, 2009c) − were found in different flux states during the MWL observations and have more than one set of model parameters. PKS 1424+240 (Acciari et al., 2010a) and 3C 66A (Abdo et al., 2011) have been modeled using different redshift assumptions. While PKS 1424+240 will not be included in the comparison study due to the current lack of redshift constraint, two redshift values are given in Table 6.3 for 3C 66A, i.e. $z = 0.3$ and $z = 0.444$, as they enclose the recently published redshift limits which were found to be in the range of $0.3347 < z \leq 0.41$ (Furniss et al., 2013).

As one can see in Table 6.3, most of the parameters used to model the SED of B2 1215+30 are well within the range of those used for previously detected blazars. The Doppler factor, for

Source	z	L_e [10^{44} erg/s]	γ_1 [10^3]	γ_2 [10^5]	q	B [G]	R [10^{16} cm]	D	$\eta_{\rm esc}$	$\epsilon_{\rm B}$	$\delta t_{\rm var}$ [hr]	ref
B2 1215+30 (high)	0.130*	5.0	30	8	2.8	0.02	5	30	3300	0.00678	17.4	
B2 1215+30 (low)	0.130*	6.5	45	20	3.4	0.01	13	30	2500	0.00874	45.3	
RBS 0413	0.190	0.297	70	10	2.4	0.1	1.1	20	10	0.06	6.06	1
1ES 0414+009	0.287	3.07	200	50	3.5	0.008	21	40	120	0.055	62.5	2
RX J0648+1516	0.179	0.75	67	10	4.8	0.14	2	20	100	0.16	10.9	3
RGB 0710+591	0.125	0.449	60	20	1.5	0.036	2	30	100	0.039	6.9	4
1ES 0806+524	0.138	0.19	17.7	2	3.1	0.39	0.5	20	3	0.31	2.6	5
1ES 0806+524	0.138	0.14	16	2	2.7	0.5	0.5	20	3	0.68	2.6	5
Mrk 421	0.031	0.0776	42	5	2.6	0.48	0.3	20	3	0.4	1.4	6
Mrk 421	0.031	0.106	33	4	3.2	0.68	0.3	20	3	0.59	1.4	6
W Comae	0.102	28	0.45	4.5	2.2	0.007	10	30	200	0.00059	31.2	7
W Comae	0.102	3.4	9	2.5	2.55	0.24	0.3	20	300	0.0023	1.5	8
3C 66A	0.300*	57	22	4	3	0.02	7	40	1000	0.0015	21.1	9
3C 66A	0.444*	128	25	5	3	0.01	11	50	1000	0.0011	29.4	9

Table 6.3.: SSC model parameters for B2 1215+30 for the high and low X-ray states in 2011 and other VERITAS-detected blazars using the same model. The columns are the following: z is the redshift (* denotes the assumed redshift within the model, see text for more details); $L_{\rm e}$ is the jet luminosity; γ_1 is the low energy cutoff energy of the electron distribution; γ_2 is the high energy cutoff; q is the spectral index of the electron injection spectrum; B is the magnetic field strength; R is the emission region radius; D is the Doppler factor; and $\eta_{\rm esc}$ is the escape time parameter. Additionally, two output parameters are given: $\epsilon_{\rm B}$ is the resulting relative partition parameter $\epsilon_{\rm B} = L_{\rm B}/L_{\rm e}$; and $\delta t_{\rm var}$ is the resulting minimum variability time scale.
References: (1) Aliu et al. (2012a); (2) Aliu et al. (2012b); (3) Aliu et al. (2011); (4) Acciari et al. (2010b); (5) Acciari et al. (2009b); (6) Acciari et al. (2009a); (7) Acciari et al. (2008); (8) Acciari et al. (2009c); (9) Abdo et al. (2011).

example, is usually found to be in the range of $D = 20 - 30$ for the applied model. This is in agreement with the results of other SSC models which have been successfully applied to VHE blazars, e.g. Tavecchio et al. (2010). However, there are two parameters which are outside this "standard range": the magnetic field strength B and the escape time parameter $\eta_{\rm esc}$. The first one is relatively low for B2 1215+30 and results in a very low relative partition parameter. For some of the other blazars, e.g. W Comae and 3C 66A, this behavior has also been seen. In those cases, an SSC model with an external radiation field resulted in model parameters with larger magnetic field strengths and closer to equipartition. However, in the case of B2 1215+30 no improvement could be found by adding an EC component to the model - neither in the representation of the shape of the SED nor by bringing the system closer to equipartition. In general, the magnetic field strength values obtained for the different sources are consistent with results from other leptonic blazar models. The second parameter, $\eta_{\rm esc}$, is high compared to the model parameters of the other blazars. Such a high value for $\eta_{\rm esc}$ implies long escape time scales. This could hint at a relatively well ordered (laminar) magnetic field in the emission region. However, it has already been shown in the previous section that the value for $\eta_{\rm esc}$ can be lowered significantly when the archival data are ignored, without losing the ability to reproduce the shape of the SED. This value is then closer to the ones found for other VERITAS-modeled blazars. In summary, the model parameters derived here for the applied SSC model are in the range of those derived from previous VERITAS blazar modeling. In this sense B2 1215+30 is a typical VHE-detected blazar.

7. Summary and Concluding Remarks

The field of ground-based gamma-ray astronomy is prospering and offers new insights into the high-energy processes of the Universe. Astronomical objects, such as active galactic nuclei (AGN), can accelerate particles up to relativistic energies. These particles produce very-high-energy (VHE; $E > 50$ GeV) gamma rays, detectable on Earth with imaging atmospheric Cherenkov telescopes (IACTs) like VERITAS. The imaging Cherenkov detectors are still evolving and the latest technical improvement for VERITAS happened in summer 2012: the PMTs in each of the VERITAS cameras were replaced with higher quantum efficiency devices. In this thesis, the sensitivity of this camera upgrade has been estimated using new Monte Carlo (MC) simulations. The analysis of these simulations yielded a reduction of the energy threshold at trigger level from ~ 100 GeV down to about 75 GeV and an increase in effective area after cuts, especially at energies below 300 GeV. The result is an improved sensitivity to VHE gamma rays.

The next-generation ground-based gamma-ray observatory CTA aims to be a factor of about ten more sensitive than any existing IACT system. While this goal is likely to be reached, one of the limitations of the Cherenkov technique stays: observations can only be carried out during clear, dark nights, leading to an observation time of about 1000 hours per year. This time can be substantially extended through observations under partial moonlight. As the light from the Moon contributes to the background noise in the cameras, new MC simulations have been set-up to determine the performance of CTA under those special conditions. It has been demonstrated in this thesis that with raised trigger thresholds and small adjustments in the image analysis, the differential sensitivity under moonlight conditions is comparable within a factor of two to the sensitivity reachable under dark-sky conditions. This result makes observations under partial moonlight a very likely operation mode for CTA, adding about 30% observation time per year and thus clearly increasing the scientific outcome of this future VHE gamma-ray observatory. The enlarged duty cycle can be used, e.g., to extend monitoring and/or multi-wavelength (MWL) campaigns on variable sources, such as AGN.

Currently, AGN represent about one third of the population of known VHE gamma-ray sources. Most of these AGN belong to the sub-class of blazars whose relativistic jets are closely aligned to the observer's line of sight. VERITAS has detected 24 out of 52 VHE-emitting blazars.

The observations of the BL Lac B2 1215+30 have been presented in this thesis. The analysis of the full data set, comprising nearly 100 hours of data taken between December 2008 and March 2012, resulted in a detection significance of 9.0σ and revealed long-term variability. In 2011, the object was found in a relatively bright flux state and a power-law fit to the differential photon spectrum yielded a spectral index of $3.6 \pm 0.4_{\mathrm{stat}} \pm 0.3_{\mathrm{syst}}$ with an integral flux above 200 GeV of $(8.0 \pm 0.9_{\mathrm{stat}} \pm 3.2_{\mathrm{syst}}) \times 10^{-12}\mathrm{cm}^{-2}\mathrm{s}^{-1}$. Contemporaneous with the VERITAS observations, MWL observations were obtained at optical (Super-LOTIS, MDM, *Swift*-UVOT), X-ray (*Swift*-XRT) and gamma-ray (*Fermi*-LAT) frequencies. These MWL data have been used to construct the spectral energy distribution (SED) of B2 1215+30 for the first half of 2011.

To investigate the underlying physical processes, the SED has been modeled with a one-zone leptonic model. The model assumes that the emission arises from synchrotron and synchrotron-self Compton (SSC) radiation of a highly relativistic electron population within the jet. Possible constraints on the input parameters of the model have been reviewed and the influence of the Doppler factor and the magnetic field strength on the overall emission has been demonstrated in this thesis. The application of the SSC model to the MWL data of B2 1215+30 results in a good description of the overall SED. The low required magnetic field strength ($B = 0.01 - 0.02$ G) in the emission region implies a magnetic field energy density several orders of magnitude below the corresponding particle energy density, hinting towards a particle-dominated jet as opposed to magnetically dominated jets predicted by jet formation models (e.g., Blandford & Znajek, 1977; McKinney, 2006). Through a comparative study with other SSC-modeled blazars detected by VERITAS, it has been found that most VHE-detected blazars also show the dominance of the particle energy density over magnetic energy density, even though not as extreme as for the case of B2 1215+30. This challenges jet formation models which require strong magnetic fields for launching and collimating the jets − one of the puzzles in AGN research. Most of the other parameter values used to model the broadband emission of B2 1215+30 are in the range of other VERITAS-detected blazars and in this sense, B2 1215+30 is a typical VHE-detected blazar.

Despite the numerous VHE-detections of AGN, many questions remain (e.g., Beckmann & Shrader, 2013): Why do some AGN develop jets while apparently most do not? What powers the jets in AGN and how are they formed? Once the matter is launched and collimated into a jet, what is the acceleration mechanism leading to the relativistic particles producing the observed spectral energy distribution and where is the emission region located? Which mechanisms are responsible for the observed variability? Which particles dominate the outflow in AGNs (leptonic or hadronic) and are AGN the sources of ultra-high-energy cosmic rays? How do AGN outflows interact with the interstellar and intergalactic medium and what is the role of AGN in the evolution of the Galaxy?

To contribute towards answering these questions, observations in the high- and very-high-energy gamma-ray regime are crucial as they sample the second peak of the SED. These observations are needed to identify the dominant emission processes (leptonic versus hadronic) and provide information about the acceleration mechanisms at very high energies. As the models for acceleration and/or emission processes in AGN are becoming more complex, we need precise spectral and temporal measurements to tightly constrain their input parameters. To disentangle between different mechanisms responsible for the observed variability, long-term observations are beneficial and a larger number of sources is needed to disentangle general properties of gamma-ray emission in AGN from characteristics of individual sources (Reimer & Böttcher, 2013).

The Cherenkov Telescope Array (CTA) will be a key observatory in this high-energy regime. With its increased sensitivity, CTA will be able to detect more VHE gamma-ray emitting AGN with different physical properties; ideally from an extragalactic sky survey to avoid biases due to pre-selection from other wavelengths. Its large effective area makes CTA an ideal instrument for the study of timing properties in blazars down to sub-minute time scales. Detecting characteristic temporal features, such as minimal variability time scales or (quasi-) periodic events, could contribute towards answering the question about the size and possible location of the VHE emission region (Sol et al., 2013). This will not only allow us to derive information about the physical processes responsible for variability, but provides as well the opportunity for testing Lorentz invariance (Ellis & Mavromatos, 2013). The increased sensitivity together with the lower energy threshold of CTA will enable the detection of more distant sources and thus enlarge our knowledge of the extragalactic background light and its sources (Dwek & Krennrich, 2013). The combination of temporal and spatial information between AGN measured by the next-generation radio and X-ray telescopes with observations in the gamma-ray regime will provide a deep insight into the high-energy Universe.

A. Cosmic-ray spectra

The gamma-ray and cosmic-ray spectra used throughout this thesis are listed in the following.

For gamma rays, the Crab Nebula spectrum as measured by the HEGRA collaboration (Aharonian et al., 2004) is:

$$\Phi_{gamma} = 2.83 \times 10^{-7} \left(\frac{E}{\mathrm{TeV}}\right)^{-2.62} \mathrm{TeV}^{-1}\mathrm{s}^{-1}\mathrm{m}^{-2}. \tag{A.1}$$

For cosmic-ray protons, the spectrum according to the ATIC measurement is

$$\Phi_{proton} = 0.098 \times 10^{-4} \left(\frac{E}{\mathrm{TeV}}\right)^{-2.62} \mathrm{TeV}^{-1}\mathrm{s}^{-1}\mathrm{m}^{-2}\mathrm{sr}^{-1}. \tag{A.2}$$

For cosmic-ray electrons, the spectrum follows a fit to the *Fermi*-LAT (Abdo et al., 2009b) and the H.E.S.S. data (Aharonian et al., 2009) applying a broken power-law function:

$$\Phi_{electron} = \Phi_0 \left(\frac{E}{E_b}\right)^{-\Gamma_1} \cdot \left(1 + \left(\frac{E}{E_b}\right)^{1/\alpha}\right)^{-(\Gamma_2-\Gamma_1)\alpha} \tag{A.3}$$

with $\Phi_0 = 2.3 \times 10^{-9}\mathrm{TeV}^{-1}\,\mathrm{s}^{-1}\,\mathrm{m}^{-2}\,\mathrm{sr}^{-1}$, $\alpha = 0.4$, $\Gamma_1 = 3.07$, $\Gamma_2 = 5$, and $E_b = 1.7\,\mathrm{TeV}$.

B. VERITAS data

This appendix details additional information about the observational data used within this thesis.

B.1. VERITAS atmosphere

As already mentioned in Section 3.2.1, in VERITAS two different (site specific) atmospheric profiles are used; corresponding to summer and winter. These two profiles are models to daily radiosonde measurements obtained at the nearby Tucson airport (Daniel, 2007) using all available data from January 1995 to July 2010. The winter atmosphere covers December to March and the summer atmosphere covers the non-monsoon months between June and September. The transistion between these two atmospheres is rather smooth and the time of the transistion can vary between the different observing periods. Therefore, the radiosonde measurements from the specific years are analysed and compared to the atmospheric profiles used within the simulations. An example of the density profiles is shown in Figure B.1 for 2011, where the monthly averaged measurements are overlaid with the models for winter and summer. To avoid that the estimated fluxes of the analysed source are systematically different between two consecutive nights, the transition between the two atmospheric profiles is chosen to be on a full Moon break. In 2011, the transition between winter and summer is therefore set to the 2011 April 18, mainly determined from the differences in the 5 to 10 km range, where most of the energy of the air shower is deposited. A similar scheme is applied to all other data sets used in this thesis. For the 2008/2009 data set the transition date is set to 2009 May 9 while the transition date in 2012 is after the last data taken in March.

B.2. B2 1215+30 runlist

Runlist of all runs passing the quality selection (bad weather or hardware malfunctioning) in chronological order. Runs include pointings on 1ES 1218+304 (N,S,W) and B2 1215+30 (N,S,E,W) which have at least three telescopes participating in the array.

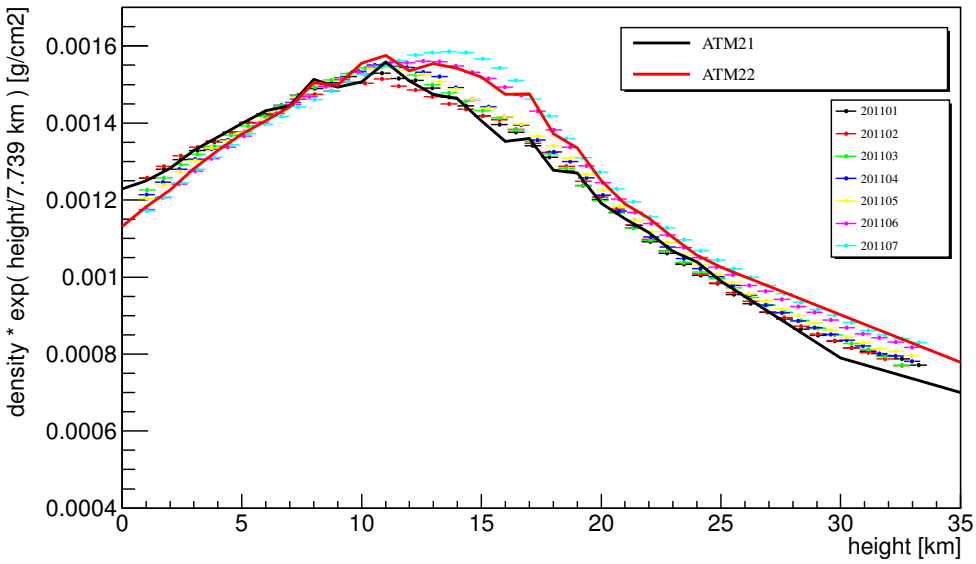

Figure B.1.: Atmospheric density profile in 2011, obtained from daily radiosonde measurements (monthly averaged). Overlaid are the two atmospheric profiles used in the simulations, where ATM21 corresponds to winter and ATM22 to summer.

2008 – 2009 data set

Winter atmosphere:

43777, 43778, 43779, 43780, 43812, 43813, 43814, 43955, 43956, 43957, 43961, 43967, 43968, 43969, 44153, 44159, 44275, 44276, 44278, 44279, 44313, 44314, 44316, 44345, 44346, 44347, 44348, 44349, 44350, 44351, 44352, 44353, 44354, 44355, 44375, 44378, 44379, 44380, 44381, 44384, 44385, 44386, 44387, 44388, 44389, 44427, 44430, 44431, 44432, 44439, 44443, 44444, 44457, 44458, 44459, 44460, 44464, 44465, 44471, 44475, 44476, 44477, 44478, 44479, 44491, 44492, 44493, 44508, 44587, 44704, 44706, 44707, 44730, 44731, 44732, 44733, 44735, 44737, 44795, 44907, 44908, 44910, 44913, 45067, 45068, 45069, 45071, 45152, 45528, 45529, 45530, 45531, 45695, 45696, 45697, 45698, 45701, 45702

Summer atmosphere:

46014, 46017, 46018, 46019, 46099, 46100, 46119, 46120

2010 – 2011 data set

Winter atmosphere:

54109, 54110, 54304, 54305, 54306, 54307, 54364, 54365, 54366, 54392, 54393, 54442, 54443,

54454, 54455, 54664, 54665, 54830, 54831, 54931, 54933, 54934, 54935, 54937, 54938, 54963, 55026, 55027, 55076, 55177, 55178, 55179, 55232, 55407, 55479, 55480, 55580, 55707, 55724, 55725, 55726, 55754, 55755, 55756, 55776, 55777, 55839, 55841, 55842, 55843, 55901, 55902, 55903, 55938, 55939, 55940, 55942, 56005, 56007, 56008, 56081, 56082, 56085, 56086, 56111, 56113, 56114, 56115, 56116, 56119, 56145, 56147, 56148, 56163

Summer atmosphere:

56237, 56238, 56239, 56240, 56261, 56263, 56294, 56295, 56296, 56298, 56319, 56320, 56321, 56322, 56359, 56360, 56362, 56363, 56384, 56386, 56389, 56390, 56480, 56481, 56484, 56485, 56507, 56509, 56510, 56511, 56534, 56535, 56536, 56537, 56538, 56554, 56559, 56562, 56610, 56611, 56612, 56613, 56725, 56726, 56746, 56763, 56764, 56791, 56841, 56842, 56929, 56930, 56932, 57012, 57079, 57080

2011 – 2012 data set

Winter atmosphere:

59846, 59907, 59908, 59941, 59990, 60073, 60074, 60173, 60174, 60176, 60177, 60178, 60202, 60203, 60223, 60239, 60240, 60257, 60258, 60259, 60276, 60277, 60404, 60407, 60408, 60478, 60480, 60481, 60538, 60567, 60568, 60569, 60629, 60630, 60657, 60659, 60660, 60694, 60856, 60892, 60894, 60895, 61144, 61206, 61207, 61209, 61344, 61345, 61349, 61633, 61634

B.3. B2 1215+30 light curve analysis and fluxes

In the following the light curves from the different seasons and the fluxes per "dark run" (corresponding to 29.5 days, where the bin edge is chosen to be on the full Moon) are given. The tables contain the following information:

MJD	The start and end date of the observations.
Time	The exposure time in minutes is given in effective time on B2 1215+30 (in 0.5° wobble offset equivalent).
Elev.	The mean elevation angle of the observations
Non	The number of events in the ON region.
Noff	The the number of events in the OFF region.
α	The normalisation given as the acceptence corrected area ratio between ON and OFF region.
Signif.	The significance of the flux point above the energy threshold.
$F(E > 200\text{GeV})$	The flux above 200 GeV, calculated using the spectral index derived in 2011, with 1-sigma statistical error bars.
$\text{UL}(E > 200\text{GeV})$	The 99% upper limit above 200 GeV, calculated using the method of Helene.

2008 – 2009 data set

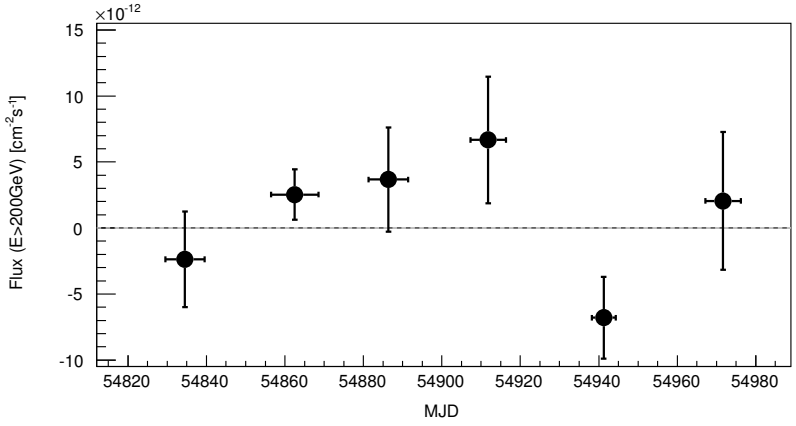

Figure B.2.: VERITAS light curve above 200 GeV for the 2008/2009 data set. Vertical error bars show 1σ statistical uncertainties on the flux, horizontal error bars indicate the width of the corresponding observing interval within the monthly bins. A fit to a constant (using the flux-point representation of the bin) yields $\chi^2/ndf = 9.7/5$.

MJD	Time [min]	Elev. [deg]	Non	Noff	α	Signif. [σ]	$F(E > 200\text{GeV})$ [in units of $10^{-12}\,\text{cm}^{-2}\,\text{s}^{-1}$]	UL
54829 - 54839	256	83.8	45	396	0.1255	-0.6	-2.4 ± 3.6	< 7.7
54856 - 54868	1040	75.8	159	1143	0.1236	1.4	2.5 ± 1.9	< 7.0
54881 - 54891	210	80.3	36	241	0.1250	1.0	3.7 ± 3.9	< 13.1
54907 - 54916	180	80.5	36	219	0.1245	1.5	6.7 ± 4.8	< 18.0
54938 - 54944	185	81.5	16	205	0.1250	-1.9	-6.8 ± 3.1	< 4.4
54967 - 54976	153	77.7	9	62	0.1251	0.4	2.1 ± 5.2	< 15.0

Table B.1.: VERITAS results of B2 1215+30 for 2008/2009.

2010 – 2011 data set

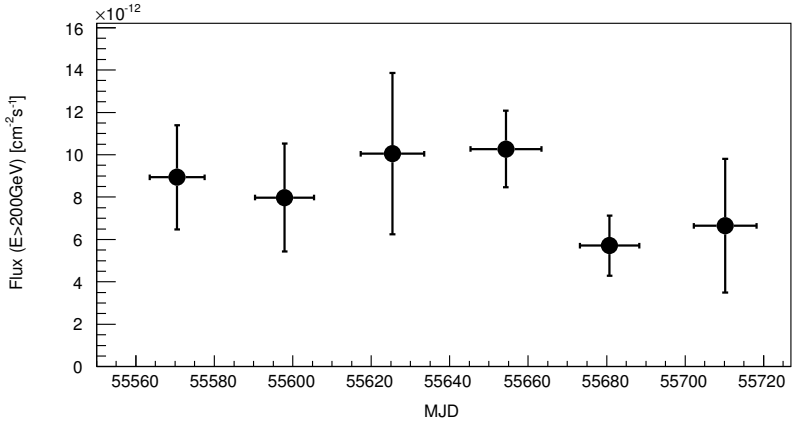

Figure B.3.: VERITAS light curve above 200 GeV for the 2010/2011 data set. Vertical error bars show 1σ statistical uncertainties on the flux, horizontal error bars indicate the width of the corresponding observing interval within the monthly bins. A fit to a constant (using the flux-point representation of the bin) yields $\chi^2/ndf = 4.7/5$.

MJD	Time [min]	Elev. [deg]	Non	Noff	α	Signif. [σ]	$F(E > 200\text{GeV})$ [$10^{-12}\,\text{cm}^{-2}\,\text{s}^{-1}$]
55563 - 55577	286	84.7	67	306	0.1167	4.4	9.5 ± 2.6
55590 - 55605	280	79.8	49	238	0.1172	3.4	7.4 ± 2.5
55617 - 55633	160	75.1	35	165	0.1156	3.0	10.1 ± 3.9
55645 - 55663	715	78.4	148	652	0.1182	6.7	10.4 ± 1.8
55673 - 55688	793	76.5	124	682	0.1137	4.5	5.8 ± 1.4
55702 - 55718	280	64.4	35	181	0.1181	2.5	7.1 ± 3.2

Table B.2.: VERITAS results of B2 1215+30 for 2010/2011.

2011 – 2012 data set

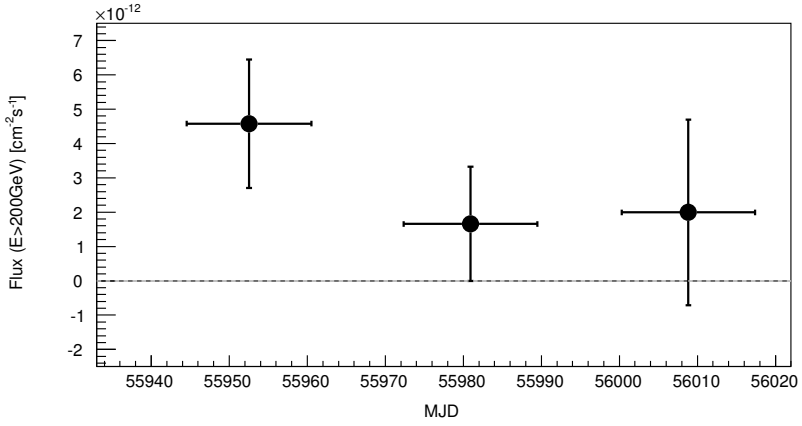

Figure B.4.: VERITAS light curve above 200 GeV for the 2011/2012 data set. Vertical error bars show 1σ statistical uncertainties on the flux, horizontal error bars indicate the width of the corresponding observing interval within the monthly bins. A fit to a constant (using the flux-point representation of the bin) yields $\chi^2/ndf = 1.5/2$.

MJD	Time [min]	Elev. [deg]	Non	Noff	α	Signif. [σ]	$F(E > 200\text{GeV})$ [in units of $10^{-12}\,\text{cm}^{-2}\,\text{s}^{-1}$]	UL
55944 - 55960	413	78.1	57	321	0.1178	2.7	4.6 ± 1.9	< 8.9
55972 - 55989	402	81.3	45	322	0.1180	1.0	1.7 ± 1.7	< 5.6
56000 - 56017	171	75.3	21	148	0.1180	0.8	2.0 ± 2.7	< 8.5

Table B.3.: VERITAS results of B2 1215+30 for 2011/2012.

Bibliography

Abdo, A. A. et al., 2009a, *Fermi/Large Area Telescope Bright Gamma-Ray Source List*, ApJS, 183, 46

Abdo, A. A. et al., 2009b, *Measurement of the Cosmic Ray $e^+ + e^-$ Spectrum from 20GeV to 1TeV with the Fermi Large Area Telescope*, Physical Review Letters, 102, 18

Abdo, A. A. et al., 2011, *Fermi Large Area Telescope Observations of Markarian 421: The Missing Piece of its Spectral Energy Distribution*, ApJ, 736, 131

Abdo, A. A. et al., 2011, *Insights into the High-energy γ-ray Emission of Markarian 501 from Extensive Multifrequency Observations in the Fermi Era*, ApJ, 727, 129

Abdo, A. A. et al., 2011, *Multi-wavelength Observations of the Flaring Gamma-ray Blazar 3C 66A in 2008 October*, ApJ, 726, 43

Abramowski, A. et al., 2010, *VHE γ-ray emission of PKS 2155-304: spectral and temporal variability*, A&A,520, A83

Abramowski, A. et al., 2013, *Measurement of the extragalactic background light imprint on the spectra of the brightest blazars observed with H.E.S.S.*, A&A, 550, A4

Acciari, V. A. et al., 2008, *VERITAS Discovery of greater than 200 GeV Gamma-Ray Emission from the Intermediate-Frequency-Peaked BL Lacertae Object W Comae*, ApJ, 684, L73

Acciari, V. A. et al., 2009a, *Simultaneous Multiwavelength Observations of Markarian 421 During Outburst* , ApJ, 703, 169

Acciari, V. A. et al., 2009b, *Discovery of Very High Energy Gamma-ray Radiation from the BL Lac 1ES 0806+52*, ApJ, 690, L126

Acciari, V. A. et al., 2009c, *Multiwavelength Observations of a TeV-Flare from W Comae*, ApJ, 707, 612

Acciari, V. A. et al., 2010a, *Discovery of Very High Energy Gamma Rays from PKS 1424+240 and Multiwavelength Constraints on Its Redshift* , ApJ, 708, L100

Acciari, V. A. et al., 2010b, *The Discovery of γ-Ray Emission from the Blazar RGB J0710+591* , ApJ, 715, L49

Acciari, V. A. et al., 2011a, *TeV and Multi-wavelength Observations of Mrk 421 in 2006-2008*, ApJ, 738, 25

Acciari, V. A. et al., 2011b, *Spectral Energy Distribution of Markarian 501: Quiescent State versus Extreme Outburst*, ApJ, 729, 2

Acharya, B. S. et al., 2013, *Introducing the CTA concept*, Astroparticle Physics, 43, 3

Ackermann, M. et al., 2011, *The Second Catalog of Active Galactic Nuclei Detected by the Fermi Large Area Telescope*, ApJ, 743, 171

Ackermann, M. et al., 2012, *The Imprint of the Extragalactic Background Light in the Gamma-Ray Spectra of Blazars*, Science, 338, 1190

Actis, M. et al., 2011, *Design concepts for the Cherenkov Telescope Array CTA: an advanced facility for ground-based high-energy gamma-ray astronomy*, Experimental Astronomy, 32, 193

Aharonian, F. A., 2000, *TeV gamma rays from BL Lac objects due to synchrotron radiation of extremely high energy protons*, New Astronomy, 5, 377

Aharonian, F. A., Hofmann, W., Konopelko, A. K. & Völk, H. J., 1997, *The potential of ground based arrays of imaging atmospheric Cherenkov telescopes. I. Determination of shower parameters*, Astroparticle Physics, 6, 343

Aharonian, F. A. et al., 2004, *The Crab Nebula and Pulsar between 500 GeV and 80 TeV: Observations with the HEGRA Stereoscopic Air Cerenkov Telescopes*, ApJ, 614, 897

Aharonian, F. A. et al., 2006, *Observations of the Crab nebula with HESS*, A&A, 457, 899

Aharonian, F. A. et al., 2007, *An Exceptional Very High Energy Gamma-Ray Flare of PKS 2155-304*, ApJ, 664, L71

Aharonian, F. A. et al., 2009, *Probing the ATIC peak in the cosmic-ray electron spectrum with H.E.S.S.*, A&A, 508, 561

Aharonian, F., Buckley, J., Kifune, T. & Sinnis, G., 2008, *High energy astrophysics with ground-based gamma ray detectors*, Reports on Progress in Physics, 71, 096901

Akiyama, M. et al., 2003, *Optical Identification of the ASCA Medium Sensitivity Survey in the Northern Sky: Nature of Hard X-Ray-Selected Luminous Active Galactic Nuclei*, ApJS, 148, 275

Albert, J. et al., 2008, *Probing quantum gravity using photons from a flare of the active galactic nucleus Markarian 501 observed by the MAGIC telescope*, Physics Letters B, 668, 253

Aleksić, J. et al., 2011, *MAGIC Discovery of Very High Energy Emission from the FSRQ PKS 1222+21*, ApJ, 730, L8

Aleksić, J. et al., 2012a, *Performance of the MAGIC stereo system obtained with Crab Nebula data*, Astroparticle Physics, 35, 435

Aleksić, J. et al., 2012b, *Discovery of VHE γ-rays from the blazar 1ES 1215+303 with the MAGIC telescopes and simultaneous multi-wavelength observations*, A&A, 544, A142

Aliu, E. et al., 2011, *Multiwavelength Observations of the Previously Unidentified Blazar RX J0648.7+1516*, ApJ, 742, 127

Aliu, E. et al., 2012a, *Discovery of High-energy and Very High Energy γ-Ray Emission from the Blazar RBS 0413*, ApJ, 750, 94

Aliu, E. et al., 2012b, *Multiwavelength Observations of the AGN 1ES 0414+009 with VERITAS, Fermi-LAT, Swift-XRT, and MDM*, ApJ, 755, 118

Aliu, E. et al., 2013, *Long term observations of B2 1215+30 with VERITAS*, ApJ, submitted

Antón, S. et al., 2004, *The spectral energy distributions of the revised 200-mJy sample*, MNRAS, 352, 673

Antonucci, R., 1993, *Unified models for active galactic nuclei and quasars*, ARA&A, 31, 473

Arlen, T. et al., 2013, *Rapid TeV Gamma-Ray Flaring of BL Lacertae*, ApJ, 762, 92

Atwood, W. B. et al., 2009, *The Large Area Telescope on the Fermi Gamma-Ray Space Telescope Mission*, ApJ, 697, 1071

Bähr, J. for the CTA Consortium, 2012, *Status of the CTA medium size telescope prototype*, American Institute of Physics Conference Series, 1505, 753

Barrau, A. et al., 1998, *The CAT imaging telescope for very-high-energy gamma-ray astronomy.*, Nuclear Instruments and Methods in Physics Research A, 416, 278

Beckmann, V. & Shrader, C. R., 2013, *The AGN phenomenon: open issues*, 9th INTEGRAL Workshop, arXiv:1302.1397

Benbow, W. for the VERITAS Collaboration, 2011, *Highlights of the VERITAS Blazar Observation Program*, in Proc 32nd ICRC, Beijing, arXiv:1110.0038

Berge, D., Funk, S. and Hinton, J., 2007, *Background modelling in very-high-energy γ-ray astronomy*, A&A, 466, 1219

Beringer, J. et al., 2012, *Review of Particle Physics*, Phys. Rev. D, 86, 1

Bernlöhr, K., 2000, *Impact of atmospheric parameters on the atmospheric Cherenkov technique*, Astroparticle Physics, 12, 255

Bernlöhr, K., Carmona, E. & Schweizer, T., 2007, *MC Simulation and Layout Studies for a future Cherenkov Telescope Array*, in Proc 30th ICRC, Merida

Bernlöhr, K., 2008a, *CTA simulations with CORSIKA/sim_telarray*, American Institute of Physics Conference Series, 1085, 874

Bernlöhr, K., 2008b, *Simulation of imaging atmospheric Cherenkov telescopes with CORSIKA and sim_telarray*, Astroparticle Physics, 30, 149

Bernlöhr, K. et al., 2013, *Monte Carlo design studies for the Cherenkov Telescope Array*, Astroparticle Physics, 43, 171

Blandford, R. D. & Eichler, D., 1987, *Particle acceleration at astrophysical shocks: A theory of cosmic ray origin*, Phys. Rep., 154, 1

Blandford, R. D. & Königl, A., 1979, *Relativistic jets as compact radio sources*, ApJ, 232, 34

Blandford, R. D. & Znajek, R. L., 1977, *Electromagnetic extraction of energy from Kerr black holes*, MNRAS, 179, 433

Błażejowski, M., Sikora, M., Moderski, R., & Madejski, G. M., 2000, *Comptonization of Infrared Radiation from Hot Dust by Relativistic Jets in Quasars* , ApJ, 545, 107

Böttcher, M., 2007, *Modeling the emission processes in blazars*, Ap&SS, 309, 95

Böttcher, M., 2012, *Modeling the Spectral Energy Distributions and Variability of Blazars*, arXiv:1205.0539

Böttcher, M. & Chiang, J., 2002, *X-Ray Spectral Variability Signatures of Flares in BL Lacertae Objects*, ApJ, 581, 127

Böttcher, M. et al., 2012, *Relativistic Jets from Active Galactic Nuclei*, WILEY-VCH, edited by M. Böttcher, D. E. Harris, and H. Krawczynski

Breeveld, A. A. et al., 2012, *Further calibration of the Swift ultraviolet/optical telescope*, MNRAS, 406, 1687

Britzger, D. et al., 2009, *Studies of the Influence of Moonlight on Observations with the MAGIC Telescope*, in Proc 31st ICRC, Lodz

Browne, I. W. A., 1971, *Two Bright New Quasi-stellar Radio Sources*, Nature, 231, 515

Buckley, J. et al., 2008, *The Status and future of ground-based TeV gamma-ray astronomy. A White Paper prepared for the Division of Astrophysics of the American Physical Society*, arXiv:0810.0444

Burrows, D. N. et al.., 2005, *The Swift X-Ray Telescope*, Space Sci. Rev., 120, 165

Čerenkov, P. A., 1937, *Visible Radiation Produced by Electrons Moving in a Medium with Velocities Exceeding that of Light*, Phys. Rev., 52, 378

Cogan, P. for the VERITAS Collaboration, 2007, *Analysis of Flash ADC Data With VERITAS*, in Proc 30th ICRC, Merida

Colla, G. et al., 1970, *A catalogue of 3235 radio sources at 408 MHz*, A&AS, 1, 281

Cortina, J. et al., 2013, *MAGIC and VERITAS detect an unprecedented flaring activity from Mrk 421 in very high energy gamma-rays*, The Astronomer's Telegram 4976

Daniel, M. K., 2007, *Application of radiosonde data to VERITAS simulations*, in Proc 30th ICRC, Merida

Daum, A. et al., 1997, *First results on the performance of the HEGRA IACT array*, Astroparticle Physics, 8, 1

Davies, J. M & Cotton, E. S., 1957, *Design of the quartermaster solar furnance*, J. Solar Energy, 1, 16

Dermer, C. & Lott, B., 2012, *On leptonic models for blazars in the Fermi era*, Journal of Physics Conference Series, 355, 1

Dermer, C. D. & Schlickeiser, R., 1993, *Model for the High-Energy Emission from Blazars*, ApJ, 416, 458

Dermer, C. D., Schlickeiser, R. & Mastichiadis, A., 1992, *High-energy gamma radiation from extragalactic radio sources*, A&A, 256, L27

Dermer, C. D., Sturner, S. J. & Schlickeiser, R., 1997, *Nonthermal Compton and Synchrotron Processes in the Jets of Active Galactic Nuclei*, ApJS, 109, 103

Dole, H. et al., 2006, *The cosmic infrared background resolved by Spitzer. Contributions of mid-infrared galaxies to the far-infrared background*, A&A, 541, 417

Dondi, L. & Ghisellini, G., 1995, *Gamma-ray-loud blazars and beaming*, MNRAS, 273, 583

Dwek, E. & Krennrich, F., 2013, *The extragalactic background light and the gamma-ray opacity of the universe*, Astroparticle Physics, 43, 112

Ellis, J., & Mavromatos, N. E., 2013, *Probes of Lorentz violation*, Astroparticle Physics, 43, 50

Farnier, C., & Lenain, J.-P., 2011, *Performance studies on the CTA array for an altitude of 3700 m and 2000 m with Moon light background*, Internal CTA Note

Fegan, D. J., 1997, *γ/hadron separation at TeV energies*, Journal of Physics G Nuclear Physics, 23, 1013

Fermi, E., 1949, *On the Origin of the Cosmic Radiation*, Physical Review, 75, 1169

Finke, J. D., Razzaque, S. & Dermer, C. D., 2012, *Modeling the Extragalactic Background Light from Stars and Dust*, ApJ, 712, 238

Fitzpatrick, E. L., 1999, *Correcting for the Effects of Interstellar Extinction*, PASP, 111, 63

Fomin, V. P. et al., 1994, *New methods of atmospheric Cherenkov imaging for gamma-ray astronomy. I. The false source method*, Astroparticle Physics, 2, 137

Fossati, G. et al., 1998, *A unifying view of the spectral energy distributions of blazars*, MNRAS, 299, 433

Fossati, G. et al., 2008, *Multiwavelength Observations of Markarian 421 in 2001 March: An Unprecedented View on the X-Ray/TeV Correlated Variability*, ApJ, 677, 906

Furniss, A. et al., 2013, *On the Redshift of the Very High Energy Blazar 3C 66A*, ApJ, 766, 35

Franceschini, A., Rodighiero, G. & Vaccari, M., 2008, *Extragalactic optical-infrared background radiation, its time evolution and the cosmic photon-photon opacity*, A&A, 487, 837

Frank, J., King, A. & Raine, D. J., 2002, *Accretion Power in Astrophysics: Third Edition*, Cambridge University Press, 398 p.

Gaisser, T. K., 1990, *Cosmic rays and particle physics*, Cambridge and New York, Cambridge University Press, 292 p.

Galante, N. for the VERITAS Collaboration, 2012, *Status and highlights of VERITAS*, American Institute of Physics Conference Series, 1505, 202

Galbraith, W. & Jelley, J. V., 1953, *Light Pulses from the Night Sky associated with Cosmic Rays*, Nature, 171, 349

Georganopoulos, M. & Kazanas, D., 2003, *Decelerating Flows in TeV Blazars: A Resolution to the BL Lacertae-FR I Unification Problem*, ApJ, 594, L27

Gilmore, R. C. et al., 2009, *GeV gamma-ray attenuation and the high-redshift UV background*, MNRAS, 399, 1694

Gliozzi, M. et al., 2006, *Long-Term X-Ray and TeV Variability of Mrk 501*, ApJ, 646, 61

Graff, P. B., Georganopoulos, M., Perlman, E. S. & Kazanas, D., 2008, *A Multizone Model for Simulating the High-Energy Variability of TeV Blazars*, ApJ, 689, 68

Hall, J. et al., 2003, *Veritas CFDs*, in Proc 28th ICRC, Trukuba

Hampf, D. et al., 2011, *Measurement of night sky brightness in southern Australia*, Advances in Space Research, 48, 1017

Hanna, D., McCann, A., McCutcheon, M. & Nikkinen, L. 2010, *An LED-based flasher system for VERITAS*, Nuclear Instruments and Methods in Physics Research A, 612, 278

Hansen, P. M., Alvarez-Muñiz, J. & Vázquez, R. A., 2011, *A comprehensive study of shower to shower fluctuations*, Astroparticle Physics, 34, 503

Harris, D. E. & Krawczynski, H., 2002, *X-Ray Emission Processes in Radio Jets*, ApJ, 565, 244

Hays, E. for the VERITAS Collaboration, 2007, *VERITAS Data Acquisition*, in Proc 30th ICRC, Merida

Heck, D. et al., 1998, *CORSIKA: a Monte Carlo code to simulate extensive air showers.*, Forschungszentrum Karlsruhe Report FZKA 6019

Heitler, W., 1954, *Quantum theory of radiation*, International Series of Monographs on Physics, Oxford: Clarendon, 3rd ed.

Helene, O., 1983, *Upper limit of peak area*, Nuclear Instruments & Methods 212, 319

Hillas, A. M., 1985, *Cerenkov light images of EAS produced by primary gamma*, in Proc 19th ICRC, La Jolla

Hillas, A. M., 2013, *Evolution of ground-based gamma-ray astronomy from the early days to the Cherenkov Telescope Arrays*, Astroparticle Physics, 43, 19

Hillas, A. M. et al., 1998, *The Spectrum of TeV Gamma Rays from the Crab Nebula*, ApJ, 503, 744

Hinton, J. A. and Hofmann, W., 2009, *Teraelectronvolt Astronomy*, ARA&A, 47, 523

Hofmann, W. et al., 1999, *Comparison of techniques to reconstruct VHE gamma-ray showers from multiple stereoscopic Cherenkov images*, Astroparticle Physics, 12, 135

Holder, J. for the VERITAS Collaboration, 2005, *Exploiting VERITAS Timing Information*, in Proc 29th ICRC, Pune, arXiv:astro-ph/0507450

Holder, J. et al., 2006, *The first VERITAS telescope*, Astroparticle Physics, 25, 391

Holder, J. et al., 2011, *VERITAS: Status and Highlights*, in Proc 32nd ICRC, Beijing, arXiv:1111.1225v1

James, F., 1998, *MINUIT - Function Minimization and Error Analysis*, CERN Program Library Long Writeup D506

Jorstad, S. G. et al., 2001, *Multiepoch Very Long Baseline Array Observations of EGRET-detected Quasars and BL Lacertae Objects: Superluminal Motion of Gamma-Ray Bright Blazars*, ApJS, 134, 181

Joshi, M. & Böttcher, M., 2011, *Time-dependent Radiation Transfer in the Internal Shock Model Scenario for Blazar Jets*, ApJ, 727, 21

Kalberla, P. M. W. et al., 2005, *Leiden/Argentine/Bonn (LAB) Survey of Galactic HI (Kalberla+ 2005)*, VizieR Online Data Catalog 8076

Katarzyński, K., 2012, *Hard MeV-GeV spectra of blazars*, A&A, 537, A47

Kieda, D. for the VERITAS Collaboration, 2011, *Status of the VERITAS Upgrade*, in Proc 32nd ICRC, Beijing, arXiv:1110.4360

Kildea, J. et al., 2007, *The Whipple Observatory 10 m gamma-ray telescope, 1997-2006*, Astroparticle Physics, 28, 182

Kino, M., Takahara, F. & Kusunose, M., 2002, *Energetics of TeV Blazars and Physical Constraints on Their Emission Regions*, ApJ, 564, 97

Kirk, J. G. & Duffy, P., 1999, *TOPICAL REVIEW: Particle acceleration and relativistic shocks*, Journal of Physics G Nuclear Physics, 25, 163

Kohnle, A. et al., 1996, *Stereoscopic imaging of air showers with the first two HEGRA Cherenkov telescopes*, Astroparticle Physics, 5, 119

Krawczynski, H. et al., 2004, *Multiwavelength Observations of Strong Flares from the TeV Blazar 1ES 1959+650*, ApJ, 601, 151

Lanzetta, K. M., Turnshek, D. A. & Sandoval, J., 1993, *Ultraviolet spectra of QSOs, BL Lacertae objects, and Seyfert galaxies*, ApJS, 84, 109

Le Borgne, D. et al., 2004, *Evolutionary synthesis of galaxies at high spectral resolution with the code PEGASE-HR. Metallicity and age tracers*, A&A, 425, 881

Li, T.-P. & Ma, Y.-Q., 1983, *Analysis methods for results in gamma-ray astronomy*, ApJ, 272, 317

Lister, M. L. et al., 2009, *MOJAVE: Monitoring of Jets in Active Galactic Nuclei with VLBA Experiments. VI. Kinematics Analysis of a Complete Sample of Blazar Jets*, AJ, 138, 1874

Longair, M. S., 1992, *High energy astrophysics. Vol.1: Particles, photons and their detection*, Cambridge University Press, 436 p.

Maier, G., 2010, *Description and application of a simple image fitting method*, Internal VERITAS note

Maier, G., 2011, *A short description of an* evndisplay*-based CTA analysis*, Internal CTA Note

Maier, G. & Knapp, J., 2007, *Cosmic-ray events as background in imaging atmospheric Cherenkov telescopes*, Astroparticle Physics, 28, 72

Mannheim, K., 1993, *The proton blazar*, A&A, 269, 67

Maraschi, L., Ghisellini, G. & Celotti, A., 1992, *A jet model for the gamma-ray emitting blazar 3C 279*, ApJ, 397, L5

Mariotti, M. et al., 2011, *Discovery of Very High Energy Gamma-Ray Emission from 1ES 1215+303 by MAGIC*, The Astronomer's Telegram 3100

Marscher, A. P. & Gear, W. K., 1985, *Models for high-frequency radio outbursts in extragalactic sources, with application to the early 1983 millimeter-to-infrared flare of 3C 273*, ApJ, 298, 114

McCann, A., Hanna, D., Kildea, J. & McCutcheon, M., 2010, *A new mirror alignment system for the VERITAS telescopes*, Astroparticle Physics, 32, 325

McKinney, J. C., 2006, *General relativistic magnetohydrodynamic simulations of the jet formation and large-scale propagation from black hole accretion systems*, MNRAS, 368, 1561

Middelberg, E. & Bach, U., 2008, *High resolution radio astronomy using very long baseline interferometry*, Reports on Progress in Physics, 71, 6

Mücke, A. & Protheroe, R. J., 2001, *A proton synchrotron blazar model for flaring in Markarian 501*, Astroparticle Physics, 15, 121

Nagai, T. et al., 2007, *Focal Plane Instrumentation of VERITAS*, in Proc 30th ICRC, Merinda

Niemiec, J. et al. for the CTA consortium, 2013, *Single-Mirror Small-Size Telescope Structure for the Cherenkov Telescope Array*, to appear in Proc. 33rd ICRC, Rio de Janeiro

Nieppola, E., Tornikoski, M. & Valtaoja, E., 2006, *Spectral energy distributions of a large sample of BL Lacertae objects*, A&A, 445, 441

Nilsson, K. et al., 2007, *Host galaxy subtraction of TeV candidate BL Lacertae objects*, A&A, 475, 199

Nolan, P. L. et al., 2012, *Fermi Large Area Telescope Second Source Catalog*, ApJS, 199, 31

Otte, N. A. for the VERITAS Collaboration, 2011, *The Upgrade of VERITAS with High Efficiency Photomultipliers*, in Proc 32nd ICRC, Beijing, arXiv:1110.4702

Paneque, D., 2012, *Experimental Gamma-Ray Astronomy*, Journal of Physics Conference Series, 375, 052020

Perkins, J. S. & Maier, G. for the VERITAS Collaboration, 2009, *VERITAS Telescope 1 Relocation: Details and Improvements*, in Proc Fermi Symposium, Washington, D.C., arXiv:0912.3841

Piner, B. G. et al., 2012, *Relativistic Jets in the Radio Reference Frame Image Database. II. Blazar Jet Accelerations from the First 10 Years of Data (1994-2003)*, ApJ, 758, 84

Pohl, M. & Schlickeiser, R., 2000, *On the conversion of blast wave energy into radiation in active galactic nuclei and gamma-ray bursts*, A&A, 354, 395

Poole, T. S. et al., 2008, *Photometric calibration of the Swift ultraviolet/optical telescope*, MNRAS, 383, 627

Preuss, S., Hermann, G., Hofmann, W. & Kohnle, A., 2002, *Study of the photon flux from the night sky at La Palma and Namibia, in the wavelength region relevant for imaging atmospheric Cherenkov telescopes*, Nuclear Instruments and Methods in Physics Research A, 481, 229

Prokoph, H. for the VERITAS Collaboration, 2012, *Observations of very high energy emission from B2 1215+30 with VERITAS*, in American Institute of Physics Conference Series, 1505, 538

Rebillot, P. F., Buckley, J. H., Dowkontt, P. & Kosack, K., 2003, *The VERITAS Flash ADC Electronics System*, in Proc 28th ICRC, Trukuba

Reimer, A. & Böttcher, M., 2013, *Studies of active galactic nuclei with CTA*, Astroparticle Physics, 43, 103

Reinthal, R. et al., 2012, *Connection Between Optical and VHE Gamma-ray Emission in Blazar Jets*, Journal of Physics Conference Series, 355, 1 (012013)

Rieger, F. M., Bosch-Ramon, V. & Duffy, P., 2007, *Fermi acceleration in astrophysical jets*, Ap&SS, 309, 119

Rieger, F. M., de Ona-Wilhelmi, E. & Aharonian, F. A., 2013, *TeV Astronomy*, to appear in the special issue of "Frontiers of Physics" on "High Energy Astrophysics", arXiv:1302.5603

Rieger, F. M. & Duffy, P., 2006, *A Microscopic Analysis of Shear Acceleration*, ApJ, 652, 1044

Rybicki, G. B. & Lightman, A. P., 1979, *Radiative processes in astrophysics*, New York, Wiley-Interscience, 393 p.

Roache, E. et al., 2007, *Mirror Facets for the VERITAS Telescopes*, in Proc 30th ICRC, Merinda

Roming, P. W. A. et al., 2005, *The Swift Ultra-Violet/Optical Telescope*, Space Sci. Rev., 120, 95

Rossi, B. & Greisen, K., 1941, *Cosmic-Ray Theory*, Rev. Mod. Phys., 13, 240

Rosswog, S. & Brüggen, M., 2007, *Introduction to High-Energy Astrophysics*, Cambridge University Press

Schlegel, D. J., Finkbeiner, D. P. & Davis, M., 1998, *Maps of Dust Infrared Emission for Use in Estimation of Reddening and Cosmic Microwave Background Radiation Foregrounds*, ApJ, 500, 525

Schmidt, F., 2005, *CORSIKA Shower Images*, `http://www.ast.leeds.ac.uk/~fs/showerimages.html` (last checked May 2012)

Schopper, R., Lesch, H.& Birk, G. T., 1998, *Magnetic reconnection and particle acceleration in active galactic nuclei*, A&A, 335, 26

Senturk, G. D. for the VERITAS Collaboration, 2011, *The Disp Method for Analysing Large Zenith Angle Gamma-Ray Data*, in Proc 32nd ICRC, Beijing

Sikora, M., Begelman, M. C. & Rees, M. J., 1994, *Comptonization of diffuse ambient radiation by a relativistic jet: The source of gamma rays from blazars?*, ApJ, 421, 153

Sironi, L. & Spitkovsky, A., 2009, *Particle Acceleration in Relativistic Magnetized Collisionless Pair Shocks: Dependence of Shock Acceleration on Magnetic Obliquity*, ApJ, 698, 1523

Sol, H., Pelletier, G. & Asseo, E., 1989, *Two-flow model for extragalactic radio jets*, MNRAS, 237, 411

Sol, H. et al., 2013, *Active Galactic Nuclei under the scrutiny of CTA*, Astroparticle Physics, 43, 215

Stamatescu, V. et al., 2012, *Towards an optimized design for the Cherenkov Telescope Array*, American Institute of Physics Conference Series, 1505, 758

Tamm, I.E & Frank, I.M., 1937, Doklady AN SSSR 14, 109

Tavecchio, F., Maraschi, L. & Ghisellini, G., 1998, *Constraints on the Physical Parameters of TeV Blazars*, ApJ, 509, 608

Tavecchio, F. & Ghisellini, G., 2008, *Spine-sheath layer radiative interplay in subparsec-scale jets and the TeV emission from M87*, MNRAS, 385, L98

Tavecchio, F. et al., 2010, *TeV BL Lac objects at the dawn of the Fermi era*, MNRAS, 401, 1570

Tody, D., 1986, *The IRAF Data Reduction and Analysis System*, in SPIE Conference Series 627, 733

Tody, D., 1993, *IRAF in the Nineties*, in Astronomical Society of the Pacific Conference Series 52, 173

Urry, C. M. & Padovani, P., 1995, *Unified Schemes for Radio-Loud Active Galactic Nuclei*, PASP, 107, 803

Vassiliev, V. V. & Fegan, S. J., 2007, *Schwarzschild-Couder two-mirror telescope for ground-based γ-ray astronomy*, in Proc 30th ICRC, Merida, arXiv:0708.2741

Valtaoja, E. et al., 1992, *Five Years Monitoring of Extragalactic Radio Sources - Part Four - Variability Staistics and the Unified Models for AGN / Active Galactic Nuclei*, A&A, 254, 80

Wakely, S. & Horan, D., 2013, *TeVCat - an Online Gamma-Ray Catalog*, `http://tevcat.uchicago.edu/` (last checked May 2013)

Watson, A. A., 2011, *The discovery of Cherenkov radiation and its use in the detection of extensive air showers*, Nuclear Physics B Proceedings Supplements, 212, 13

Weekes, T. C. et al., 1989, *Observation of TeV gamma rays from the Crab nebula using the atmospheric Cerenkov imaging technique*, ApJ, 342, 379

Weinstein, A. for the VERITAS Collaboration, 2007, *The VERITAS Trigger System*, in Proc 30th ICRC, Merinda

Wills, B. J. et al., 1992, *A survey for high optical polarization in quasars with core-dominant radio structure - Is there a beamed optical continuum?*, ApJ, 398, 454

Zech, A. et al., 2013, *SST-GATE: A dual mirror telescope for the Cherenkov Telescope Array*, to appear in Proc 33rd ICRC, Rio de Janeiro

List of Figures

List of Tables

Acknowledgments

First of all, I would like to thank my advisor Dr. Gernot Maier for his support and guidance during the last three years. Apart from introducing me to real data, his deep knowledge on simulations, reconstruction methods and physics made every discussion with him very fruitful. I would also like to thank the members of my PhD committee, especially Prof. Dr. Reshmi Mukherjee and Prof. Dr. Thomas Lohse for refereeing this thesis.

There are other people that contributed directly or indirectly to the results presented in this thesis. Thanks to Konrad Bernlöhr for his long and very detailed answers on all my questions related to CTA simulations. I am very grateful to Markus Böttcher for the opportunity to use his blazar model code and for answering my questions related to the SED modeling. I would also like to spread my gratitude to the whole VERITAS Collaboration for the very friendly atmosphere that we have worked in, especially to Manel Errando for his help and all the discussions we had. It has been a great pleasure to work with you, Manel. Special thanks to Lucie Gérard for the countless discussions, the suggestions to different drafts of the text and especially for reminding me during the writing phase of this thesis that blazars are indeed fascinating objects and not just a single blob in the sky. It has been a pleasure sharing the office with you during the last year.

Many thanks to the members of the different astroparticle groups at DESY who always had their doors open. This thesis would not have shaped so well without all the discussions between the different offices, over lunch, or over a beer. Although it seems so far away that the CTA group at DESY counted only three members, I am deeply grateful to Dr. Stefan Schlenstedt for providing me the opportunity to start my diploma thesis at DESY and be, together with Gareth Hughes, part of this new group. I would also like to thank Gareth for his help and friendship over more than three years.

Finally, I would like to thank my family and friends. Without your overwhelming support, your love and your motivations, I would not have reached this point of my life.

Selbständigkeitserklärung

Hiermit erkläre ich, dass ich die vorliegende Arbeit selbständig und nur unter Verwendung der angegebenen Literatur und Hilfsmittel angefertigt habe. Ich habe mich nicht anderweitig um einen Doktorgrad beworben und besitze keinen Doktorgrad. Die Promotionsordnung der Mathematisch-Naturwissenschaftlichen Fakultät I der Humboldt-Universität zu Berlin ist mir bekannt.

Berlin, den 18.06.2013 Heike Prokoph